

ADVANCED POWER ELECTRONICS TOPOLOGIES AND CONTROL FOR
ELECTRIC DISTRIBUTION AND MICROGRID APPLICATIONS

A Dissertation

by

JORGE ALFONSO RAMOS-RUIZ

Submitted to the Office of Graduate and Professional Studies of
Texas A&M University
in partial fulfillment of the requirements for the degree of

DOCTOR OF PHILOSOPHY

Chair of Committee,	Prasad Enjeti
Committee Members,	Le Xie
	Shankar P. Bhattacharyya
	Zhizhang Xie
Head of Department,	Miroslav M. Begovic

May 2020

Major Subject: Electrical Engineering

Copyright 2020 Jorge Alfonso Ramos-Ruiz

ABSTRACT

The importance of power electronics is increasingly evident as the world economy becomes more electrified. Power electronics play a key role in enabling renewable energy generation growth. Every year the capacity of electricity generation using renewable sources of energy increases worldwide, this growth is expected to continue for several decades. Power electronic converters are needed to make the integration of such resources a reality.

Renewable energy sources such as, solar photovoltaic (PV), wind turbines and micro-turbines are being installed even at distribution centers such as residential areas, industrial locations, etc. When the power generated by these distributed energy resources (DERs) is higher than the local load demand, it is nowadays possible to supply power to the utility grid from the distribution centers and store the excess energy in battery energy storage systems (BESS) for peak shaving and capacity smoothing. Additionally, the possibility of transacting energy between peers in the near future has received increased attention.

As DERs penetration increases, the control of the system becomes more challenging for the distribution system operator (DSO), as the intermittent nature of renewable sources can result in grid instability and voltage magnitude variations, limiting the maximum amount of DERs that can be connected to the grid significantly.

Therefore, this dissertation presents cutting edge power electronics topologies to enable the increased penetration of DERs in the distribution grid.

The first topology accurately controls the voltage magnitude and phase combining phase shifting transformer techniques with AC/AC converters to achieve active and reactive power flow control. This accurate control enables the use of a modified angle droop control scheme, also proposed in this dissertation.

The second topology is a self organizing power electronics converter with control intelligence at the edge of the distribution network, intended for residential applications. This topology significantly improves the traditional residential distribution network, allowing massive levels of PV penetration in residential systems, even 100%, promoting further investment on renewables.

Every topology includes a suggested application to demonstrate their value for the electrical grid, as well as simulation results. Experimental results are also included for the second topology.

ACKNOWLEDGEMENTS

The time I spent at Texas A&M University meant a time of incredible growth, both personally and intellectually. This has made me a better engineer and a better person, helping me to achieve my most challenging achievement; completing a PhD degree. I could not have done this by myself. It was thanks to many persons that helped me during the most difficult times that I completed my doctoral degree. To all of these persons I extend my sincere gratitude.

I will be always grateful to my advisor Dr. Prasad Enjeti for all the knowledge and advice he provided throughout my time as his graduate student. He has been not only a great guide to me, but he was also a patient mentor that taught me about not only about electrical engineering, but also about my professional career, and other important aspects of life as a whole.

I feel privileged to have worked during the last years of my PhD with Dr. Le Xie. He was always a very supportive mentor who helped me grow into the person I am now.

I also want to thank Dr. Shankar P. Bhattacharyya and Dr. Zhizhang Xie, for being members in my PhD committee. I had the privilege of learning from the courses they teach at Texas A&M University.

I would like to acknowledge the students in the Power Electronics and Power Quality research group, without their valuable help, my research would have been very hard. I thank (in no particular order) Somasundaram Essakiappan, Harish Krishnamoorthy, Pawan Garg, Michael Daniel, Jose Sandoval, Erick Pool, Taeyong Kang,

Bahaa Hafez, Ahmed Morsy, Mesaad Albader, Salwan Samir, Sinan Al-Obaidi, Ahmed Allehyani, Eduardo Mejia, Ivan Diaz and Jorge Cisneros for making my learning and life experience more enjoyable.

My PhD would not have been possible without the support of my family and friends. I thank my parents for believing in me and supporting me during the most difficult times.

CONTRIBUTORS AND FUNDING SOURCES

The work presented in this dissertation was guided by the dissertation committee consisting of Professor Prasad Enjeti, Professor Le Xie, Professor Shankar P. Bhattacharyya from the Electrical and Computer Engineering Department, and Professor Zhizhang Xie from the Department of Mathematics.

My PhD studies were partially founded by Mexico's Consejo Nacional de Ciencia y Tecnología (CONACYT). I held the title of Graduate Assistant Research in the Electric Power and Power Electronics program area.

The Power Quality Laboratory from the Electrical and Computer Engineering Department at Texas A&M provided additional resources such as software licenses and laboratory equipment.

TABLE OF CONTENTS

	Page
ABSTRACT	ii
ACKNOWLEDGEMENTS	iv
CONTRIBUTORS AND FUNDING SOURCES	vi
TABLE OF CONTENTS	vii
LIST OF FIGURES	x
LIST OF TABLES	xvii
CHAPTER I INTRODUCTION	1
The importance of Power Electronics for the future electrical grid	1
Distributed Energy Resources impact on the future electrical grid	2
Microgrids	3
Microgrid control.....	4
Current sharing control.....	4
Master/slave	4
Droop control methods	4
Power Electronics and solar Photovoltaics	8
The PV cell/module.....	8
The P-V and I-V curves.....	10
Power converters to interface PV modules with BESS and the grid	11
Voltage quality	16
The stability of the future grid.....	17
Energy Routers	17
Inverters and rectifiers control.....	18
Grid voltage phase detection	20
Research Objective	22
Structure of dissertation	23
CHAPTER II POWER ELECTRONICS TRANSFORMER WITH DYNAMIC VOLTAGE AND ANGLE DROOP CONTROL FOR MICROGRID APPLICATIONS	25
Introduction	25

AC-AC converters	26
Proposed topology for PET-DVADC	31
Duty cycle calculations	34
Example system to optimize transformer ratings	35
Simulation results	37
Conclusions and future work.....	40
CHAPTER III PET-DVADC ENABLED ANGLE DROOP CONTROL FOR MICROGRID POWER FLOW CONTROL.....	41
Introduction	41
Conventional Angle Droop Control.....	44
Modified Angle Droop Control for peer-to-peer energy transaction.....	44
Design examples and simulation results	45
Transactive Energy Scenario # 1	45
Transactive Energy Scenario # 2	50
Conclusions and future work.....	53
CHAPTER IV POWER ELECTRONICS INTELLIGENCE AT THE NETWORK EDGE (PINE) – A NEW TOPOLOGY TO INTERFACE PV AND BATTERY ENERGY STORAGE SYSTEMS AT THE GRID EDGE.....	54
Introduction	55
Proposed PINE topology.....	59
PV system design	61
Front end PWM converter	63
Output PWM converter	64
Rooftop Solar PV/Battery Interface	64
Control strategy of the PINE converter.....	65
Front end PWM converter control	65
Output PWM converter control	67
Rooftop Solar PV/Battery Interface control	70
Simulation results	72
A single PINE without the use of the PV/BESS system	73
Supplying power to the grid	76
PINE modes of operation as the time of the day changes	77
Energy budgeting	87
Hardware results	91
Conclusions	94
CHAPTER V IMPLEMENTATION IMPACTS OF PINE TOPOLOGY AT THE GRID EDGE.....	95
Introduction	95
PINE average model	98

Front End PWM converter average model.....	98
Output PWM converter average model.....	100
Demonstration of PINE’s value on a small distribution system.....	102
Increased penetration levels of PINE in a residential distribution system.....	105
Simulation with average model	108
Simulation with switching converters	109
Conclusions	111
CHAPTER VI SUMMARY	112
Conclusion.....	112
Future Work.....	113
REFERENCES	114
APPENDIX A LINE PARAMETERS OF TEST FEEDER SYSTEM. ADAPTED FROM [67].....	121

LIST OF FIGURES

	Page
Fig. 1. The growing electricity demand is being supplied by renewable energy sources in an increasing rate. Adapted from [1].	2
Fig. 2. Typical microgrid structure, the microgrid is connected to the rest of the grid via the Point of Common Coupling (PCC).	3
Fig. 3. Frequency droop control curves. a) Frequency (ω) vs Real Power (P) curve. b) Voltage (V) vs Reactive Power (Q) curve.	6
Fig. 4. PV cell equivalent circuit.	9
Fig. 5. Relationship between the power and voltage of the PV cell (P-V curve), and relationship between current and voltage of the PV cell (I-V curve).	10
Fig. 6. In line systems. The BESS is connected directly to the dc-link, the PV system is interfaced with a DC-DC stage. The dc-link is then interfaced to the grid with a single DC-AC stage, where all the loads are connected. Adapted from [16].	12
Fig. 7. DC coupled systems. Two separate DC-DC stages are needed to interface the PV and the BESS to the dc-link, this architecture improves flexibility to the BESS to be charged/discharged, the residential load is connected at the grid. Adapted from [16]	13
Fig. 8. AC coupled systems. The PV and the BESS are connected to the grid with independent DC-DC and DC-AC stages, this approach further improves flexibility, allowing techniques such as Electric Demand Side Management EDSM.	14
Fig. 9. AC and DC coupled systems. One single stage is used to interface the dc-link with the grid. Loads can be connected at either the dc-link or the grid side, further improving flexibility and efficiency. Adapted from [16].	15
Fig. 10. Proposed topology for PV/BESS interface to the grid. Named Power Electronics Intelligence at the Network Edge, this topology is discussed in chapters 4 and 5.	16
Fig. 11. General structure of PLL for grid synchronized converters. Adapted from [25].	21

Fig. 12. Strategy to create the orthogonal component of the grid voltage. Adapted from [26].	21
Fig. 13. AC-AC full bridge configuration.....	27
Fig. 14. Instantaneous states in a full bridge AC-AC converter. a) Instantaneous voltage is equal to the input voltage ($V_{out}=V_{in}$). b) and c) The instantaneous output voltage is zero ($V_{out}=0$). d) Instantaneous output voltage has inverse polarity with respect to the input voltage ($V_{out}=-V_{in}$).	28
Fig. 15. Switching strategy used to obtain same polarity output voltage. a) Input and Output voltages of single AC-AC converter; b) switching signals for switches sw_1 , sw_2 , sw_3 and sw_4 ; c) switching signals for switches sw_5 , sw_6 , sw_7 and sw_8	30
Fig. 16. Switching strategy used to obtain inverse polarity output voltage a) Input and output voltages of single AC-AC converter; b) switching signals for switches sw_1 , sw_2 , sw_3 and sw_4 ; c) switching signals for switches sw_5 , sw_6 , sw_7 and input sw_8	30
Fig. 17. Proposed Power Electronics Transformer with Dynamic Voltage and Angle Droop Control (PET-DVADC).	32
Fig. 18. Voltage realization example by the PET-DVADC topology.	33
Fig. 19. If the converter that produces $d_1n_1V_{AB}$ voltage fails, the converter that produces the voltage $d_3n_3V_{CA}$ can be used to achieve the same voltage V_A , increasing the reliability of the system.	34
Fig. 20. Vector diagram representation of the needed voltages to obtain an output voltage with 1.0 pu magnitude and 15° of phase shift.	38
Fig. 21. The phase angle is changed from 0 to 15 at $t_1 = 50$ ms, and magnitude from 1 p.u. to 1.1 p.u. at $t_2 = 100$ ms.	39
Fig. 22. Fractions of line to line voltages needed to achieve the output voltage changes.....	39
Fig. 23. Proposed Transactive Energy (TE) scheme for interconnected microgrids Angle Droop Control. Note: each microgrid is connected to the system at the point of common coupling (PCC) through a Power Router (PR). In this example, the PET-DVADC topology (discussed in detail in chapter 3) is shown to enable dynamic adjustments to PCC voltage magnitude and phase angle.	43

Fig. 24. Modified Angle Droop Control scheme. a) Phase angle droop controller. b) Voltage magnitude droop controller.	45
Fig. 25. Simulation scenario 1 for Transactive Energy application. After 0.2 seconds, the availability from renewable sources in μG_5 increases by 55 kW, and the DSO distributes the power to μG_1 (25 kW) and μG_2 (30kW), so they can reduce their fossil fuel needs.	47
Fig. 26. Simulation results for the proposed scenario, after $t = 0.1$ seconds, the system load changes from 25% to 85%, after $t = 0.2$ seconds, μG_5 provides 25kW, 12.1 kVAR to μG_1 and 30 kW, 14.5 kVAR to μG_2	48
Fig. 27. Simulation results for the proposed scenario, after $t = 0.2$ seconds, $\delta_1=9.95$, $\delta_2=10.4$ and $\delta_5=11.2$, while the other phase angles are set at $\delta_i=11.04$, enabling real power flow control. To control the reactive power, $V_1 = 260$, $V_2 = 264$, $V_5 = 280$, while the other magnitudes are set at $V_i = 271$ V.	49
Fig. 28. Simulation scenario 2 for Transactive Energy application. After 0.2 seconds, the availability from renewable sources in μG_5 increases by 50 kW, this can be used to completely eliminate the needs for fossil fuel sources that μG_2 needs.	51
Fig. 29. Simulation results for the proposed scenario, after $t = 0.2$ seconds, $\delta_2 = 10.1$ and $\delta_5 = 11.07$, while the other phase angles are set at $\delta_i = 11.02$, enabling real power flow control. To control the reactive power, $V_2 = 258$, $V_5 = 279$, while the other magnitudes are set at $V_i = 271$ V.	52
Fig. 30. Simulation results for the proposed scenario, after $t = 0.2$ seconds, $\delta_2 = 10.1$ and $\delta_5 = 11.07$, while the other phase angles are set at $\delta_i = 11.02$, enabling real power flow control. To control the reactive power, $V_2 = 258$, $V_5 = 279$, while the other magnitudes are set at $V_i = 271$ V.	53
Fig. 31. Conventional rooftop PV and battery energy storage system (BESS) interfaced to the grid via separate topologies.	56
Fig. 32. Proposed power electronics at the grid edge - a self-organizing converter with control intelligence at the edge of the electric distribution network.	57
Fig. 33. Proposed topology for the Power Electronics intelligence at the Network Edge (PINE) concept. Both roof-top solar PV and BESS are integrated into the dc-link.	60
Fig. 34. Detailed circuit Rooftop PV/BESS Interface.	61

Fig. 35. a) PV curve of the module selected for PINE system. b) IV curve of the selected module.	62
Fig. 36. a) PV curve of the PV array designed for PINE system. b) IV curve of the selected array.	63
Fig. 37. a) Rectifier mode; b) Regen mode. Adapted from [51].	65
Fig. 38. Current mode controller of Front end PWM converter in rectifier mode.	66
Fig. 39. Output PWM converter control scheme, energy budgeting is enabled by limiting output current. Each phase voltage is controlled in the same manner, with a phase shift of 180°	69
Fig. 40. Control strategy to maintain a nearly sinusoidal output voltage with on-linear loads. Adapted from [54].	70
Fig. 41. The voltage V_{DC} is maintained at the desired magnitude by controlling the phase shift between switching functions of H-bridges 1 and 2.	71
Fig. 42. The voltage V_{DC} is maintained by controlling the phase shift between signals 1 and 2. The phase shift signal is referred to as ϕ	72
Fig. 43. PINE converter operation during normal operating conditions, a) grid voltage variations V_{grid} and input current $I_{grid} * 10$; b) Output voltages V_A and V_B ; c) dc-link voltage; d) output phase currents I_A and I_B	74
Fig. 44. PINE converter operation during normal operating conditions, a) grid voltage variations V_{grid} and input current $I_{grid} * 10$; b) Output voltages V_A and V_B (with THD < 3%); c) dc-link voltage; d) output phase currents I_A and I_B	75
Fig. 45. PINE converter on regen mode, a) grid voltage V_{grid} and input current $I_{grid} * 20$; b) BESS voltage V_{BESS} and current I_{BESS} ; c) PV panels voltage V_{PV} and current I_{PV} ; d) output phase voltage V_A and current I_A	77
Fig. 46. Load profile of a residential load during a day (black curve). PV output power available profile (blue curve). Adapted from [60].	78
Fig. 47. Scenario at 6:30 AM, the load is near its peak, but the available power from the PV panels is low, the PINE system relies on the BESS and the grid to supply the requirements.	80

Fig. 48. PINE converter on scenario at 6:30 AM, a) grid voltage V_{grid} and input current $I_{\text{grid}}*40$; b) BESS voltage V_{BESS} and current I_{BESS} ; c) PV panels voltage V_{PV} and current I_{PV} ; d) output phase voltage V_A and current I_A*5	81
Fig. 49. Scenario at 12:00 PM, the load is near is significantly small, while the available power from the PV panels is near its peak, the PINE system charges the BESS and supplies power to the grid.	82
Fig. 50. PINE converter on scenario at 12:00 PM, a) grid voltage V_{grid} and input current $I_{\text{grid}}*40$; b) BESS voltage V_{BESS} and current I_{BESS} ; c) PV panels voltage V_{PV} and current I_{PV} ; d) output phase voltage V_A and current I_A*20	83
Fig. 51. Scenario at 6:00 PM, the load is near is its peak, while the available power from the PV panels is small, the PINE system uses the BESS as well as the PV system to supply the needed power to the load. The grid is fed 1 kVAR of reactive power for voltage support purposes.....	84
Fig. 52. PINE converter on scenario at 6:00 PM, a) grid voltage V_{grid} and input current $I_{\text{grid}}*20$; b) BESS voltage V_{BESS} and current I_{BESS} ; c) PV panels voltage V_{PV} and current I_{PV} ; d) output phase voltage V_A and current I_A*20	85
Fig. 53. Scenario at 11:00 PM, the load is significantly small, while there is no available power from the PV panels, since the electricity price is relatively low in this scenario, the PINE system charges the BESS from the grid. The grid is fed 2.5 kVAR of reactive power for voltage support purposes.	86
Fig. 54. PINE converter on scenario at 11:00 PM, a) grid voltage V_{grid} and input current $I_{\text{grid}}*20$; b) BESS voltage V_{BESS} and current I_{BESS} ; c) PV panels voltage V_{PV} and current I_{PV} (there is no available power from the PV system); d) output phase voltage V_A and current I_A*400	87
Fig. 55. Example system reconfiguration - post disaster.	88
Fig. 56. Energy budgeting scenario without the ability to disconnect each load. a) output voltage V_A and a desirable limit of 0.87 pu. b) Real and Reactive power limit, as disaster evolves.	89
Fig. 57. Energy budgeting scenario, each time the control produces a voltage below 0.87 pu, a non-essential load is disconnected, maintaining the voltage in the allowable range. a) output voltage V_A and a desirable limit of 0.87 pu. b) Real and Reactive power limit, as disaster evolves. c) non-essential loads disconnection steps.	90

Fig. 58. Experimental waveforms of the PINE converter. Channel 1 shows the input voltage, channel 2 shows the dc-link voltage, channel 4 shows the input current.	92
Fig. 59. Experimental waveforms for a step change input voltage. Channel 2 shows the dc-link voltage being regulated. Channel 1 shows the input current, notice the reduction due to constant power nature of PINE.....	92
Fig. 60. Experimental waveforms for energy budgeting. Energy budgeting is applied to limit the power to 200W. Channel 1 shows output voltage V_A . Channel 3 shows phase current I_A . Channel 2 shows output voltage V_B and channel 4 shows phase current I_B	93
Fig. 61. Future distribution power system with PINE technology installed at different locations. Only nodes where customers do not have PINE installed need to be regulated by Voltage Regulation Devices (VRD). Node A represents the load connection point at a PINE-interfaced house. Node B represents the grid connection point of a PINE-interfaced house. Node C represents the grid connection point of a non-PINE interfaced house.....	97
Fig. 62. Equivalent circuit of the Front End PWM converter fundamental component (60 Hz) connected to the grid.	98
Fig. 63. Equivalent circuit of the Front End PWM connected to the grid in the dq frame.	100
Fig. 64. Equivalent circuit of the Output PWM converter phase A. The phase B is modeled in a similar manner.	102
Fig. 65. A simple distribution system with/without PINE technology. (a) Traditional distribution system without PINE. (b) Distribution system with PINE.....	103
Fig. 66. System dynamics subject to the disturbance: phase voltage profile and reactive power support without PINE. (a) Voltage at node B. (b) Voltage at node C. (c) needed reactive power to regulate voltages at nodes B and C to meet minimum requirement i.e. 0.87 pu.	104
Fig. 67. System dynamics subject to the disturbance: phase voltage profile and reactive power support with PINE at node B. (a) Voltage at node B. (b) Voltage at node C. (c) needed reactive power to regulate only voltage node C (since PINE is regulating its own load voltage, node A) to meet minimum requirement i.e. 0.87 pu. (d) Voltage at node A, or load voltage of PINE interfaced load.....	105

Fig. 68. Test feeder used to simulate high penetration levels of PINE in a distribution feeder, based on the IEEE-37 test node feeder. Note: line impedances between nodes are specified in Appendix A. Adapted from [67].....	106
Fig. 69. Detailed configuration of each node containing loads (every blue node in Fig. 68).....	107
Fig. 70. Simulation results for a distribution grid with 100% PINE penetration level. As seen in Fig. 69, each node has three connected PINE enabled homes, one per phase; a) Grid voltages phases A, B and C; b) input current of PINE enabled homes in node 38; c) Real power of PINE enabled homes in node 38; d) dc-link voltage of PINE enabled homes in node 38.....	109
Fig. 71. Simulation results for a distribution grid with 100% PINE penetration level, for the switching converters simulation. As seen in Fig 69, each node has three connected PINE enabled homes, one per phase; a) Grid voltages phases A, B and C; b) input current of PINE enabled homes in node 38; c) dc-link voltage of PINE enabled homes in node 38; d) output voltages V_A and V_B of PINE load connected at node 38, phase A.	110

LIST OF TABLES

	Page
Table 1. Desired output voltage of phase A.	37
Table 2. Steps taken to show the system response when a TE operation is performed by the system between μG_1 , μG_2 and μG_5	50
Table 3. Electrical data of PV module selected for the PINE system.	61
Table 4. Simulation design parameters of PINE topology.	73
Table 5. Operating conditions of PINE during 4 different scenarios, as time of day changes.	79
Table 6. PINE converter experimental prototype parameters.	91

CHAPTER I

INTRODUCTION

The importance of Power Electronics for the future electrical grid

According to the International Energy Agency (IEA), global energy demand is expected to increase by 30% between 2017 and 2040, electrical energy makes up 40% of that rise in final consumption [1]. As shown in Fig. 1, it is expected that by 2040, solar will represent the largest share of renewable sources of energy [1]. Traditionally, electrical energy has been generated in centralized facilities using non-renewable resources. Due to environmental concerns and technology advancement, the usage of renewable sources such as solar and wind, has been increasing significantly, and is expected to keep increasing in the following decades. In fact, most of global investments in power plants are being done on renewable sources of energy.

Power electronics converters are needed in order to interface renewable sources of energy to the rest of the electric grid. This involves proper architectures and control techniques to maximize their potential and store the excess energy in energy storage systems (BESS) for peak shaving and capacity smoothing.

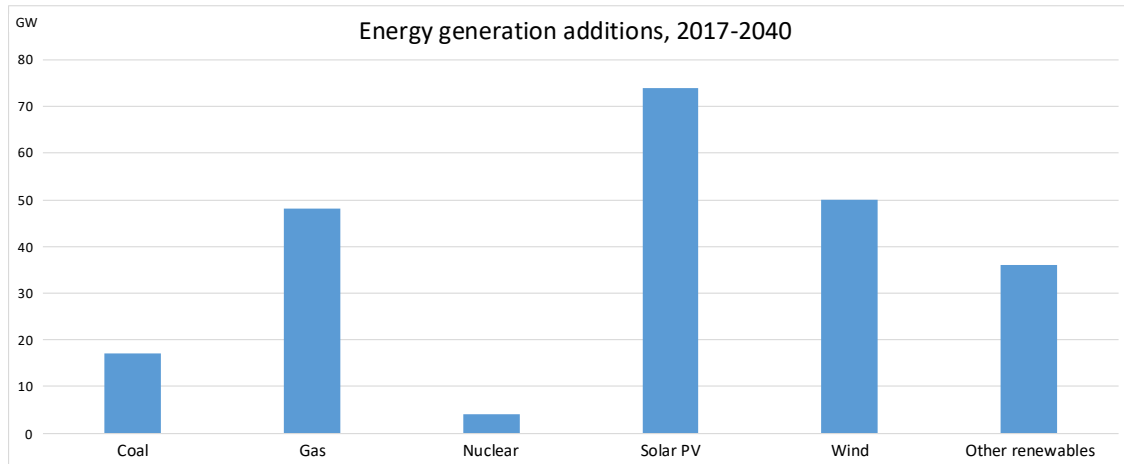


Fig. 1. The growing electricity demand is being supplied by renewable energy sources in an increasing rate. Adapted from [1].

Distributed Energy Resources impact on the future electrical grid

The rapid increase of Distributed Energy Resources (DERs) share represents one of the most challenging aspects in today's grid management, especially when dealing with their intermittent and unpredictable nature. Different aspects such as voltage quality and grid stability arise as DERs penetration increases.

These new challenges can be partially addressed by the use of microgrids, which are clusters of loads and sources that are controlled by an intelligent microgrid central controller (MGCC), and are connected to the utility grid through points of common coupling (PCC) [2-8]. In this manner, the Distribution System Operator (DSO) needs only to coordinate the microgrids interaction by controlling the complex voltage of each PCC [2]. Novel control strategies and power electronics topologies are needed to maintain proper voltage quality and grid stability.

Microgrids

Microgrid is a key element in renewable energy penetration. It consists of a cluster of several loads and DERs (such as distributed generators, storage devices, or controllable loads) controlled as an independent system, within clear electrical boundaries, as shown in Fig. 2. Microgrids can act as a single controllable entity as seen by the rest of the grid, it is connected to the rest of the network via the point of common coupling (PCC) [3]. By controlling the PCC voltage ($V_i \angle \delta_i$) the DSO can coordinate the power flow between microgrids.

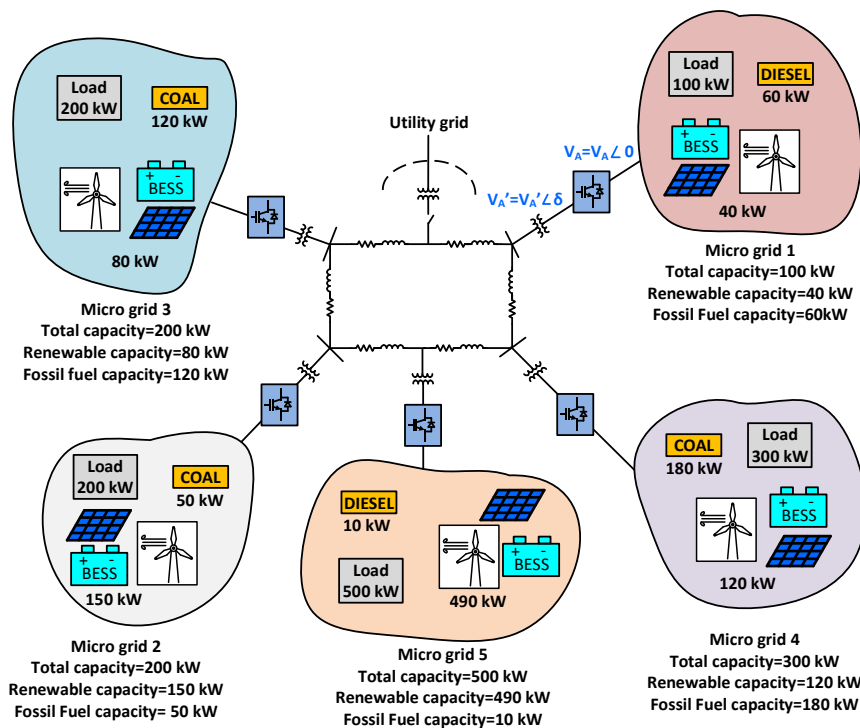


Fig. 2. Typical microgrid structure, the microgrid is connected to the rest of the grid via the Point of Common Coupling (PCC).

Microgrid control

Microgrid control has been studied extensively [4-9]. This dissertation considers the power flow coordination between islanded microgrids by the use of a recently introduced topology [10].

Generally, the power sharing control strategies for microgrid coordination can be classified in three main categories [2]:

Current sharing control

A centralized controller receives the information of the load current of the entire system. The controller then sets output current reference points for each Distributed Generator (DG). In this form of control, communication is crucial, and any interruption will lead to a collapse of the system [7, 9].

Master/slave

This control strategy involves assigning a Distributed Generator (DG) as the master. The master maintains a voltage reference (both magnitude and frequency) when the microgrids are working on islanded mode, the rest of the microgrids operate in PQ mode, injecting any desired active and/or reactive power (usually referred to as slaves) [4, 7]. Communication between the master and the slaves is essential, and the stability of the system highly depends on the master DG.

Droop control methods

Droop control methods for microgrid control emulate the operation principle of synchronous generators in traditional power systems. A mismatch between the input and the output power (electric active power) causes a change in the rotor speed, this change of

speed is translated in a deviation in voltage frequency. In a similar manner, a mismatch in the reactive power causes a deviation in the voltage magnitude [7]. The main advantage of droop control methods is that only local measurements are needed in order to control the power flow between microgrids, significantly reducing the communication needs. Droop control methods are further discussed in chapter 3.

Among microgrid power flow control strategies, droop control has the advantage that it is based on local measurements, significantly reducing communication needs. Droop control methods can be divided in two subcategories:

1. Frequency droop control
2. Angle droop control

Frequency Droop control

The frequency droop control strategy simulates the characteristics of synchronous generator based power systems, it manages the real power flow between microgrids by controlling their PCC voltage frequency, in a similar manner, frequency droop control manages the reactive power flow by controlling the voltage magnitude at the PCC. Fig. 3 shows examples of frequency droop control curves for both real (P vs ω) and reactive (Q vs V) power flow control.

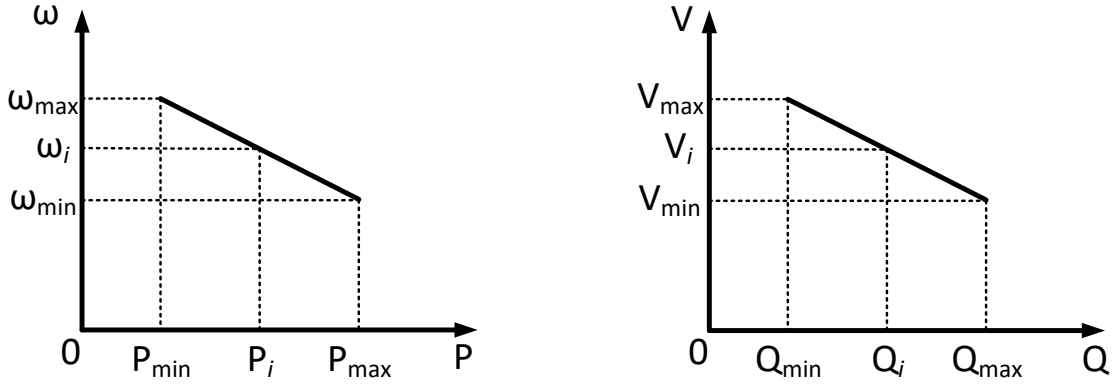


Fig. 3. Frequency droop control curves. a) Frequency (ω) vs Real Power (P) curve. b) Voltage (V) vs Reactive Power (Q) curve.

Where ω and V are the frequency and magnitude of the voltage of a given microgrid, respectively, P is the real power flow, and Q is the reactive power flow of the given microgrid. If the phase angle difference between microgrids is considered significantly small, the power flow between both microgrids can be given by equations (1.1) and (1.2):

$$\omega_i - \omega^* = m(P_i^* - P_i) \quad (1.1)$$

$$V_i - V^* = n(Q_i^* - Q_i) \quad (1.2)$$

Where: i is the i_{th} microgrid, ω_i , V_i are the PCC voltage angle and magnitude. P_i^* , Q_i^* are the nominal real and reactive power injections for the i_{th} microgrid. P_i , Q_i are the actual real and reactive power injections. ω^* , V^* are the reference frequency and voltage magnitude. To represent the sensitivity of indicating real and reactive power imbalance, the droop coefficients m (for frequency) and n (for voltage magnitude) are used, respectively.

It can be seen that by selecting the proper droop coefficients m and n , the frequency and voltage magnitude variation can be determined, this means that a compromise has to be done between power flow control accuracy and allowable variation of both parameters.

One of the main disadvantages of the frequency droop control strategy is that, since it controls the required real power by modifying the frequency, the steady state frequency of the system becomes load dependent, limiting proper load sharing.

Angle droop control

Recently, angle droop control methods are being studied. One of the main differences between frequency droop and angle droop control methods is the variable used to indicate the real power imbalance, frequency droop uses the PCC's frequency (ω), and angle droop uses the phase angle (δ) instead, as shown in the resultant equations given by (1.3) and (1.4):

$$\delta_i - \delta^* = \sigma_{\delta i}(P_i^* - P_i) \quad (1.3)$$

$$V_i - V^* = \sigma_{V i}(Q_i^* - Q_i) \quad (1.4)$$

Where: i is the i_{th} microgrid. δ_i, V_i are the PCC voltage angle and magnitude. P_i^*, Q_i^* are the nominal real and reactive power injections for the i_{th} microgrid. P_i, Q_i are the actual real and reactive power injections. δ^*, V^* are the reference phase angle and voltage magnitude. To represent the sensitivity of indicating real and reactive power imbalance, the droop coefficients $\sigma_{\delta i}$ (for frequency) and $\sigma_{V i}$ (for voltage magnitude) are used, respectively.

The coefficients $\sigma_{\delta i}$ and $\sigma_{V i}$ are calculated to set needed voltage magnitude and angle values for load sharing. These values are then used by the PR in each interface to

control the power sharing between microgrids in proportion to the ratings of each converter, as shown in equations (1.5) and (1.6).

$$\sigma_{\delta 1} \times P_1 = \sigma_{\delta 2} \times P_2 = \dots = \sigma_{\delta 5} \times P_5 \quad (1.5)$$

$$\sigma_{V1} \times Q_1 = \sigma_{V2} \times Q_2 = \dots = \sigma_{V5} \times Q_5 \quad (1.6)$$

Using the phase angle (δ) to control the real power flow allows the angle droop technique to provide proper load sharing among the microgrids without affecting the steady state frequency. Using angle droop control strategies allows to establish stability study results for the whole system.

In [2] a model reference control (MRC) based power sharing scheme is proposed to enable online modification of the set point for every operating condition. This ensures that real time stability and regulation requirements are met. Angle droop control requires phasor measurement units (PMUs) for angle referencing.

Power Electronics and solar Photovoltaics

The PV cell/module

The first photovoltaic solar cell was developed at the Bell Labs in the 1950's. The first PV applications were space satellites, and later low powered devices [12]. In the 1970's, the PV technology cost reduced to a point that made it available for other applications such as offshore gas and oil rigs, lighthouses, and even the residential applications started being considered as an option. [12].

The PV cell produces an electrical current by absorbing sunlight to raise electrons to a higher energy state. The PV cell then provides a path for these electrons to flow to an

external circuit, where the electricity is utilized [13]. A single PV cell can produce approximately half a volt, so they need to be connected in series to obtain a PV module, producing commercial voltages such as 12 V, 48 V, etc.

It is possible to represent the PV cell by the equivalent circuit shown in Fig. 4. The PV cell can be represented by a current source in parallel with a diode, with the addition of the shunt and series resistances (R_p and R_s , respectively) [14].

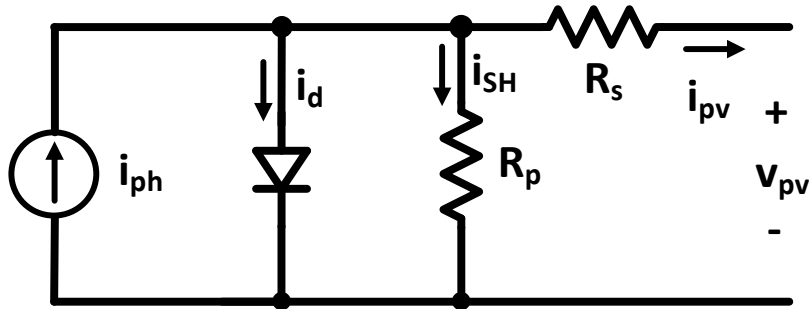


Fig. 4. PV cell equivalent circuit.

With the equivalent circuit, the PV cell module can be defined by equations 1.7 and 1.8:

$$i_{pv} = i_{ph} - I_o \left[\exp \left(\frac{v_{pv} + R_s i_{pv}}{V_t a} \right) - 1 \right] - \frac{v_{pv} + R_s i_{pv}}{R_p} \quad (1.7)$$

$$V_t = \frac{kT}{q} \quad (1.8)$$

Where: i_{pv} is the output current of the PV cell, i_{ph} is the photo-generated current, I_o is the saturation current of the diode, v_{pv} is the output voltage of the PV cell, R_s is the

series resistance of an individual cell, R_p is the shunt resistance of an individual cell, k is the Boltzmann constant, T is the cell temperature in Kelvin, and q is the electron charge.

The P-V and I-V curves

The P-V (power-voltage) and I-V (current-voltage) curves can be used to describe the electricity generation capabilities of a PV cell, module, or array of modules for a given set of weather conditions. Fig. 5 shows a typical set of I-V and P-V curves, including the most important parameters. It can be seen that the point of maximum power delivered by the PV system (P_{max}) is the point where the product of the current and voltage is the biggest. The voltage and current at this point are commonly referred to as V_{mp} and I_{mp} , respectively. The other two points of interest in the I-V curve are the current at zero output voltage (short circuit current I_{sc}) and the voltage where there is no current in the output (open circuit voltage V_{oc}), at these points, there is no power generated by the PV cell.

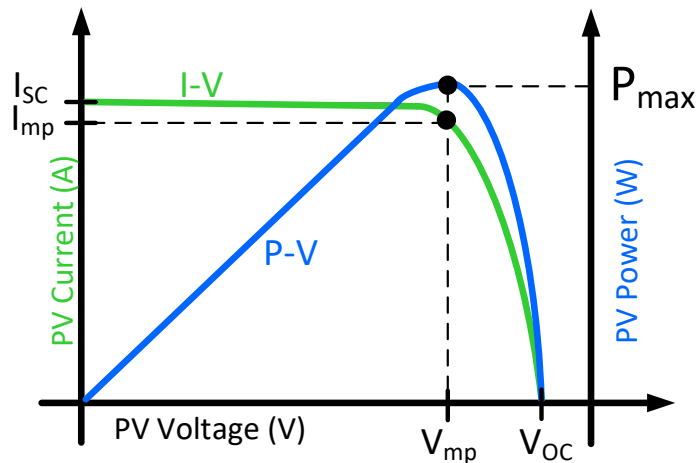


Fig. 5. Relationship between the power and voltage of the PV cell (P-V curve), and relationship between current and voltage of the PV cell (I-V curve).

Power converters to interface PV modules with BESS and the grid

PV modules need power electronic converters in order to be interfaced to the electrical grid. Traditionally, PV panels have been connected using centralized inverters interfacing a significant amount of PV modules that are connected in series (usually called a string) to avoid further voltage amplification. These strings are then connected in parallel using string diodes, to reach higher power outputs, the output of these arrangements are then processed by a power converter usually referred to as grid-tied inverter [15]. To reduce the cost of the total PV installation, several changes have been done to these power converters, as well as the PV module arrangements, including the addition of Battery Energy Storage Systems (BESS), transformer stages, etc.

The main reasons to integrate BESS into PV systems are cost reduction, peak shaving, and the possibility of operating in islanded mode, among others [16].

To improve the safety of the system, and improve the voltage amplification stages, transformers have been used, either with Low Frequency Transformers (LFT) or high Frequency Transformers (HFT).

Several PV/BESS system architectures have been used for grid interface, depending on the availability of BESS [15], the voltage levels at the input/output, the need for isolation, number of processing stages, efficiency, etc [16].

Based on these needs, 4 main categories have been proposed in [16] for residential PV/BESS architectures:

In line systems (Fig. 6)

The PV modules are interfaced with a DC-DC stage that can perform Maximum Power Point Tracker functions, and provide power to the BESS or the DC-AC stage via a dc bus. The DC-AC stage is then used to interface the dc bus to the utility grid, where all the loads are connected.

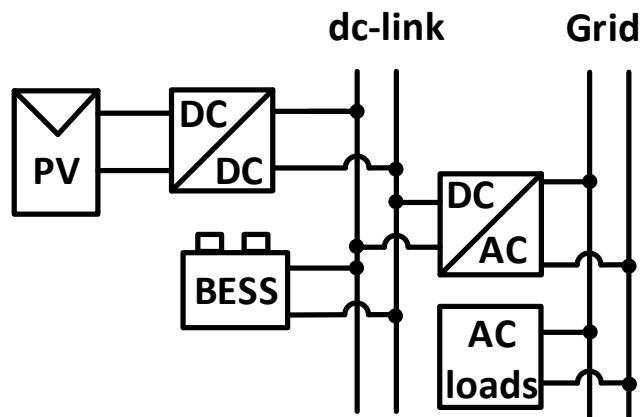


Fig. 6. In line systems. The BESS is connected directly to the dc-link, the PV system is interfaced with a DC-DC stage. The dc-link is then interfaced to the grid with a single DC-AC stage, where all the loads are connected. Adapted from [16].

DC coupled systems (Fig. 7)

The PV modules and the BESS are interfaced with separate DC-DC stages to the dc-link. The dc-link is then interfaced to the grid and the residential load using a single DC-AC stage. With separate DC-DC stages, the system has more flexibility to

charge/discharge the BESS with the PV and/or the grid, if the power converters are bi-directional.

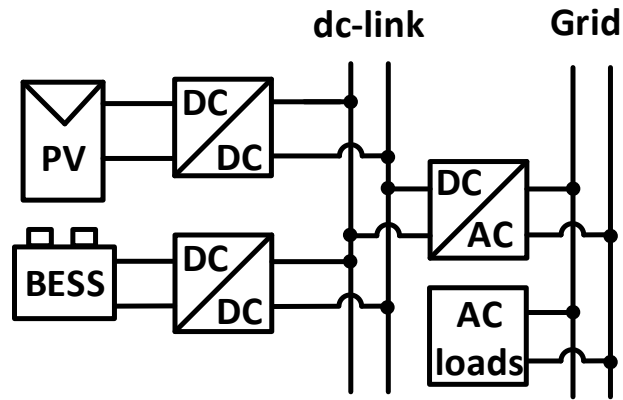


Fig. 7. DC coupled systems. Two separate DC-DC stages are needed to interface the PV and the BESS to the dc-link, this architecture improves flexibility to the BESS to be charged/discharged, the residential load is connected at the grid. Adapted from [16]

AC coupled systems (Fig. 8)

The PV modules and the BESS are interfaced independently to the grid. Each interface includes a DC-DC stage and a DC-AC stage. The absence of a common inverter results in a more modular approach that allows both the PV and the BESS to act independently from each other. This approach has the advantage of adding flexibility to the system by combining Electric Demand Side Management (EDSM) techniques used together with DERs [17].

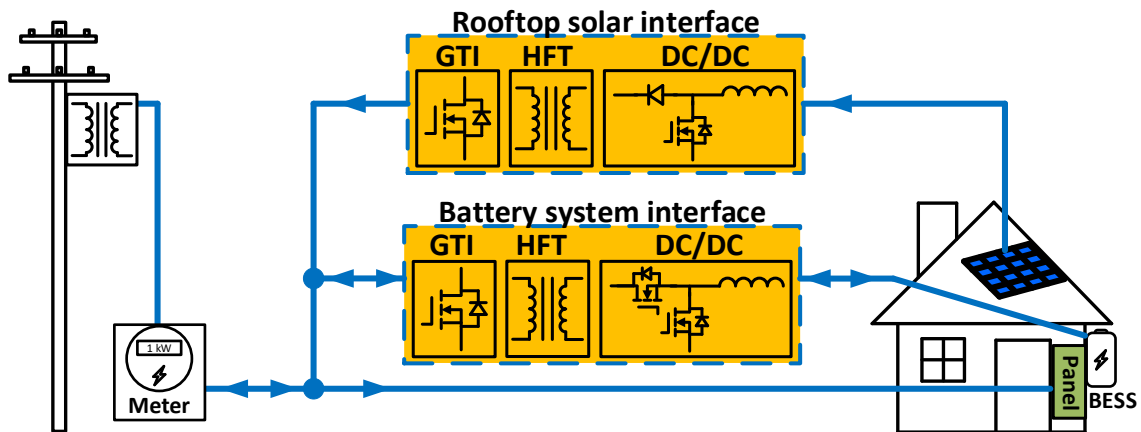


Fig. 8. AC coupled systems. The PV and the BESS are connected to the grid with independent DC-DC and DC-AC stages, this approach further improves flexibility, allowing techniques such as Electric Demand Side Management EDSM.

AC and DC coupled systems (Fig. 9)

In this configuration, the PV modules and the BESS are also interfaced with separate DC-DC stages to the dc-link. The dc-link is then interfaced to the grid using a single DC-AC stage, DC loads can be directly connected to the dc-link, and AC loads are connected to the grid. This increases the efficiency, since this eliminates the need for a rectification stage for DC loads.

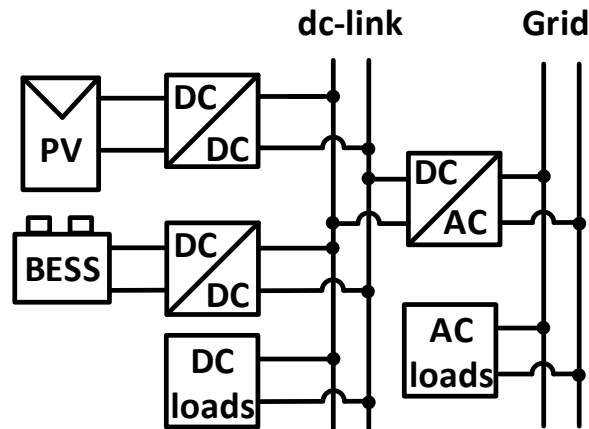


Fig. 9. AC and DC coupled systems. One single stage is used to interface the dc-link with the grid. Loads can be connected at either the dc-link or the grid side, further improving flexibility and efficiency. Adapted from [16].

The isolation stages can be applied at different stages. Some systems use transformers embedded in the DC-DC stages (using HFT), other systems use transformers to interface the DC-AC stage with the grid (using LFT) [15].

This dissertation proposes a new architecture for PV/BESS grid interface. The topology is shown in Fig. 10.

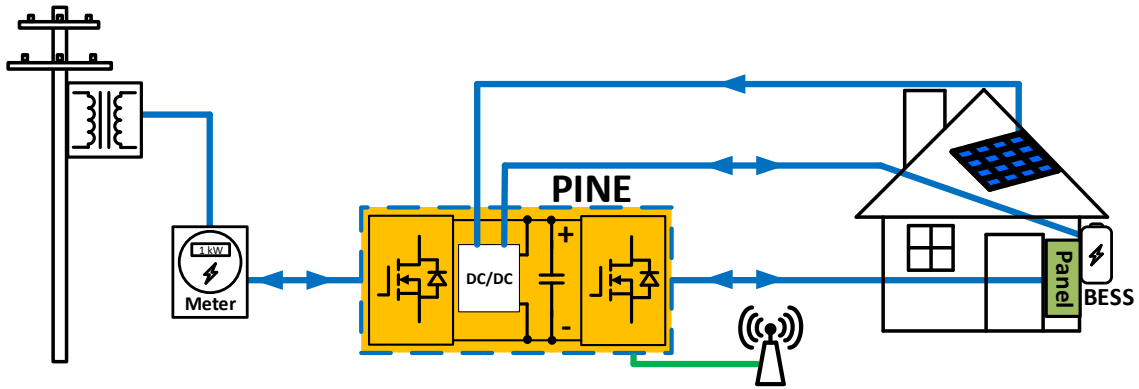


Fig. 10. Proposed topology for PV/BESS interface to the grid. Named Power Electronics Intelligence at the Network Edge, this topology is discussed in chapters 4 and 5.

Voltage quality

Voltage profile variations need to be tightly regulated because significant sags/swells might cause sensitive equipment malfunction [18]. Voltage magnitudes above or below the desired limit might cause problems such as overexcitation, insulation failure, and undesired circuit breaker trips.

As DERs penetration increase, standards regulating grid voltage need to change, not only to ensure new grid connected converters don't make the grid become unstable, but also to increase grid support advantages. Some of the new requirements are:

- Voltage Ride-Through
- Frequency Ride-Through
- Voltage support
- Frequency support

The stability of the future grid

The stability in conventional power systems have been extensively studied for decades [19]; however, the electrical grid of the future has fundamental differences with the present grid, more stability studies are needed to ensure the proper function of such grid [2, 20]. The main differences between the present and future grid include:

- High penetration of DERs, as such penetration increases, stability issues may arise, even if the stability is guaranteed for each individual microgrid.
- Since DERs are interfaced to the grid via power electronics converters instead of synchronous generators, they lack inertia, and frequency/phase angle may have a unacceptable levels of variation, affecting the system overall stability.
- Microgrids are interconnected at the distribution level, at lower voltages, the distribution lines' ratios X/R are lower, and they cannot be considered lossless.

Energy Routers

With increasing penetration of renewable energy sources such as, solar photovoltaic (PV), wind turbines and micro-turbines, there is an increasing need for control strategies and power electronics converters that result in dynamic and reliable power flow control. In order to control the power flow through two control areas there are several options, like tap-changing transformers and phase shifting transformers, which provide limited power flow. More complex and expensive options allow a wider control range are the Unified Power Flow Controller (UPFC), or the back-to-back HVDC link topologies.

Inverters and rectifiers control

Single phase grid connected voltage source inverters (VSI) are frequently used in DERs applications such as solar Photovoltaic [15], especially at the residential level. The demand of these systems is expected to increase as renewable energy penetration keeps growing. Usually, the VSIs and the grid are interfaced through a line reactor. In most of these systems, the input/output current is controlled, while regulating the dc-link voltage magnitude [21].

There are several techniques to achieve current control of grid connected converters. These techniques can be categorized in two main groups [21]:

- a) Stationary frame control
- b) Synchronous frame control

In this work, the synchronous reference frame (also referred to as dq frame) is used for simplicity. In the synchronous reference frame, ac quantities are processed as dc quantities, allowing the simplification of the control by enabling the use of PI controllers. In three phase systems, the transformation of the original system from the stationary frame to the synchronous frame is done in two steps:

- 1) Transform the three-phase system to a two axes system using equations (1.9) and (1.10) (known as the Clarke transformation). The two axes are commonly referred to as α and β .

$$X_{\alpha} = \frac{2}{3} \left[X_a - \frac{1}{2} X_b - \frac{1}{2} X_c \right] \quad (1.9)$$

$$X_{\beta} = \frac{2}{3} \left[0 + \frac{\sqrt{3}}{2} X_b - \frac{\sqrt{3}}{2} X_c \right] \quad (1.10)$$

Where a, b and c represent the three phase component magnitudes.

2) Transform the two axes system in stationary frame to the synchronous frame using equations (1.11) and (1.12) (known as the Park transformation). The new variables are commonly referred to as d and q .

$$X_d = X_\alpha \cos(\omega t) + X_\beta \sin(\omega t) \quad (1.11)$$

$$X_q = -X_\alpha \sin(\omega t) + X_\beta \cos(\omega t) \quad (1.12)$$

Where ω is the angular velocity of the system, and t is time.

However, for single phase systems, there is only one phase available for every variable, and in order to obtain the dq components, a minimum of two orthogonal variables are needed. To obtain a second orthogonal component, several techniques can be used. One of the most widely used techniques is the use of the all pass filter (APF), as shown in equation 1.13. By processing the original single phase variables through this APF, a set of virtual components that are orthogonal to those in the single phase system are created [22, 23].

$$APF(s) = \frac{\omega_1 - s}{\omega_1 + s} \quad (1.13)$$

Where ω_1 is the fundamental frequency of the system.

The APF can be seen as a transport delay block, which produces a phase shift of 90 degrees with respect to the original signal. The original signal is referred to as α , while the orthogonal signal is named β . In this fashion, the Park transformation (equations 1.11 and 1.12) can be used to obtain the dq components.

With dc quantities, conventional PI controllers can be used, and the output quantities of each controller are then transformed back to the stationary ($\alpha\beta$) frame using

equations (1.14) and (1.15) (also known as the reverse Park transformation) in order to obtain the control signals for the converters:

$$X_{\alpha} = X_d \cos(\omega t) - X_q \sin(\omega t) \quad (1.14)$$

$$X_{\beta} = X_d \sin(\omega t) + X_q \cos(\omega t) \quad (1.15)$$

The signal X_{α} is usually used as the modulation signal for the converter, and the signal X_{β} is discarded. The control strategy for each topology is discussed in more detail in the corresponding chapter.

Grid voltage phase detection

Grid connected VSIs need to obtain information from the utility grid, such as phase, amplitude and frequency of the grid voltage in order to synchronize the power converter with the utility grid, this enables the accurate generation of the reference signals for current control. This information is obtained by a Phase-Locked-Loop (PLL) structure.

Fig. 11 shows the needed PLL structure used for grid connected VSIs [24, 25]. It can be seen that the phase detection is done by synchronizing the grid voltage vector with the reference frame of the PLL. The reference of the q component of the grid voltage is set to zero in order to lock the PLL output with the grid voltage phase angle [25].

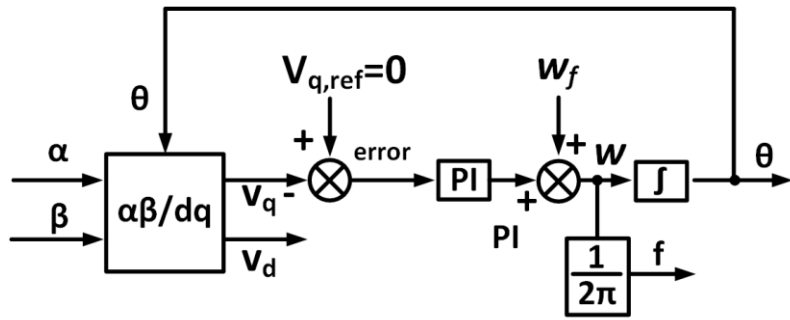


Fig. 11. General structure of PLL for grid synchronized converters. Adapted from [25].

As previously mentioned, in single phase systems, in order to use the Clarke transformation, an orthogonal signal needs to be generated, usually, this is obtained by the use of an APF that introduces a 90° phase shift between the original and the needed signal.

In PLL applications, this simple method presents several issues, such as: frequency dependency and poor filtering of the orthogonal system [25]. In this work, the strategy to generate the orthogonal signal is based on [26], as shown in Fig. 12.

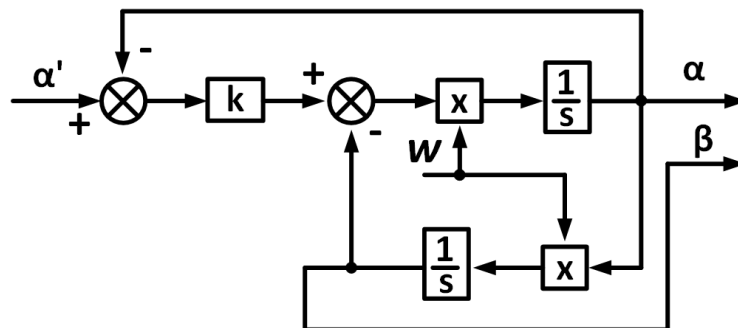


Fig. 12. Strategy to create the orthogonal component of the grid voltage. Adapted from [26].

Where k is a proportional gain, α' represents the input signal (grid voltage) and α and β are the needed components for the PLL to determine the phase, amplitude and frequency of the utility voltage.

Research Objective

It is evident that in order to meet with the increasing energy demand, while reducing non-renewable sources dependence, reliability, stability and efficiency concerns must be addressed. In response to these needs, this dissertation aims to propose and analyze new control schemes, as well as the needed power electronics converters to enable them.

Traditional voltage control is done in two separate stages, a rectifier stage and the inverter stage, using a dc-link capacitor to interface them. In order to avoid the bulky dc-link stage, and reduce the number of needed conversion stages, AC-AC converters have been implemented where only voltage magnitude regulation is desired. In this dissertation, a new topology named Power Electronics Transformer with Dynamic Voltage and Angle Droop Control (PET-DVADC) is introduced.

The proposed topology is designed to enable a modified angle droop control strategy, also described and analyzed in this work. The PET-DVADC topology generates the needed voltages by using fractionally rated transformers and AC-AC converters, eliminating the need for rectifier and dc-link stages, aiming to improve efficiency, reliability and cost.

The modified angle droop control strategy increases the flexibility for power flow control in microgrid applications. Enabling the possibility of Energy Transactions between

peers (or peer-to-peer energy transactions). This dissertation studies the application of this strategy, as well as the PET-DVADC in a setup consisting in 5 microgrids.

Since the voltage variation issue is one of main challenges for increased penetration of renewable sources of energy, this dissertation proposes and discusses a new topology to interface a residential PV/BESS system with the distribution grid. The resultant topology is called Power Electronics Intelligence at the Network Edge (PINE), besides addressing the voltage variation issue, this topology aims to improve the distribution grid thanks to other advantages presented and discussed in this work.

An average model of the proposed topology is developed to investigate its effects in a distribution grid with high penetration levels of power electronics. A test feeder based on the IEEE-37 test node feeder is developed to simulate a case where all the residential loads are interfaced using a PINE converter.

The proposed control strategies and power electronics topologies aim towards the energy internet concept by improving microgrid interface control accuracy, allowing the increase of residential PV penetration, and adding smart grid features to existing grids. All the topologies have bi-directional capabilities.

Structure of dissertation

This dissertation is divided in five chapters. The first chapter discusses current microgrid control strategies, as well as usual topologies and control schemes used to interface PV/BESS with the grid.

The second chapter proposes a new power electronics realization to enable power flow control by controlling the PCC output voltage magnitude and phase using phase

shifting transformer techniques. The resultant topology is called Power Electronics Transformer with Dynamic Voltage and Angle Droop Control (PET-DVADC), the topology is designed to enable a modified angle droop control technique discussed in chapter 3. Simulation results are presented.

The third chapter proposes a modified angle droop control technique that allows a more accurate control of active/reactive power, enabling peer-to-peer energy transactions (or Transactive Energy). Simulation results using a design example consisting of 5 microgrids with different penetration levels of renewable energy are presented.

The fourth chapter proposes a power electronics topology that interfaces a residential load, including a rooftop solar PV/Battery system to the grid, enabling several advantages that contribute to the electrical grid of the future, the resultant topology is named Power Electronics Intelligence at the Network Edge (PINE) simulation and hardware results are presented.

The fifth chapter discusses the implementation of PINE in the distribution grid. High penetration levels of PINE interfaced loads are simulated. The advantages of a distribution system without PINE at every node are also presented.

Finally, chapter 6 provides a summary of the research work reported in this dissertation and finalizes with recommendations for further research topics in this area.

CHAPTER II

POWER ELECTRONICS TRANSFORMER WITH DYNAMIC VOLTAGE AND ANGLE DROOP CONTROL FOR MICROGRID APPLICATIONS*

This chapter introduces a power router (PR) that enables power flow control between microgrids without the use of a dc-link. The proposed PR is realized by augmenting a fractionally rated transformer with AC-AC converter blocks (also fractionally rated). This leads to a topology which is named as Power Electronics Transformer with Dynamic Voltage and Angle Droop Control (PET-DVADC). Design details of the PET-DVADC concept are discussed. The equations used to obtain the required duty cycles are also presented.

A design example is used to obtain simulation results for a desired voltage needed from the proposed topology.

Introduction

In the traditional electrical grid, there is limited capability of power flow control between different control areas. As the penetration of distributed energy resources increases, the need for accurate and reliable control over the power flow between different control areas needs to increase. In today's current electrical grid, the limited control of power flow control is the energy router. In [27], a theoretical analysis for one option of energy router, the Controllable Network Transformer (CNT) is developed.

* © 2018 IEEE. Reprinted, with permission from [10] Jorge A. Ramos-Ruiz, Prasad Enjeti, Le Xie, "Peer-to-peer Energy Transaction in Microgrids with Power Electronics Enabled Angle Droop Control" in IEEE Electronic Power Grid (eGRID), November 2018, pp. 1-6.

The CNT is a low cost option, optimized for only magnitude control, having real power flow control limited capabilities. In [28], a different energy router technology scheme is presented, called the compact dynamic phase angle regulator (CD-PAR), it is optimized for real power flow control, but compromises the reactive power flow accuracy. The energy router is the main component for making a usual distribution grid “smart”, by enabling power flow control at any given node. In this chapter, a new topology for an energy router PET-DVADC is proposed.

AC-AC converters

Traditionally, AC-AC conversion has been done in two separate stages, a rectifier stage and the inverter stage. The rectification stage is usually implemented by using either a diode rectifier or a PWM rectifier, using a dc-link stage to interface them. This approach is needed when variable frequency is desired. In order to avoid the dc-link stage, AC-AC converters can be implemented where only voltage magnitude regulation is desired.

In recent years, several AC-AC topologies have been proposed. In [29], an AC-AC converter with high efficiency and bi-directional capabilities is proposed, but the main limitation is that the output voltage is fixed, so there is no control on the output voltage. Other common topologies are the buck and boost types [30], they can only provide unipolar output voltage, which reduces the flexibility of the system.

In this work, a full bridge configuration is used to achieve the AC-AC conversion, as shown in Fig. 13. This allows for more flexibility in the output voltage magnitude control. The topology can increase or decrease the input voltage, it can also provide a

positive or negative voltage, as shown in Fig. 14. The mentioned configuration has been used for Solid State Transformer applications [31].

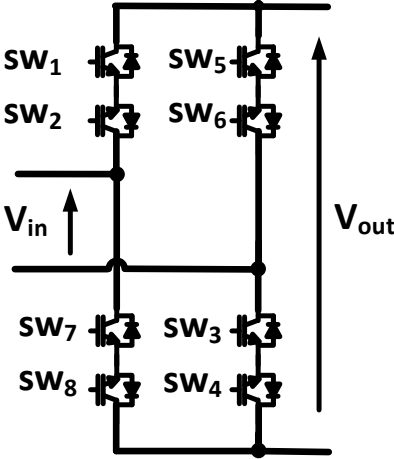


Fig. 13. AC-AC full bridge configuration.

The full bridge configuration enables three different states in the output voltage. It can be seen that in order to obtain a switch that can block the voltage in both directions, two regular switches can be connected in an anti-series fashion. Fig. 14 shows the instantaneous voltage states and how they are obtained.

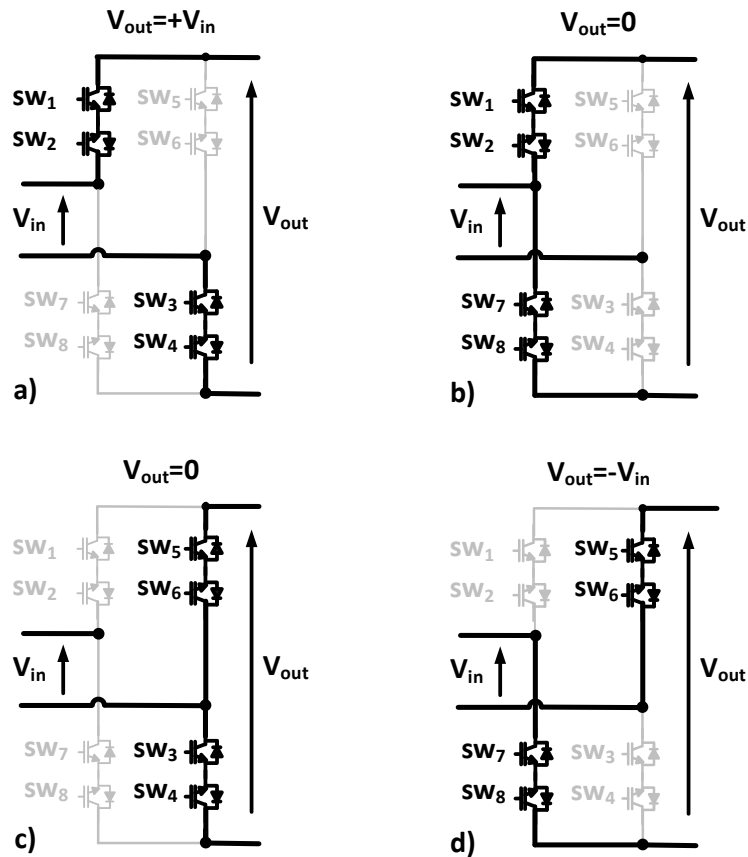


Fig. 14. Instantaneous states in a full bridge AC-AC converter. a) Instantaneous voltage is equal to the input voltage ($V_{out}=V_{in}$). b) and c) The instantaneous output voltage is zero ($V_{out}=0$). d) Instantaneous output voltage has inverse polarity with respect to the input voltage ($V_{out}=-V_{in}$).

As shown in Fig. 14, the three instantaneous voltage states can be obtained using 4 different combinations:

- When switches sw_1 , sw_2 , sw_3 , and sw_4 are ON, while switches sw_5 , sw_6 , sw_7 and sw_8 are OFF, the output voltage V_{out} has the same polarity as V_{in} ($V_{out}=V_{in}$). This is depicted in Fig. 14a.

- Two different combinations will produce a zero output voltage ($V_{out}=0$). When switches sw_1 , sw_2 , sw_7 and sw_8 are ON, and sw_5 , sw_6 , sw_3 , and sw_4 are OFF, as shown in Fig. 14b. The inverse combination will also produce an output voltage equal to zero, as shown in Fig. 14c.
- When switches sw_5 , sw_6 , sw_7 , and sw_8 are ON, while switches sw_1 , sw_2 , sw_3 and sw_4 are OFF, the output voltage V_{out} has the inverse polarity as V_{in} ($V_{out}=-V_{in}$). This is depicted in Fig. 14d.

The switching signals used to obtain the different voltages are shown in Figs. 15 and 16. It can be seen that to produce an output voltage with the same polarity as the input, the instantaneous voltage is made to alternate between $V_{out}=V_{in}$ and $V_{out}=0$, as shown in Fig. 15. To produce a voltage with the inverse polarity, the output voltage is made to alternate between $V_{out}=-V_{in}$ and $V_{out}=0$, as shown in Fig. 16. By controlling the proportion between $V_{out}=\pm V_{in}$ and $V_{out}=0$ states, the magnitude of the output voltage can be controlled.

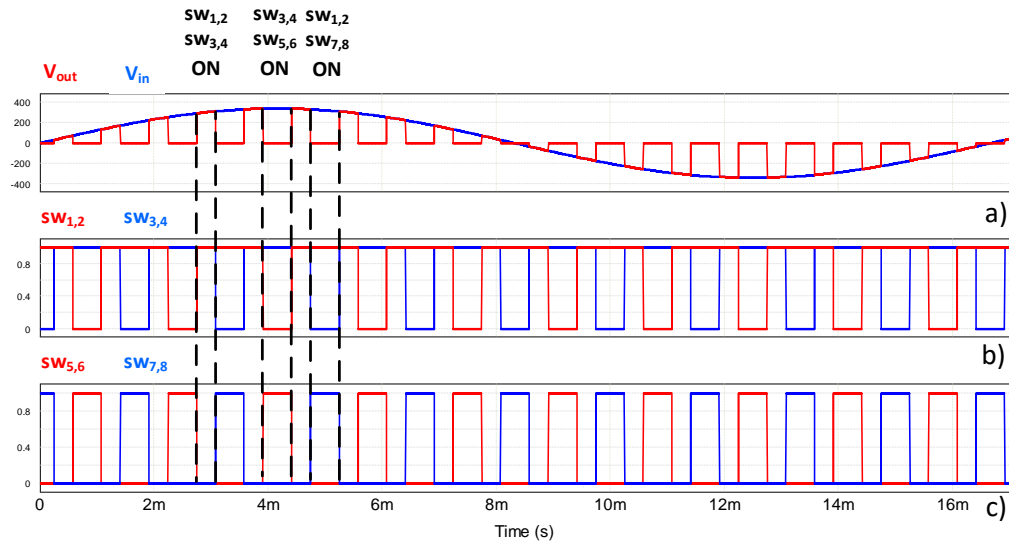


Fig. 15. Switching strategy used to obtain same polarity output voltage. a) Input and Output voltages of single AC-AC converter; b) switching signals for switches sw₁, sw₂, sw₃ and sw₄; c) switching signals for switches sw₅, sw₆, sw₇ and sw₈.

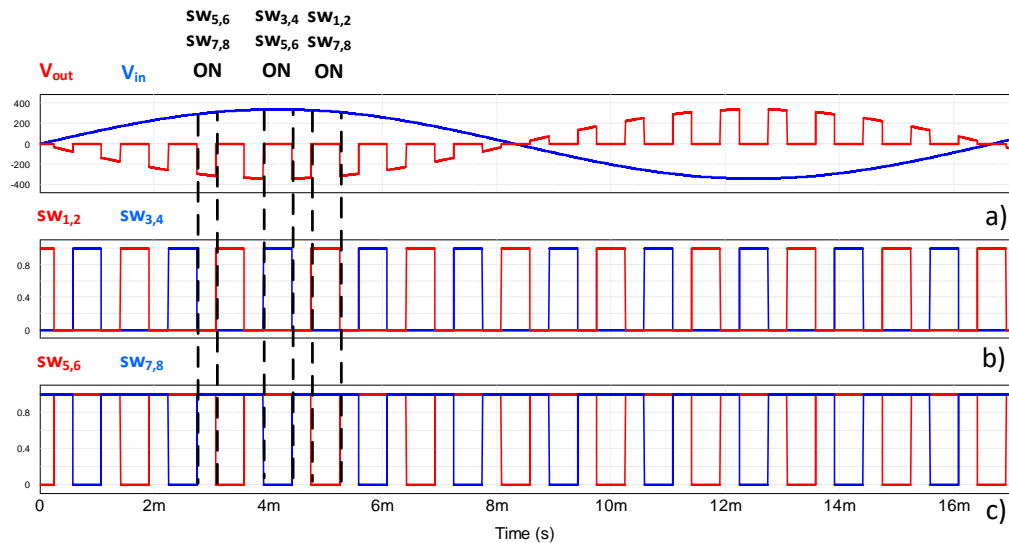


Fig. 16. Switching strategy used to obtain inverse polarity output voltage a) Input and output voltages of single AC-AC converter; b) switching signals for switches sw₁, sw₂, sw₃ and sw₄; c) switching signals for switches sw₅, sw₆, sw₇ and sw₈.

Proposed topology for PET-DVADC

Fig. 17 shows the proposed topology for PET-DVADC. It consists of a delta-star connected transformer with three primary and nine fractionally rated secondary windings (three per phase), each one connected to an also fractionally rated AC-AC converter. The desired voltage for each phase is then obtained from equations (2.1-2.3).

$$V'_A = V_A \pm d_1 n_1 V_{AB} \pm d_2 n_2 V_{BC} \pm d_3 n_3 V_{CA} \quad (2.1)$$

$$V'_B = V_B \pm d_3 n_3 V_{AB} \pm d_1 n_1 V_{BC} \pm d_2 n_2 V_{CA} \quad (2.2)$$

$$V'_C = V_C \pm d_2 n_2 V_{AB} \pm d_3 n_3 V_{BC} \pm d_1 n_1 V_{CA} \quad (2.3)$$

Microgrid Distribution Voltage	Fractionally Rated Transformer	AC-AC Converter (fractional rated) with bi-directional switches	Medium Voltage Transformer	Medium Voltage Microgrid Interface Point of Common Coupling
--------------------------------------	--------------------------------------	---	----------------------------------	--

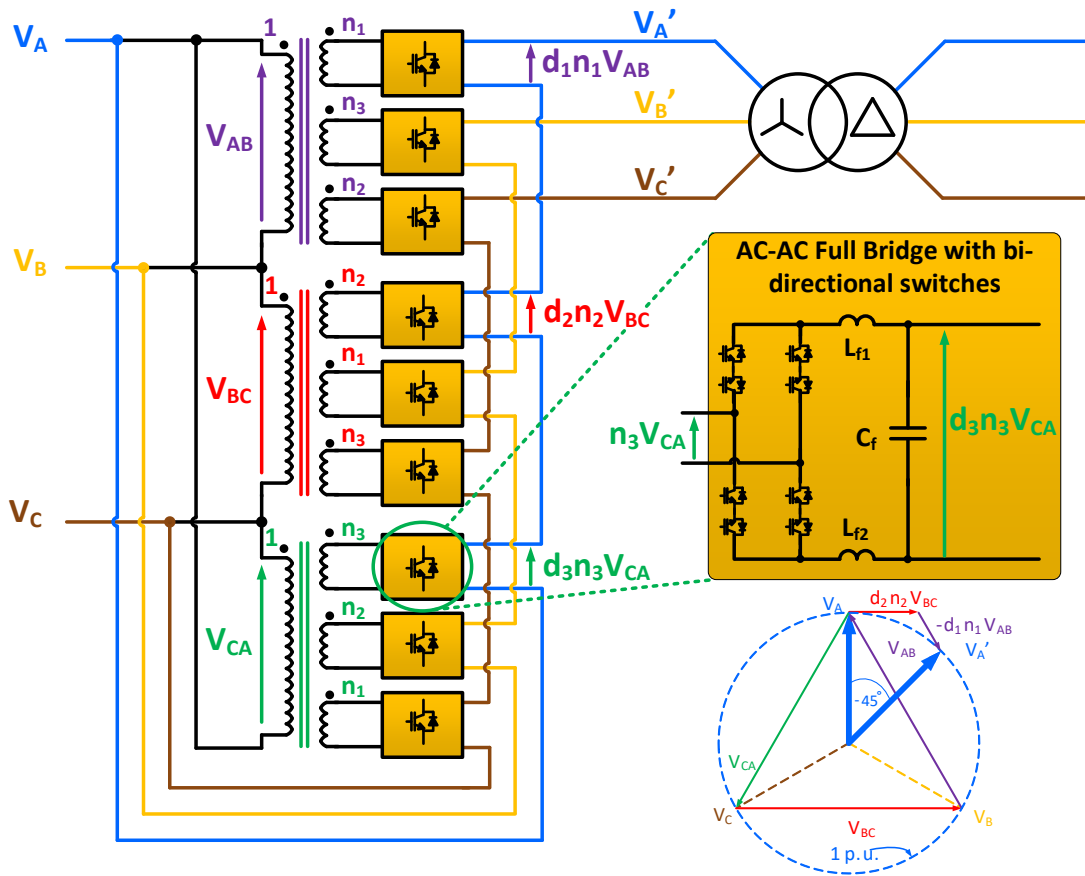


Fig. 17. Proposed Power Electronics Transformer with Dynamic Voltage and Angle Droop Control (PET-DVADC).

Fig. 18 shows in more detail an example of the process to obtain the desired voltage. It can be seen that the more efficient way to obtain a $+45^\circ$ phase shift with no change in magnitude is to add a fraction of V_{BC} ($d_2 n_2 V_{BC}$) and then subtract a fraction of

V_{AB} ($-d_1 n_1 V_{AB}$). These fractions are achieved by multiplying the voltages by their respective transformer turn ratio and duty ratios.

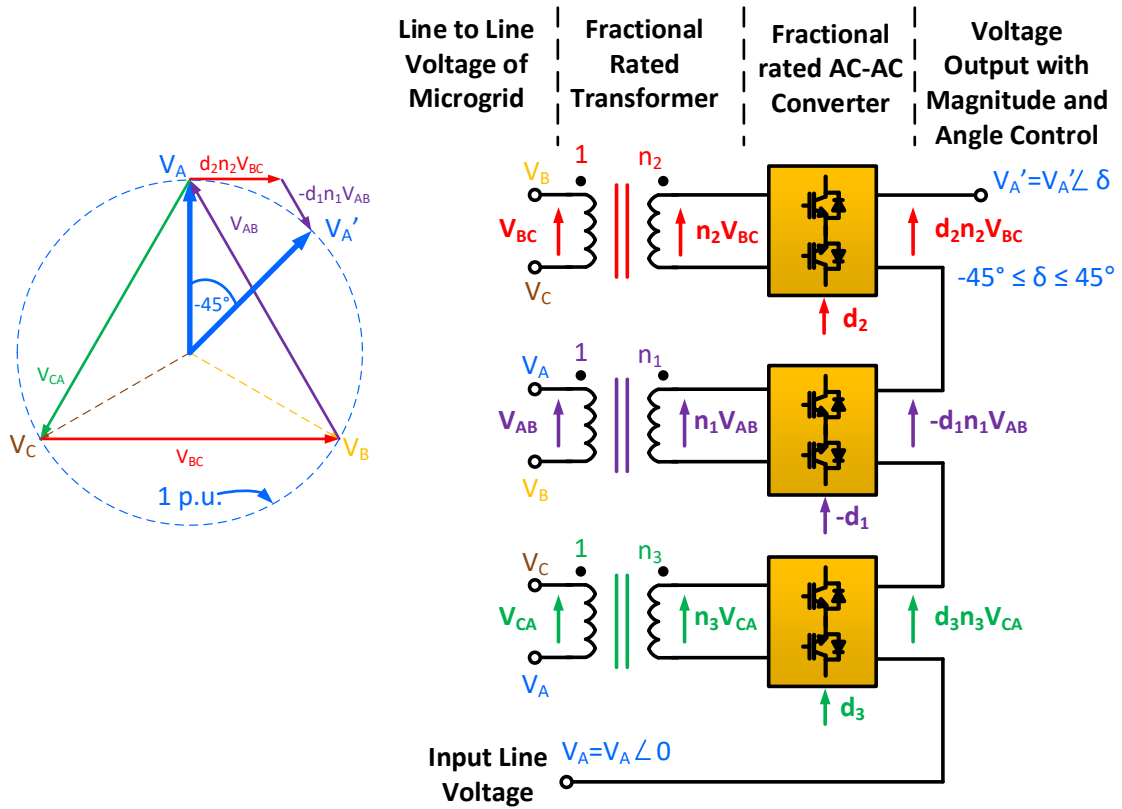


Fig. 18. Voltage realization example by the PET-DVADC topology.

Different combinations can result in the same voltage, so a voltage V_{CA} ($\pm d_3 n_3 V_{CA}$) can also be added/subtracted to obtain the same result, this will in turn improve the systems reliability, so if one of the AC-AC converters failed, the needed voltage can still be achieved, as shown in Fig. 19.

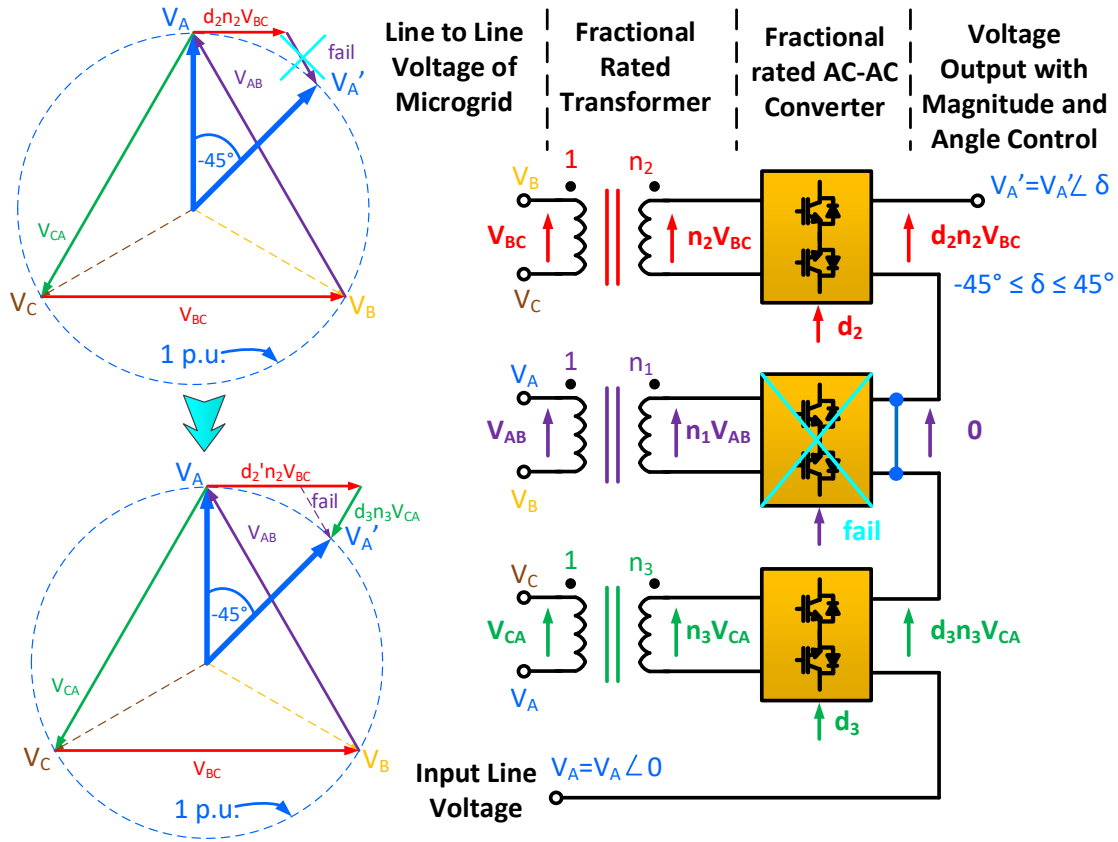


Fig. 19. If the converter that produces $d_1 n_1 V_{AB}$ voltage fails, the converter that produces the voltage $d_3 n_3 V_{CA}$ can be used to achieve the same voltage V_A' , increasing the reliability of the system.

Duty cycle calculations

The required duty cycles to obtain a desired voltage by the PET-DVADC are obtained using equations (2.4 - 2.14).

$$V_A = V_i * \sin(\omega t + \delta_i) \quad (2.4)$$

$$V_B = V_i * \sin(\omega t + \delta_i - 120) \quad (2.5)$$

$$V_C = V_i * \sin(\omega t + \delta_i - 240) \quad (2.6)$$

$$V_{AB} = \sqrt{3} * V_i * \sin(\omega t + \delta_i + 30) \quad (2.7)$$

$$V_{BC} = \sqrt{3} * V_i * \sin(\omega t + \delta_i + 270) \quad (2.8)$$

$$V_{CA} = \sqrt{3} * V_i * \sin(\omega t + \delta_i + 150) \quad (2.9)$$

$$x = V_i * \cos(\delta_i) \quad (2.10)$$

$$y = V_i * \sin(\delta_i) \quad (2.11)$$

Assuming a small angle δ_i , the ideal combination to obtain the desired voltage is:

$$d_1 n_1 = \frac{x - V_{base}}{\sqrt{3} V_{base} \cos(30)} \quad (2.12)$$

$$d_2 n_2 = \frac{y - (d_1 n_1 \sqrt{3} V_{base} \sin(30))}{\sqrt{3} V_{base} \sin(270)} \quad (2.13)$$

$$d_3 n_3 = 0 \quad (2.14)$$

Where: i is the i th microgrid, δ_i and V_i are the PCC desired voltage angle and magnitude, V_{base} is the system base voltage, x is the needed voltage in phase component, y is the needed voltage orthogonal component, V_A , V_B and V_C are the phase voltages, V_{AB} , V_{BC} , and V_{CA} are the line-to-line voltages, d_i is the corresponding duty cycle and n_i is the corresponding transformer turns ratio.

Example system to optimize transformer ratings

The proposed PET-DVADC topology enables a wide range of control for voltage magnitude and phase angle. In this section, a design example to optimize the power ratings of the transformer windings is proposed.

For the proposed application, the whole system's installed capacity is $P_{3-phase} = 1300$ kW and $Q_{3-phase} = 630$ kVAR. Designing a system to be able to provide the required power to the grid, assuming it has a voltage magnitude of 1.0 pu and a phase angle of 0,

will result in a required voltage magnitude and phase angle for a PET-DVADC (single phase). This voltage can be estimated with equations (2.15) and (2.16).

For a 13.2 kV system, with a 48-mile length, the chosen parameters are $R=0.547\Omega/\text{mile}$, and $L=0.4360\text{mH}/\text{mile}$, for simplicity of calculations, the line resistance is neglected.

$$\frac{(V_i)*(V_{grid})}{X_L} * \sin\delta = P_{1-phase} \quad (2.15)$$

$$\frac{V_i^2 - (V_i * V_{grid} * \cos\delta)}{X_L} = Q_{1-phase} \quad (2.16)$$

The required voltage phase and magnitude are estimated to be $\delta < 4^\circ$, and $V_i < 1.03$ pu, respectively. In the low voltage side, this translates to a single phase voltage of: $V_A' < 273.5$ V. With the magnitude and phase angle known, the required terms for duty ratio multiplied by turns ratio ($d_x n_x$) are calculated using equations 2.10-2.14, resulting in: $d_3 n_3 = 0.018$, and $d_2 n_2 = -0.032$.

The power ratings of the proposed PET-DVADC topology depend on the output voltage requirements, both phase angle and voltage magnitude. As the requirement of phase angle difference increases, the required voltages also increase. In a similar manner, as the requirement of voltage magnitude difference increases, the required voltages will increase. This is shown in equations 2.4 - 2.16.

For this system, a turns ratio of $n:n_1$, $n:n_2$, and $n:n_3$ of 0.1 is proposed to have enough flexibility, meaning the maximum voltage that could be present in the secondary side of the fractionally rated transformer results in 46 V, with a peak value of 65V.

Simulation results

An example system was designed and simulated in PSIM for a phase voltage $V_A = 256 \text{ V}$, with a change in phase angle at $t = 50 \text{ ms}$, and a change in magnitude at $t = 100 \text{ ms}$. The main purpose is to show how the controller reacts when the magnitude and/or phase angle of the interface voltage needs to be adjusted dynamically. Table 1 summarizes the parameters used for the simulation.

Table 1. Desired output voltage of phase A.

Parameter	$t < t_1$	$t_1 < t < t_2$	$t > t_2$
Phase voltage V_A	1 pu	1 pu	1.1 pu
Phase angle	0°	15°	15°
Nominal voltage per phase	$460 / \sqrt{3}$		

Fig. 20 shows the vector diagram of the needed duty cycles calculated to obtain the desired output voltage after $t_2=100 \text{ ms}$. It can be seen that the optimal combination to achieve the mentioned voltage is by using the windings n_2 and n_3 .

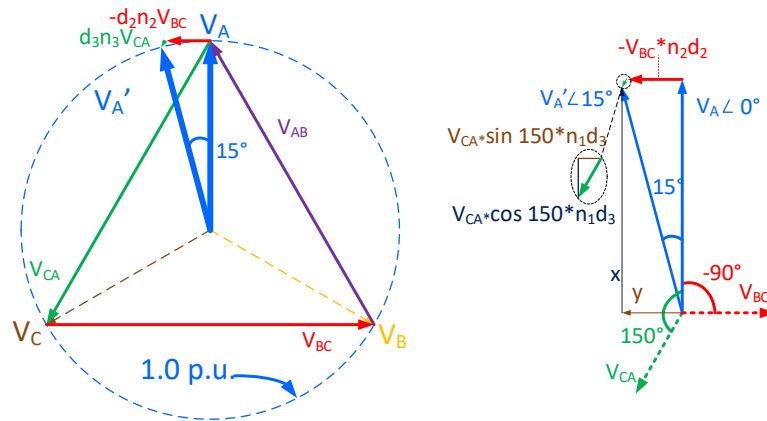


Fig. 20. Vector diagram representation of the needed voltages to obtain an output voltage with 1.0 pu magnitude and 15° of phase shift.

Figs. 21 and 22 show the simulation results for the proposed system. As shown in table 1, a change in phase angle δ is made between 0 and 15 at $t_1 = 50$ ms, and a change in magnitude from 1 pu to 1.1 pu is then made at $t_2 = 100$ ms. Fig. 21 shows the needed fractions of voltages V_{BC} and V_{CA} needed to achieve these angles/magnitudes, this is realized by changing duty cycles d_2 and d_3 respectively.

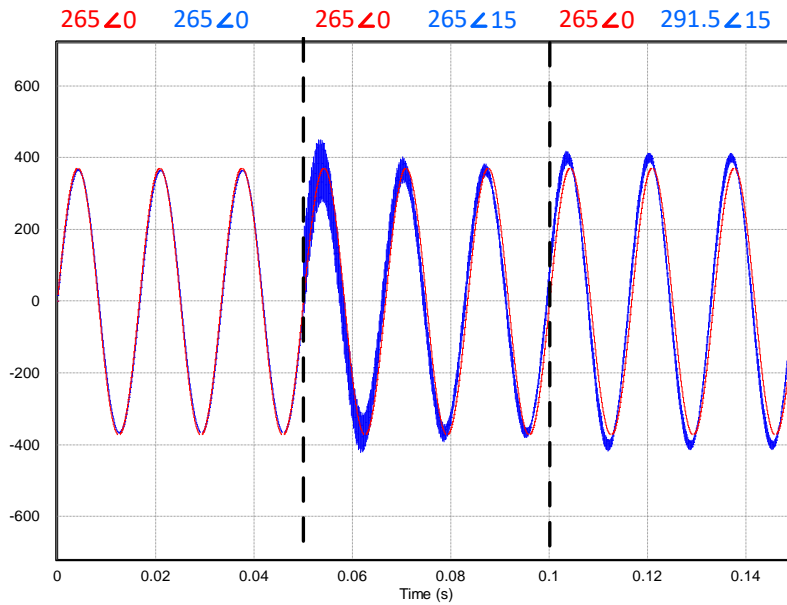


Fig. 21. The phase angle is changed from 0 to 15 at $t_1 = 50$ ms, and magnitude from 1 p.u. to 1.1 p.u. at $t_2 = 100$ ms.

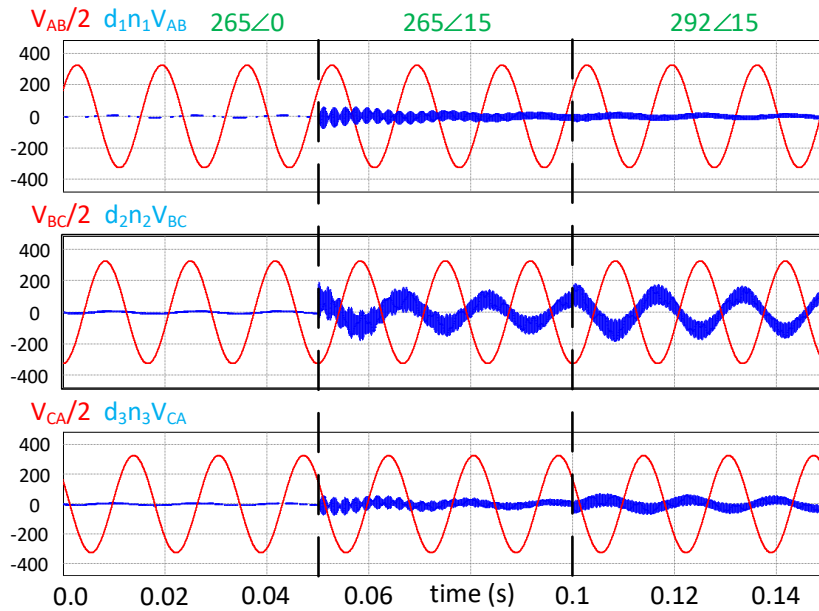


Fig. 22. Fractions of line to line voltages needed to achieve the output voltage changes.

Conclusions and future work

This chapter introduced a new power router topology that enables power flow control between microgrids without the use of a dc-link. The proposed PR was designed by augmenting a fractionally rated transformer with AC-AC converter blocks (also fractionally rated). The proposed topology was named as Power Electronics Transformer with Dynamic Voltage and Angle Droop Control (PET-DVADC). Design details of the PET-DVADC concept were discussed and analyzed.

A design example was used to obtain simulation results for a desired voltage needed from the proposed topology.

CHAPTER III

PET-DVADC ENABLED ANGLE DROOP CONTROL FOR MICROGRID POWER FLOW CONTROL*

In this chapter, a modified Angle Droop Control (ADC) scheme is presented with added flexibility for accurate peer-to-peer Transactive Energy (TE) control in an interconnected microgrid system. The proposed scheme enables TE (i.e. energy transfer on demand) between two or more microgrids with simultaneous guaranteed stable operation due to overlaid ADC. To enable such a scheme, a power router (PR) for power flow control was introduced in chapter 2, named PET-DVADC. The interface of the proposed topology resides at distribution voltage level of the micro-grid interface point before the step-up transformer. Simulations on a five interconnected microgrid architecture are presented. Energy transactions between two and three microgrid examples are discussed with the proposed PET-DVADC control.

Introduction

The need for accurate microgrid power flow control has received increased attention in the literature, specially the topic of Transactive Energy (TE) [32-36]. In view of this, the Grid-Wise Architecture Council initiated a discussion in the area of TE systems, to facilitate the integration of “prosumers”, utility companies and researchers to obtain common definitions and standards in this area [33, 34]. Peer to Peer markets in TE

* © 2018 IEEE. Reprinted, with permission from [10] Jorge A. Ramos-Ruiz, Prasad Enjeti, Le Xie, “Peer-to-peer Energy Transaction in Microgrids with Power Electronics Enabled Angle Droop Control” in IEEE Electronic Power Grid (eGRID), November 2018, pp. 1-6.

frameworks have been extensively studied [35, 36]. To enable any TE approach, the importance of precise power flow control strategies becomes evident, as it can have a high impact on the system's stability [37].

As previously mentioned, angle droop control uses the phase angle (δ) to control the flow of real power, and the voltage magnitude (V) to control the flow of reactive power, as shown in equations (1.3) and (1.4).

In [38], a modified angle droop control technique is introduced to improve the accuracy of the proportional power sharing by communicating each PCC with its neighbors, without affecting the stability of the network. This chapter proposes a modified angle droop control method approach, to enhance the flexibility of the system, by providing each microgrid with the freedom to not only share power in a proportional way. This will allow each microgrid to decide if more energy is to be sent (or received) to/from the rest of the grid.

Different methods have been studied for power flow coordination, traditionally, power flow has been achieved by setting the operating modes of generators, shunt VAR compensation and Load Tap-Changing methods, but the range of control is limited [19]. In [27], the controllable network transformer (CNT) is introduced, it consists of a fractionally rated transformer augmented by an AC-AC converter. It is a low-cost option, but is optimized for only magnitude control, having real power flow control limited capabilities.

In [28], a Power Router (PR) technology optimized for real power flow coordination is presented, it is called the compact dynamic phase angle regulator (CD-

PAR). Similar to the CNT, it uses fractionally rated transformers to obtain the desired voltage realization, it assumes that the needed phase angle δ is small, and does not have full control over the voltage magnitude, compromising reactive power flow accuracy.

In this chapter, a modified Angle Droop Control scheme is discussed as a possible approach to implementing the peer-to-peer energy transaction. The new scheme provides the DSO with an additional degree of freedom, enabling peer-to-peer energy transactions. An example system using five microgrids with high renewable energy penetration is used to prove the validity of the proposed approach, as shown in Fig. 23.

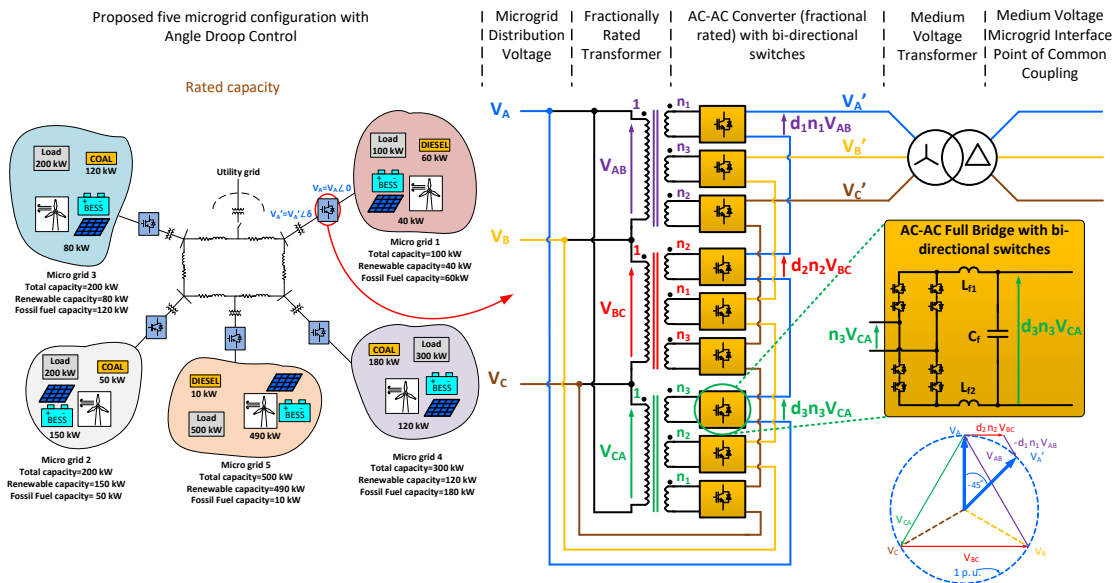


Fig. 23. Proposed Transactive Energy (TE) scheme for interconnected microgrids using Angle Droop Control. Note: each microgrid is connected to the system at the point of common coupling (PCC) through a Power Router (PR). In this example, the PET-DVADC topology (discussed in detail in chapter 3) is shown to enable dynamic adjustments to PCC voltage magnitude and phase angle.

Conventional Angle Droop Control

Conventional Angle Droop Control achieves power sharing between microgrids by using P- δ control (for real power sharing) and Q-V droop control (for reactive power sharing) [2, 11]. The voltage angle and magnitude droop control law is shown in equations (1.3) and (1.4).

Modified Angle Droop Control for peer-to-peer energy transaction

In this section, changes to conventional angle droop control are discussed. The proposed modifications to conventional Angle Droop Control scheme to enable Transactive Energy control are shown in Fig 24. When a TE operation is required by the DSO, the required power to be supplied by a particular microgrid is given to the controller as $P_{i, \text{desired}}$. This required power is then compared to the power being supplied by the microgrid, and the difference is then handled by a PI controller. The output of the PI controllers (Fig. 24) results is the needed change for the PCC's voltage magnitude V_i and phase angle δ_i . Both V_i and phase angle δ_i are controlled by adjusting the duty cycle of AC to AC converter blocks in PET-DVADC (see chapter 2 for additional details).

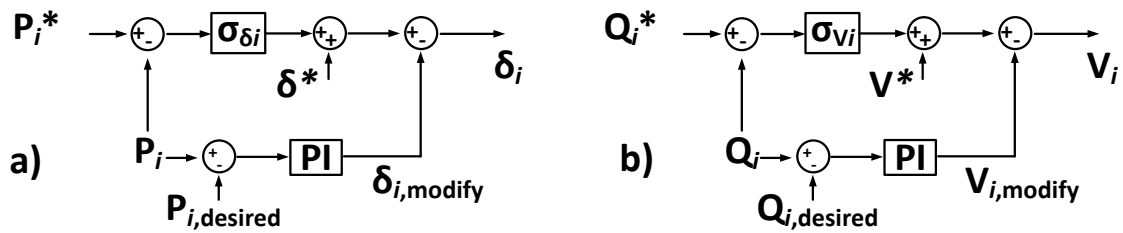


Fig. 24. Modified Angle Droop Control scheme. a) Phase angle droop controller. b) Voltage magnitude droop controller.

It can be seen from Fig. 24a that if a microgrid requires additional real power from the rest of the system, the difference $P_i - P_{i,desired}$ will be positive, resulting in a reduction of its PCC phase angle. This will enable the desired power transfer. Similarly, Fig. 24b shows the needed adjustments for the differences in reactive power.

Design examples and simulation results

Fig. 25 shows example interconnections between five microgrids. Each microgrid depicted in Fig. 25 is assumed to have different renewable energy penetration and load profile. As described previously, each microgrid is interfaced to the other via a power router PET-DVADC. In this section, two different scenarios of the example system are simulated in PSIM for the power ratings shown in Fig. 25 and table 2. The main purpose is to show how the modified angle droop control is able to accurately control the power generated per microgrid as required.

Transactive Energy Scenario # 1

In the first scenario (see Figs. 25, 26 and 27), the loads of all microgrids are increased from 20% to 85% at $t = 0.1$ seconds using conventional Angle Droop Control.

At this time, since the renewable energy sources availability is not optimal, the microgrids need to rely on fossil fuels to meet their total demands. At $t = 0.2$ seconds, the loads remain the same, however it is assumed that there is an increase in the renewable energy availability in μG_5 (55 kW). This additional availability of 55 kW can now be transacted by the DSO to μG_1 and μG_2 to reduce the usage of fossil fuel resources in their systems. This scenario is graphically shown in Fig. 25, where μG_5 delivers to μG_1 (25 kW) and μG_2 (30 kW). In order to accomplish this transactive energy flow, the modified angle droop controller, as shown in Fig. 27, reduces the phase angles δ_1 and δ_2 , and increases δ_5 , enabling the required action by the PET-DVADC.

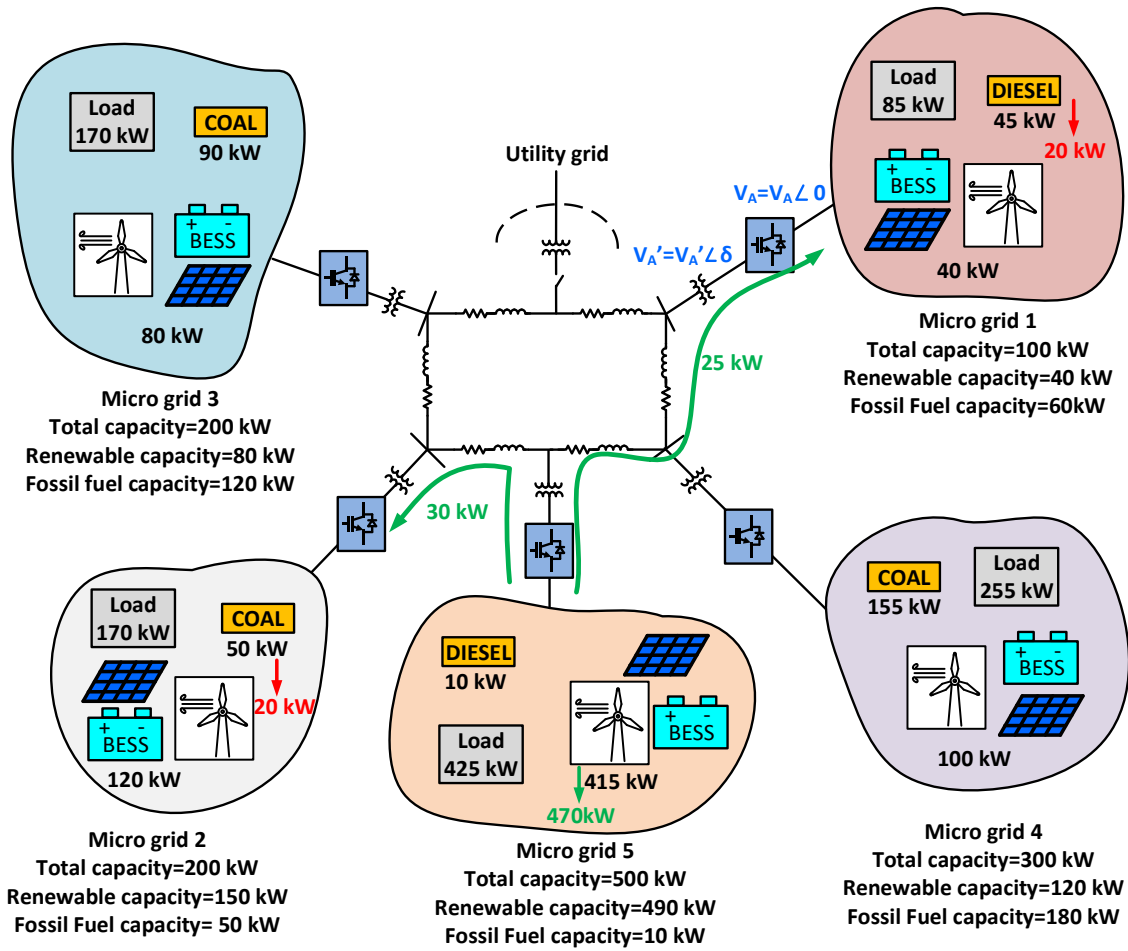


Fig. 25. Simulation scenario 1 for Transactive Energy application. After 0.2 seconds, the availability from renewable sources in μ G5 increases by 55 kW, and the DSO distributes the power to μ G1 (25 kW) and μ G2 (30kW), so they can reduce their fossil fuel needs.

Fig. 26 shows the accurate power flow control. After $t = 0.1$ seconds, the load is increased in all microgrids, it can be seen that thanks to the conventional angle droop control, the power is shared appropriately by all the microgrids. After $t = 0.2$ seconds, μ G5 is required to supply 25 kW, 12.1 kVAR to μ G1 and 30 kW, 14.5 kVAR to μ G2. By using the proposed control, it can be seen that the power is accurately controlled.

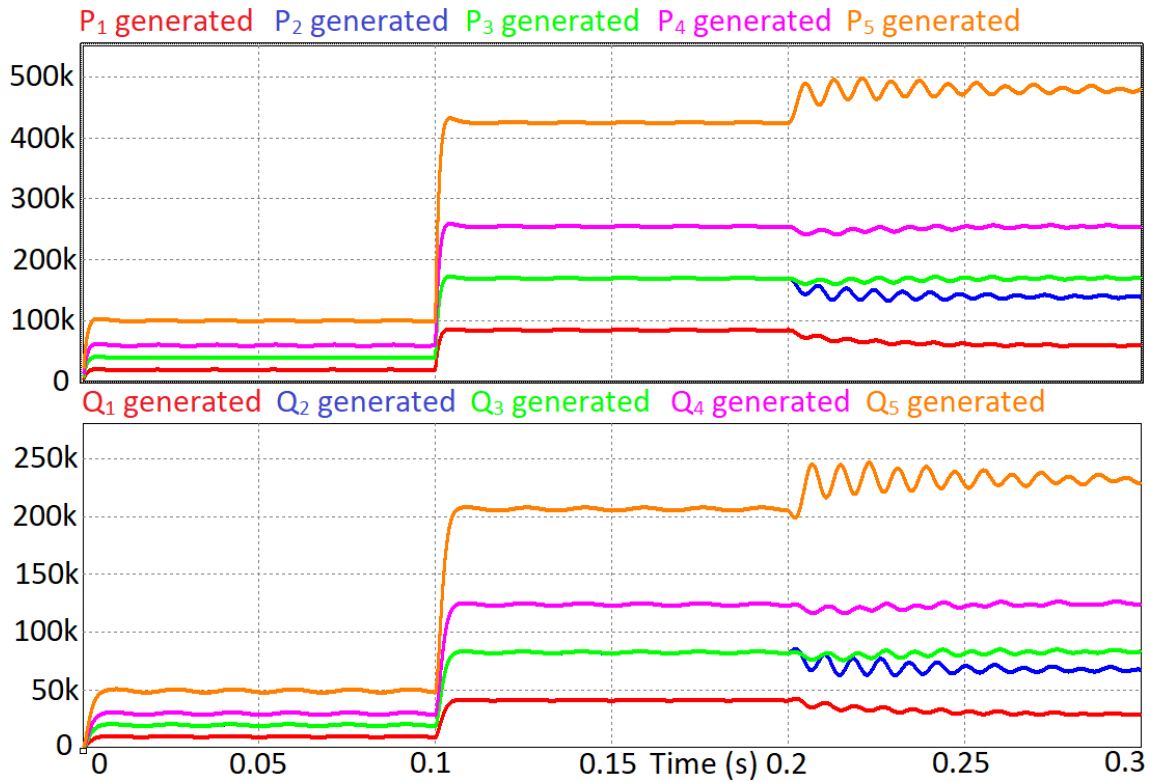


Fig. 26. Simulation results for the proposed scenario, after $t = 0.1$ seconds, the system load changes from 25% to 85%, after $t = 0.2$ seconds, μG_5 provides 25kW, 12.1 kVAR to μG_1 and 30 kW, 14.5 kVAR to μG_2 .

Fig. 27 shows the voltage magnitudes and phase angles that the PET-DVADC topology needs to realize to allow the power flow control, as required by the DSO. As can be seen, since 25 kW are required by the μG_1 to reduce its fossil fuel consumption, the total power it will produce is only 60 kW instead of the previous 85 kW, this difference is handled by the PI controller, resulting in a reduction of the phase angle δ_1 allowing the μG_1 to receive power from the μG_5 . Since it also requires reactive power, the voltage magnitude at the PCC will also reduce in a similar fashion.

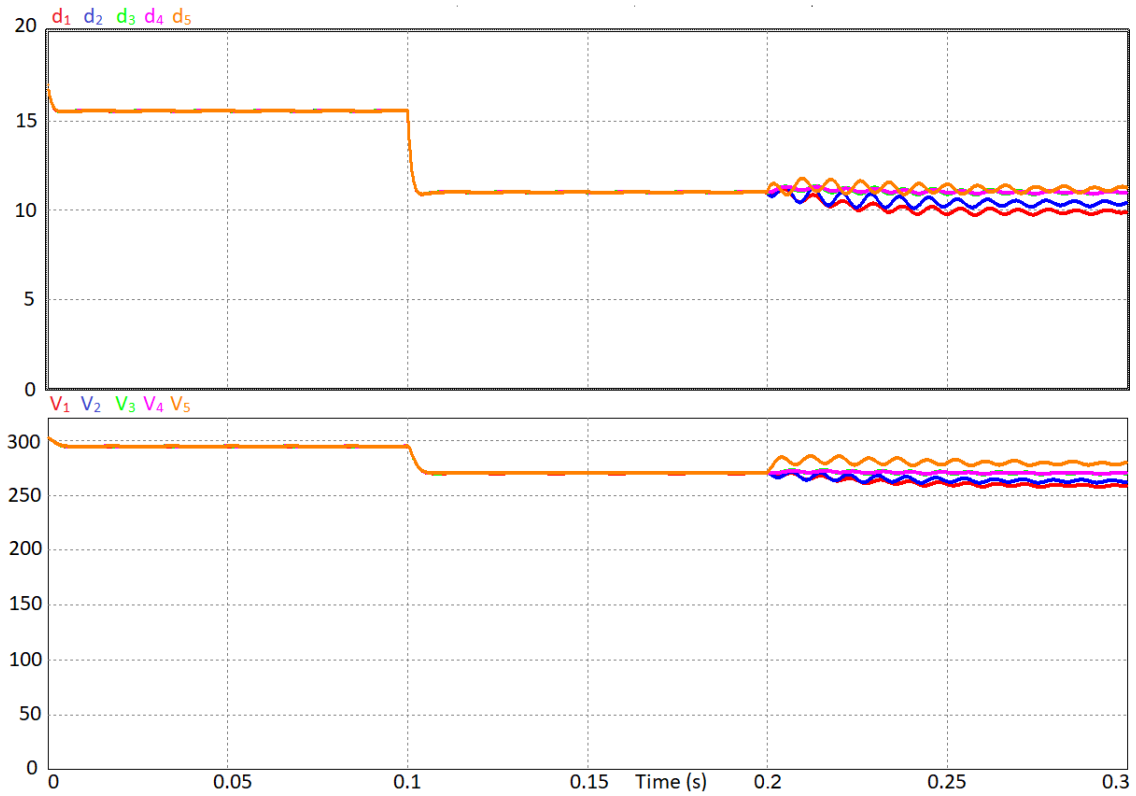
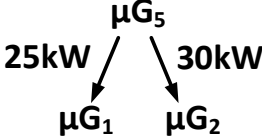


Fig. 27. Simulation results for the proposed scenario, after $t = 0.2$ seconds, $\delta_1=9.95$, $\delta_2=10.4$ and $\delta_5=11.2$, while the other phase angles are set at $\delta_i=11.04$, enabling real power flow control. To control the reactive power, $V_1 = 260$, $V_2 = 264$, $V_5 = 280$, while the other magnitudes are set at $V_i = 271$ V.

Table 2 summarizes the steps taken in the example system scenario.

Table 2. Steps taken to show the system response when a TE operation is performed by the system between μG_1 , μG_2 and μG_5 .

all μG_s Load 20%	no TE each μG supplies its own load	t=0.1 sec
all μG_s Load 85%	no TE each μG supplies its own load	
all μG_s Load 85%		t=0.2 sec

Transactive Energy Scenario # 2

In the second scenario (see Figs. 28, 29 and 30), the loads of all microgrids are also increased from 20% to 85% at $t = 0.1$ seconds. At $t = 0.2$ seconds, the DSO makes the decision to completely eliminate fossil fuels consumption for μG_2 , while the loads remain the same. Since there is a surplus in the renewable energy availability in μG_5 (50 kW). This additional availability of 50 kW can now be transacted by the DSO to μG_2 to eliminate its usage of fossil fuel resources. This scenario is graphically shown in Fig. 28 where μG_5 delivers 50 kW to μG_2 . In order to accomplish this transactive energy flow, the modified angle droop controller, as shown in Fig. 30, reduces the phase angle δ_2 , and increases δ_5 , enabling the required action by the PET-DVADC.

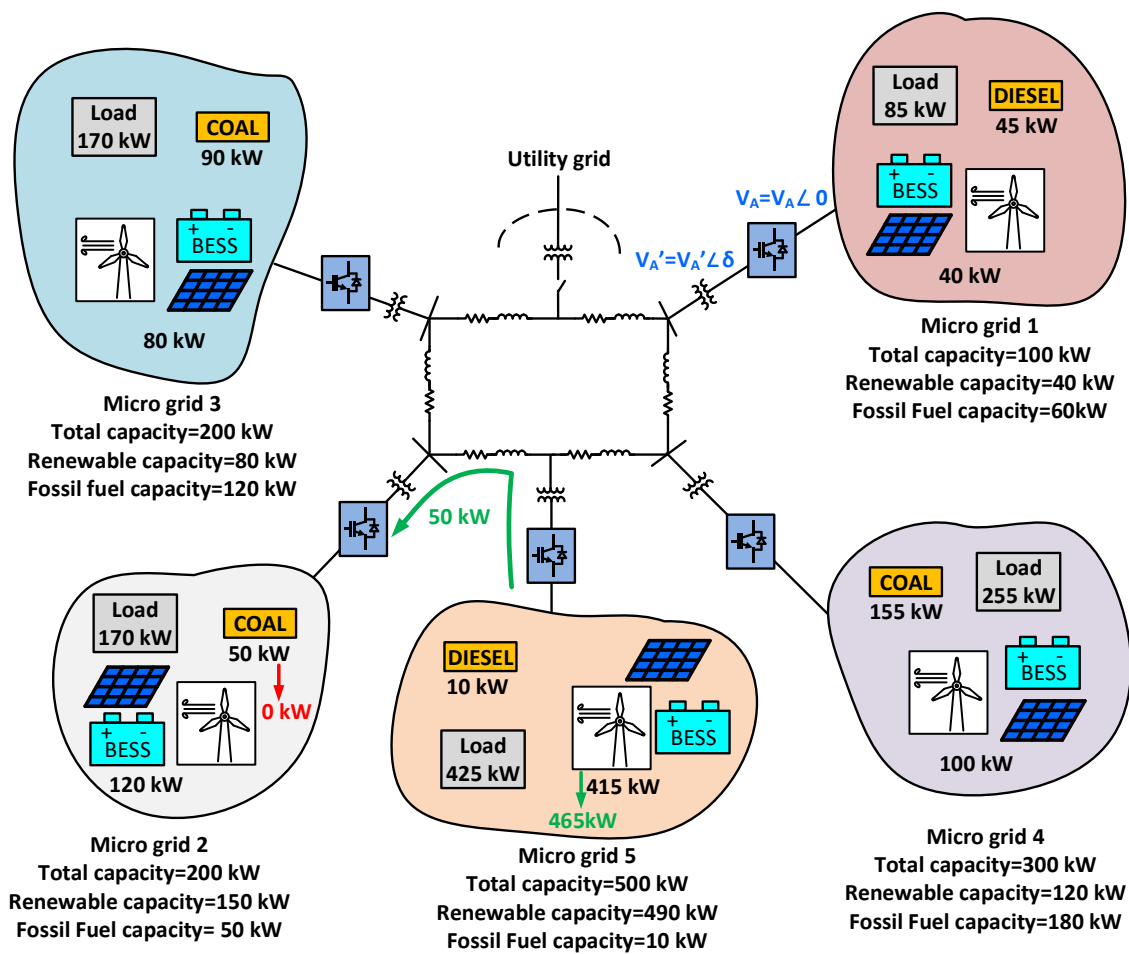


Fig. 28. Simulation scenario 2 for Transactive Energy application. After 0.2 seconds, the availability from renewable sources in μG_5 increases by 50 kW, this can be used to completely eliminate the needs for fossil fuel sources that μG_2 needs.

Fig. 29 shows the accurate power flow control. After $t = 0.1$ seconds, the load is increased in all microgrids, it can be seen that thanks to the conventional angle droop control, the power is shared appropriately by all the microgrids. After $t = 0.2$ seconds, μG_5 is required to supply 50 kW, 29.3 kVAR to μG_2 . By using the proposed control, it can be seen that the power is accurately controlled.

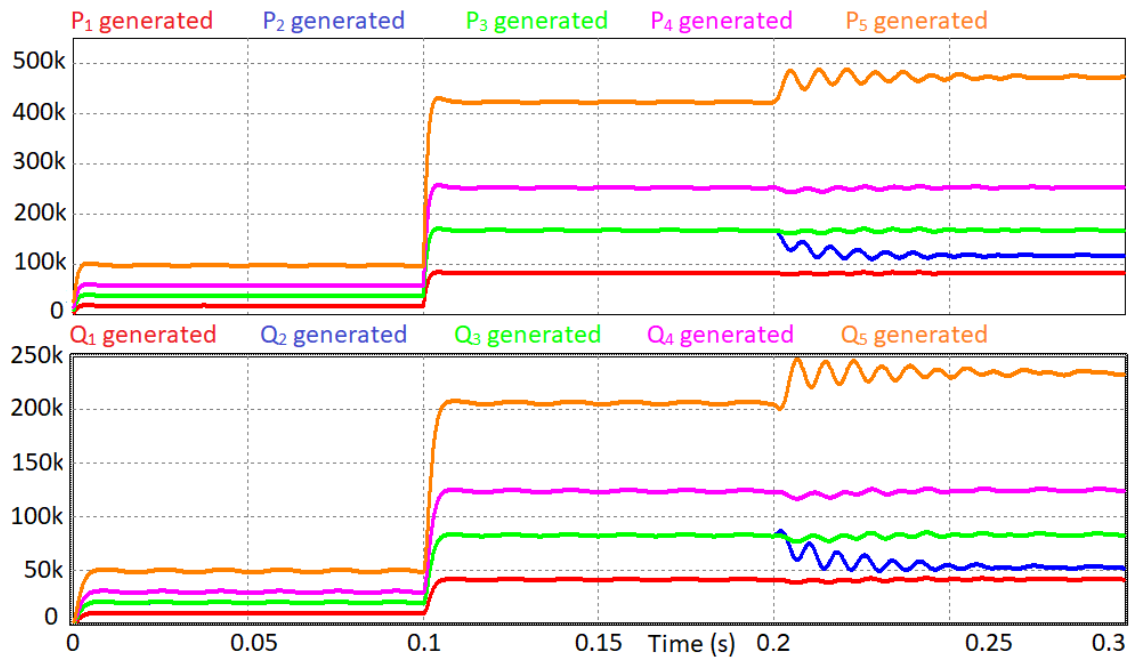


Fig. 29. Simulation results for the proposed scenario, after $t = 0.2$ seconds, $\delta_2 = 10.1$ and $\delta_5 = 11.07$, while the other phase angles are set at $\delta_i = 11.02$, enabling real power flow control. To control the reactive power, $V_2 = 258$, $V_5 = 279$, while the other magnitudes are set at $V_i = 271$ V.

Fig. 30 shows the voltage magnitudes and phase angles that the PET-DVADC topology needs to realize to allow the power flow control, as required by the DSO.

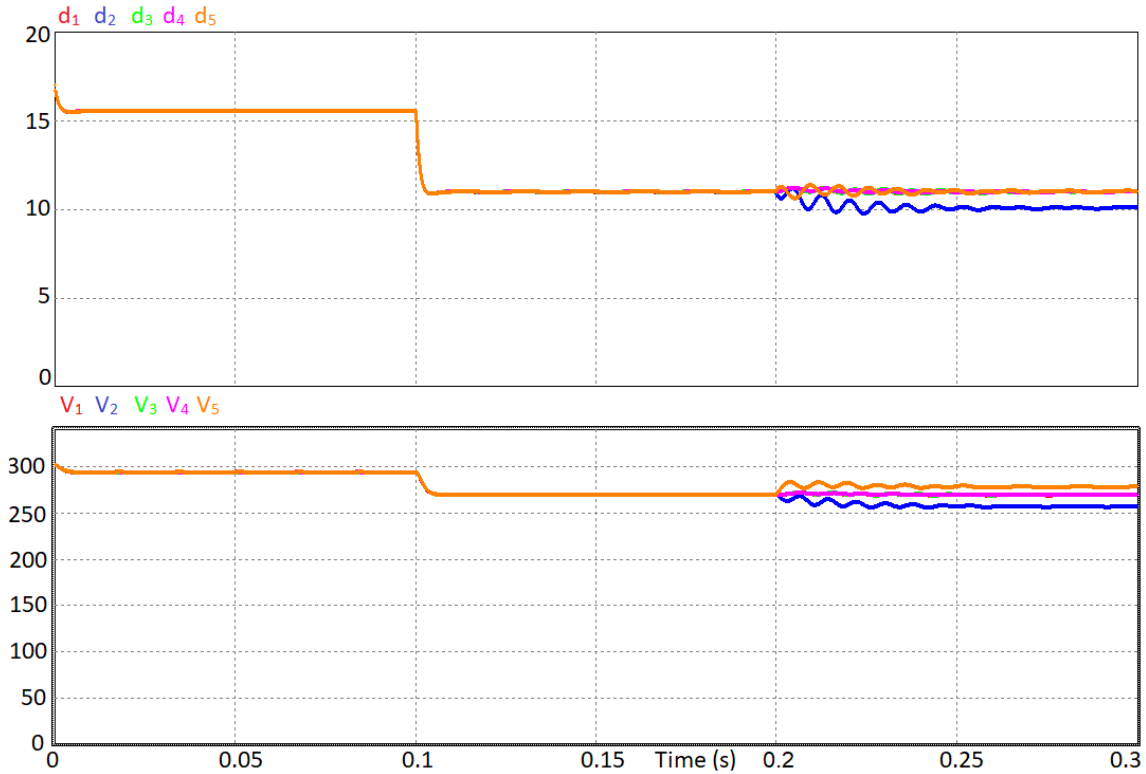


Fig. 30. Simulation results for the proposed scenario, after $t = 0.2$ seconds, $\delta_2 = 10.1$ and $\delta_5 = 11.07$, while the other phase angles are set at $\delta_i = 11.02$, enabling real power flow control. To control the reactive power, $V_2 = 258$, $V_5 = 279$, while the other magnitudes are set at $V_i = 271$ V.

Conclusions and future work

This chapter discussed the implementation of a modified Angle Droop Control (ADC) scheme that is proposed as a means to achieve peer-to-peer energy transaction in future microgrid interconnections. The proposed strategy is intended to work with the topology presented in chapter 2 (PET-DVADC). Two example scenarios have been simulated extensively and results are discussed.

CHAPTER IV

POWER ELECTRONICS INTELLIGENCE AT THE NETWORK EDGE (PINE) – A NEW TOPOLOGY TO INTERFACE PV AND BATTERY ENERGY STORAGE SYSTEMS AT THE GRID EDGE**

In this chapter, a self-organizing power electronic converter with control intelligence at the edge of the network is proposed and discussed. The proposed converter is called Power Electronics Intelligence at the Network Edge (PINE). The proposed approach consists of a power electronic converter (rectifier/dc-link/inverter) used to supply residential loads. The rooftop solar and battery energy storage system is connected to the dc-link. With the bidirectional characteristic of the PINE, the load voltage is regulated via feedback, while input distribution voltage can be allowed to vary in a range. This type of configuration allows for control of input power factor to be unity, reactive power to be injected at the grid edge to regulate the voltage and also enable energy budgeting, i.e. limit the amount of power to the residential load under disaster situations [39]. This concept provides a possible pathway toward supporting a very high level of PV penetration in present and future distribution systems. Simulation and experimental results on a laboratory prototype system validate the PINE converter concept.

** © 2018 IEEE. Reprinted, with permission, from [39] Jorge A. Ramos-Ruiz, Prasad Enjeti, Le Xie, “Power Electronics Intelligence at the Grid Edge – Enables Energy Budgeting” in IEEE Electronic Power Grid (eGRID), November 2018, pp. 1-6.

Introduction

Recently, there has been an effort by governments and utilities around the world to derive a significant amount of energy from renewable sources, increasing renewable electricity capacity to unprecedented levels; this growth is expected to continue in the near future, or even accelerate [40]. If such systems are adopted with high penetration of PVs varying their output, inter temporally in an unpredicted manner, maintaining a good voltage profile becomes challenging due to the low spatial and temporal resolution of voltage control devices [41]. Actually, the challenges to maintain a good voltage profile limits how much PV can be connected to distribution systems [42].

In traditional residential PV/BESS systems, the house/load is directly connected to the grid and the residential load is susceptible to grid voltage variations. Further, since the power supplied from the grid is not processed, it is not possible to limit the amount of power delivered to each consumer in case of limited availability.

The topic of electric distribution system optimization and restoration has attracted increased attention thanks to the smart grid investments across the world. Examples of distribution system optimization and volt var regulation efforts are shown in [43, 44]. Further, [45, 46] explore the possibility of using microgrids as a way to improve power supply resilience during natural disasters. This is done by adding diversity to the energy source, reducing the dependency on certain essential infrastructures to operate a system (or lifelines). Theoretical calculations confirmed via Monte Carlo simulations are employed to show the availability and higher availability in the presence of renewable

energy sources is confirmed. They do not however, show disaster reconfiguration architecture and energy budgeting aspects that are essential under post-disaster scenarios.

Assessments post-2005 bombings in London conclude that cell phone networks are not resilient, however, the Internet designed as a network with its intelligence at the edge is highly resilient [47]. Such resiliency is needed for power distribution too since electricity is the very lifeblood of modern civil society, just as much as communication is. There is urgent need to restore the critical needs, if not all the needs, of access to electricity.

Traditionally, residential rooftop solar PV/Battery systems are installed employing dedicated converters for each [16]. The main advantages are: a) energy cost reduction, b) peak shaving, c) volt var control, d) consumption in rural areas. Fig. 31 shows such a system where in the roof-top PV and the battery energy storage system (BESS) employ separate DC-AC converters interfaced to the grid.

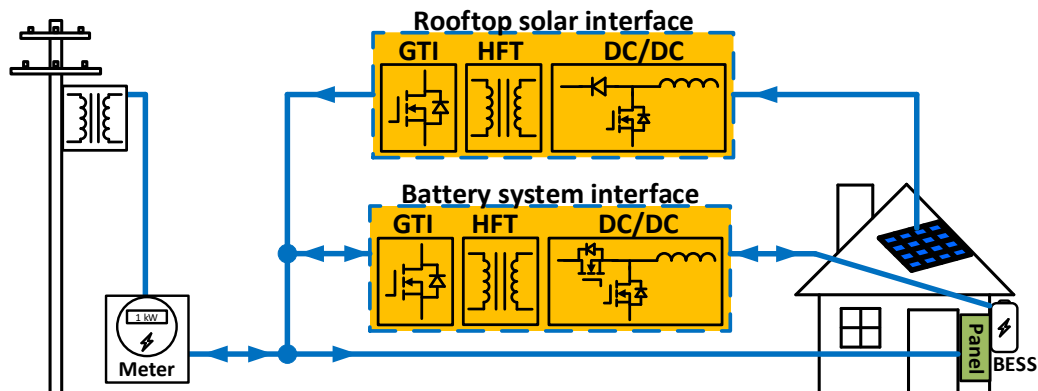


Fig. 31. Conventional rooftop PV and battery energy storage system (BESS) interfaced to the grid via separate topologies.

It is noted that the house/load is directly connected to the grid and the residential load is susceptible to grid voltage variations. Further, since the power supplied from the grid is not processed, it is not possible to limit the amount of power delivered to each consumer in case of limited availability.

In view of this, this chapter focuses on self-organizing power electronics intelligence at the very edge of the electric distribution network. The resultant paradigm of grid operation is termed power electronics intelligence at the network edge (PINE) as shown in Fig. 32, first introduced in [48]. The proposed converter is deployed at the very edge of the network, i.e., behind the electric meter, enabling the utility company to perform energy budgeting during disaster events, while keeping the end-users' voltage constant, and reducing input current harmonics during normal operation. PINE can also be controlled to inject reactive power to the grid for volt var control (VVC).

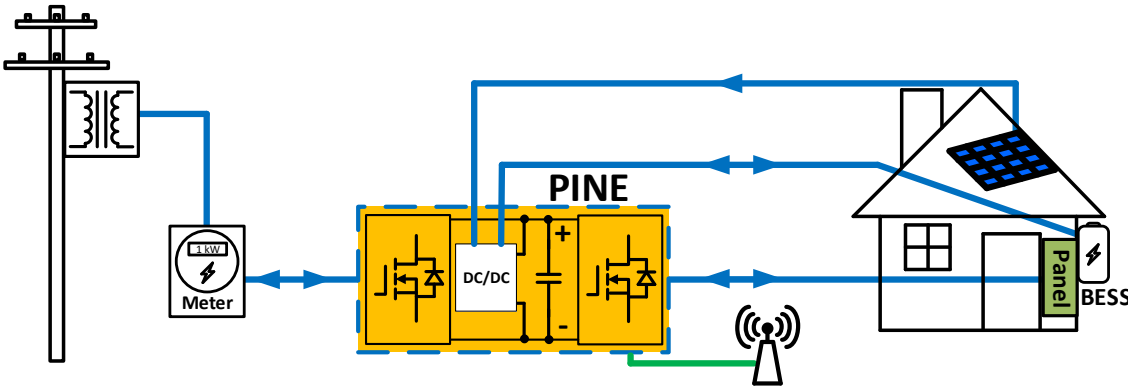


Fig. 32. Proposed power electronics at the grid edge - a self-organizing converter with control intelligence at the edge of the electric distribution network.

The main advantages of the proposed power electronics at the grid edge concept are:

- Since PINE is deployed in front of each residential load, input utility voltage can vary over a wider range since PINE allows for output voltage to be regulated regardless of input voltage variations.
- The Front End PWM converter can be controlled to exhibit close to unity input factor with sinusoidal input current shape. This reduces the overall rms value of the currents flowing in the distribution system, minimizing losses.
- Since the power consumed by the residential load is entirely processed via the PINE converter, the output load current can be limited during disasters based on the available power. Hence energy budgeting can be implemented with the proposed topology. This feature can be enabled remotely using Internet-of-Things (IoT) technology.
- Since the power consumed by the residential load is entirely processed via the PINE converter, the output load current can be limited during disasters based on the available power. Hence energy budgeting can be implemented with PINE.
- The overall cost of the PINE converter is comparable with a separate PV inverter and BESS converter. Since the average cost of a PV inverter (in residential applications) represents 10% of the overall cost. Assuming a residential setup already has a PV inverter installed, the extra cost in hardware can be estimated to be similar to getting an extra PV inverter.
- Output voltage (120/240 V, 60 Hz) is regulated via PWM control of the output converter.

- PINE is based on distributed decision-making without any need for coordination.
- Power flow is bidirectional.
- The proposed PINE topology enables the use of power disaggregation, or non-invasive load monitoring (NILM) [49], and Voltage Conservation Reduction (VCR) [50], both strategies allow the customer to reduce energy consumption.

Fig. 31 shows an example system where in the roof-top PV and the battery energy storage system (BESS) employ separate converters interfaced to the grid, each of them with its own DC/DC, isolation and DC/AC stages [15, 16]. Comparing Fig. 31 with the proposed PINE architecture in Fig. 32, it is noted that the proposed PINE integrates both PV and BESS interface with the utility in a single converter architecture. Figs. 33 and 34 show one possible circuit topology of the PINE architecture depicting that total number of device components are not exceeded compared to Fig. 31. Comparing the size of PV installations on each home and BESS ratings, the PINE architecture VA ratings is comparable and without any additional cost penalty.

Proposed PINE topology

The proposed PINE concept, as shown in Figs. 33 and 34, is designed to power the 120/240V split phase loads in a typical home and consists of three main stages. The first stage consists of a front end PWM converter that minimizes current harmonics from the grid, and maintains the dc-link voltage magnitude constant when the PV/Battery system is not being used. The middle stage is a rooftop solar system that consists of a PV module and a BESS interfaced through a power sharing converter to the voltage V_{EF} , this is then interfaced to the dc-link through a bidirectional high frequency series resonant DC-DC

converter. The final stage consists on an output PWM converter that feeds a split phase ac output (120/240V, 60 Hz). Since the power from the grid is handled entirely by the proposed topology, energy budgeting is available during disaster events, and during normal operation, the circuit is able to operate over a wide range of input voltage (from 0.8 pu to 1.2 pu), while minimizing harmonic input current. In addition, this circuit allows bidirectional power flow and control of real and reactive power flow.

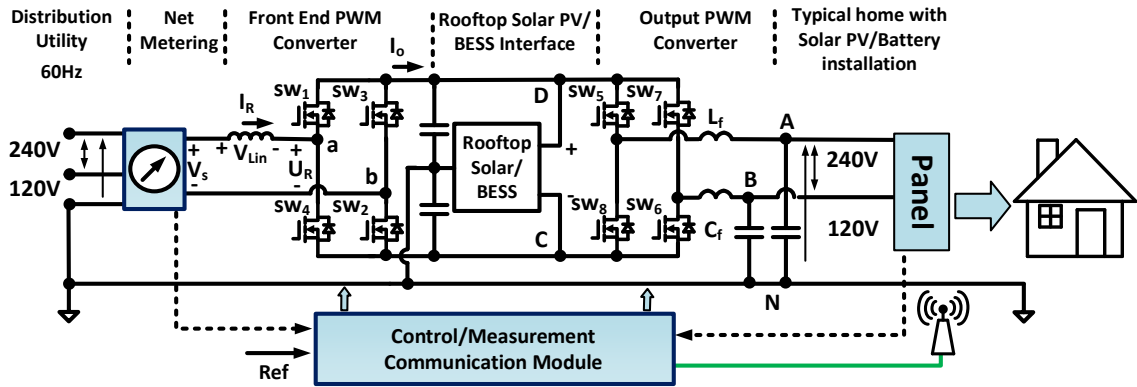


Fig. 33. Proposed topology for the Power Electronics intelligence at the Network Edge (PINE) concept. Both roof-top solar PV and BESS are integrated into the dc-link.

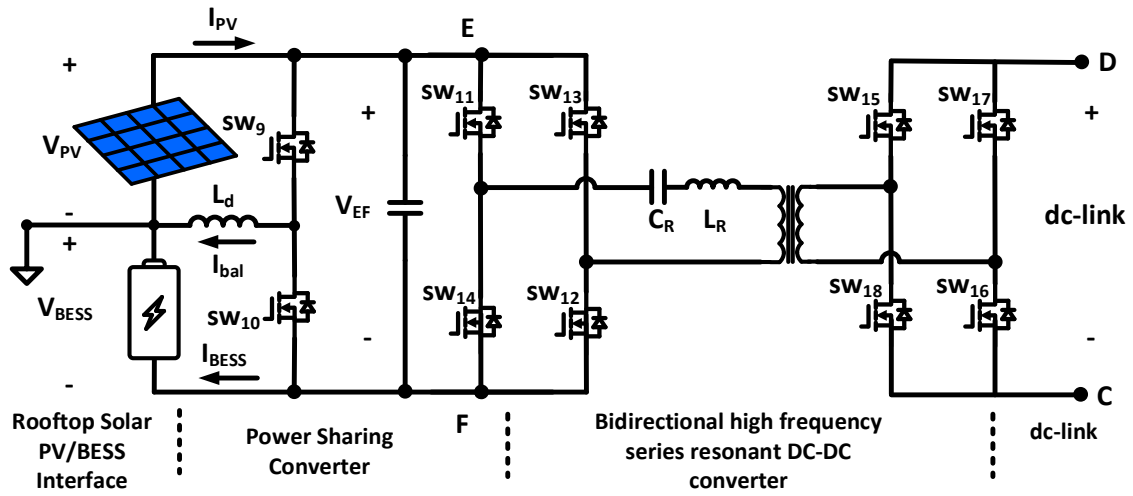


Fig. 34. Detailed circuit Rooftop PV/BESS Interface.

PV system design

For the PV system design, a 290 W module is selected. The main electrical characteristics are shown in Table 3:

Table 3. Electrical data of PV module selected for the PINE system.

Peak power (P_{max})	290 W
Max power voltage (V_{mp})	54.7 V
Max power current (I_{mp})	5.59 A
Open circuit voltage (V_{OC})	64.2 V
Short circuit current (I_{SC})	6.0 A
Cells in series	96

Fig. 35a shows the Power vs Voltage curve of the PV panel module used for the proposed PINE system. Fig. 35b shows the selected module current vs Voltage (IV) curve.

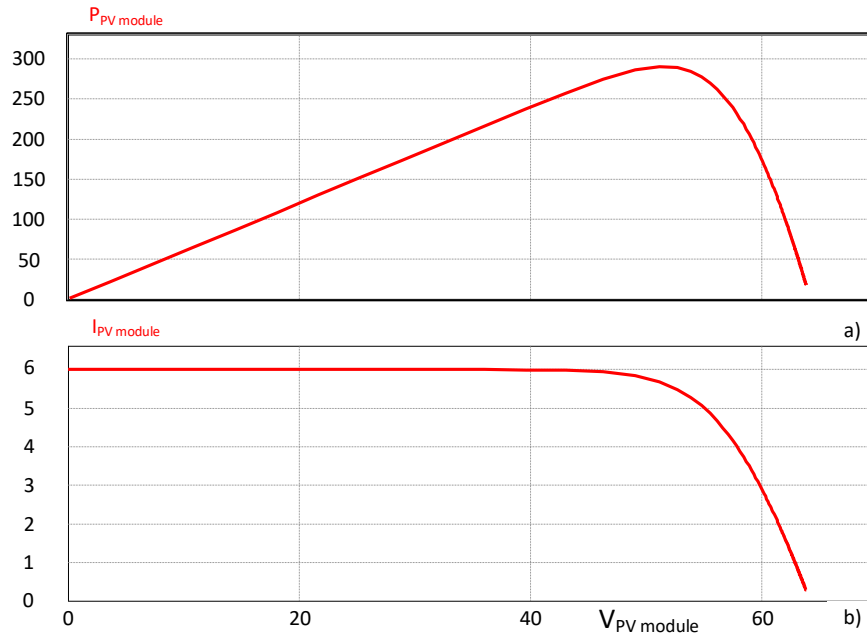


Fig. 35. a) PV curve of the module selected for PINE system. b) IV curve of the selected module.

As previously mentioned, the PV system is designed to provide a maximum of nearly 5 kW of power at its peak capacity. To provide such needs, a total of 17 panels are needed in parallel, for a total power of 4.93 kW at full capacity. Fig 36 shows the PV and IV curves of the PV array.

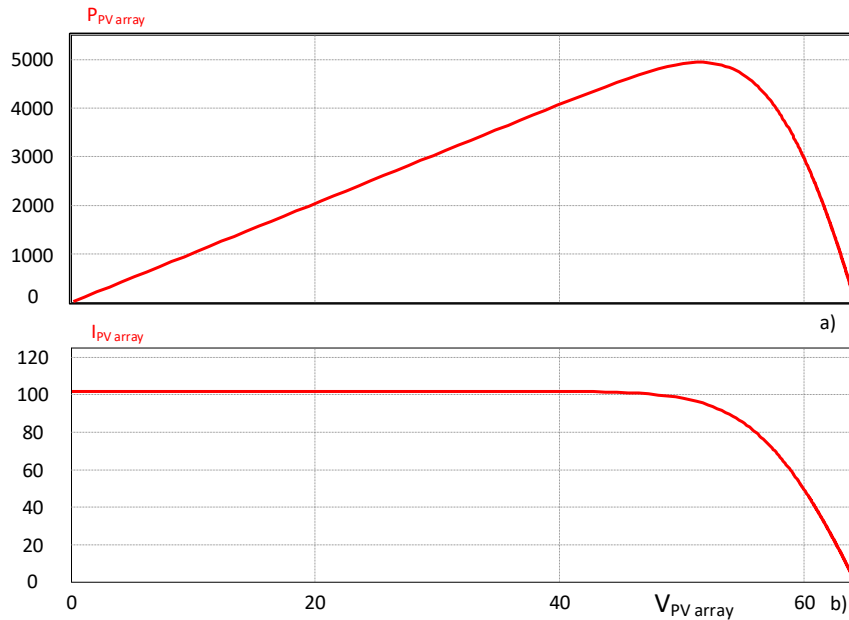


Fig. 36. a) PV curve of the PV array designed for PINE system. b) IV curve of the selected array.

Front end PWM converter

The Front End converter (Fig. 33) consists of switches SW_1 to SW_4 , it is operated at high switching frequency and is synchronized with the grid. The PWM control ensures near sinusoidal input current and unity input power factor. This contributes to reduce the distribution system's line losses, size of components, system component overheating, etc. When there is no available power from the PV/BESS system, this converter maintains the dc-link voltage magnitude constant. When there is available power in the PV/BESS system, the Front End converter is controlled to return power to the grid, acting as a smart inverter. Further, the Front End converter power factor can be adjusted to inject reactive

power at the grid edge for voltage control purposes. The control strategy is detailed in the following section.

Output PWM converter

The output PWM converter generates split phase ac output (120/240V, 60Hz) designed for the typical residential load. The control is able to maintain a sinusoidal output voltage under a variety of load conditions. During disaster events, the output maximum allowable power for each house is controlled by limiting the reference current. This in turn enables energy budgeting, improving power supply availability during grid recovery times. Further, we envision the possibility of remotely turning off loads when needed. The following section details the control strategy.

Rooftop Solar PV/Battery Interface

The rooftop solar and BESS system is connected as shown in series via a power sharing converter. The power sharing converter switches SW_9 and SW_{10} are used to control the amount of power that both the PV and the BESS contribute to feed the load/grid depending on the operating conditions requirements. The following section details the control strategy. When the PV/BESS are supplying power to the load and/or grid, the dc-link voltage magnitude is maintained by the bidirectional high frequency series resonant DC-DC converter. The following section details the control strategy.

Control strategy of the PINE converter

In this section the control strategy for the PINE converter is detailed. As mentioned previously, the control depends on the operating conditions of the system.

Front end PWM converter control

The Front End PWM converter is bidirectional, having two operating modes: rectifier mode when the grid is supplying the PINE interfaced load, and inverter mode when power is fed back to the grid.

When the grid is feeding the PINE interfaced load (rectifier mode), the converter ensures a power factor close to unity, and the input current is harmonic free (due to high frequency PWM switching) with an input current I_R that is in phase with the grid voltage V_S , resulting in a negative phase angle δ between the converter voltage U_R and the grid voltage V_S as shown in Fig. 37 [51].

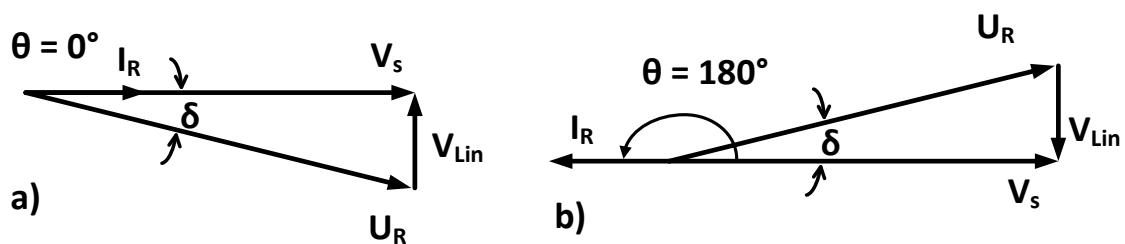


Fig. 37. a) Rectifier mode; b) Regen mode. Adapted from [51].

A current mode controller is set to maintain a constant dc-link voltage. The reference voltage ($V_{dc,ref}$) is compared with the measured dc-link voltage ($V_{dc-link}$), the difference is processed by a PID controller, obtaining the needed reference for the input current d component ($I_{Rd,ref}$). Since no reactive power is desired in this case, the q component of the input current is simply set to 0 ($I_{Rd,ref} = 0$), as shown in Fig. 38.

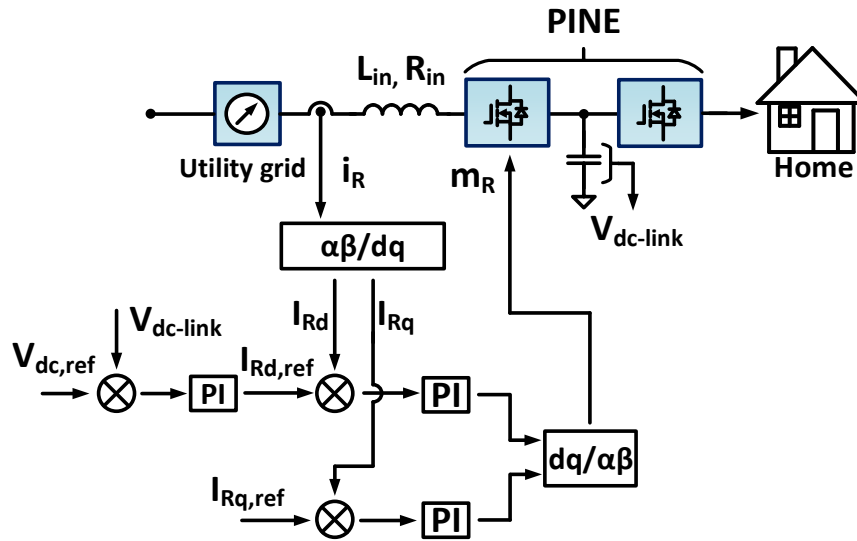


Fig. 38. Current mode controller of Front end PWM converter in rectifier mode.

When there is additional available power in the PV panels and/or the BESS, the front end PWM converter can be operated in inverter mode, resulting in a positive phase angle δ , as shown in Fig. 37b.

The control is similar to the rectifier mode, obtaining the reference for the d and q components of the input current $I_{Rd,ref}$ and $I_{Rq,ref}$, respectively, by using equations 4.1 and 4.2:

$$I_{Rd,ref} = \frac{2*P_{,ref}}{V_{sd}} \quad (4.1)$$

$$I_{Rq,ref} = \frac{2*Q_{,ref}}{V_{sq}} \quad (4.2)$$

Where $P_{,ref}$ and is the required real power (Watts) to be supplied to the grid, and $Q_{,ref}$ is the reactive power (VARs) to be supplied to the grid.

Using the reverse Park transformation (equations 1.14 and 1.15) to process the resulting signals, both control modes result in the modulation index m_R required to control switches SW₁ through SW₄.

Output PWM converter control

The control strategy is shown in Fig. 39. In order to control the output phase voltage V_A , the dq components of a reference value $V_{d,ref}$ and $V_{q,ref}$ are obtained by equations 1.5, 1.6 and 1.7. The measured voltage dq components V_d and V_q are then subtracted from the mentioned reference signals and then processed a PI controller, giving as a result the required references for the output current $I_{d,ref}$ and $I_{q,ref}$. These signals are processed in a similar manner to obtain the required dq components of the resultant signal m_A . Phase voltage V_B is controlled in a similar manner, with a phase shift of 180° [22, 23].

In a disaster situation, the maximum amount of power delivered to a given PINE system can be limited by an external command to adjust the d component of the output current on each phase (I_d) to a maximum allowable when needed, as shown in equation (4.3) and Fig. 39:

$$I_{dref} = \begin{cases} I_{dref}^*, I_{dref}^* \leq I_{max} \\ I_{max}, I_{dref}^* > I_{max} \end{cases} \quad (4.3)$$

Where:

I_{dref}^* is the reference current given by the controller under normal situation (no power limitation), and I_{max} is the current limit for I_d and is calculated by equation (4.4):

$$I_{max} = \frac{2 * P_{limit}}{|V_{d,ref}|} \quad (4.4)$$

Limiting the output current will in turn reduce the output voltage magnitude. To prevent the voltage from reducing below a given limit, we envision the presence of smart home energy management devices with Internet-of-Things (IoT) technology enabled to turn on/off various loads in a typical home. Since 80% of a residential load is fed through dedicated circuit breakers [52, 53], employing solid state circuit breakers loads can be turned on/off remotely by PINE.

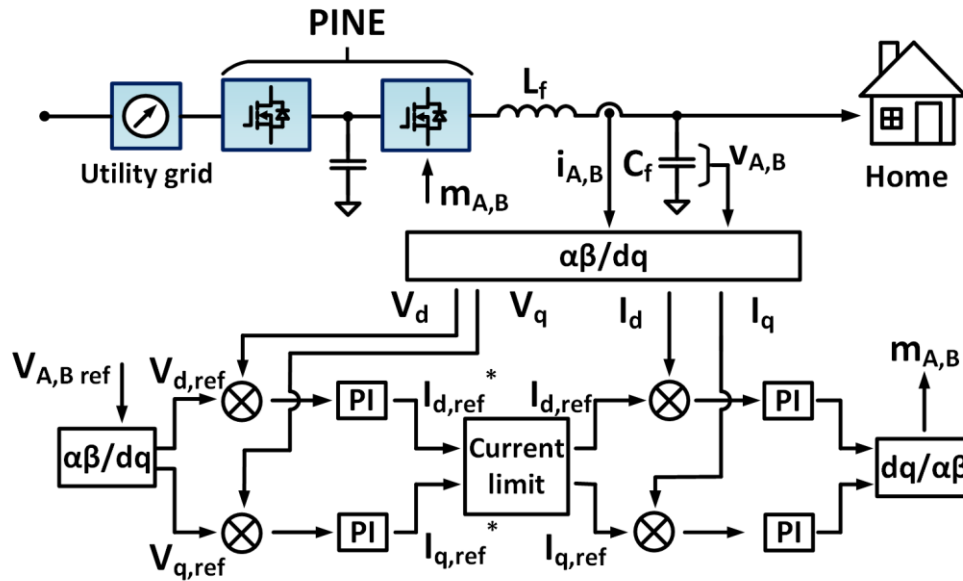


Fig. 39. Output PWM converter control scheme, energy budgeting is enabled by limiting output current. Each phase voltage is controlled in the same manner, with a phase shift of 180° .

In the presence of non-linear loads, the control strategy of the Output PWM converter can be slightly modified, as shown in Fig. 40, a simple inner current regulating loop is used to regulate the output voltage to be nearly sinusoidal even with non-linear currents. The control strategy is shown in Fig. 40. It can be seen that the controller uses the capacitor filter current to correct the output voltage.

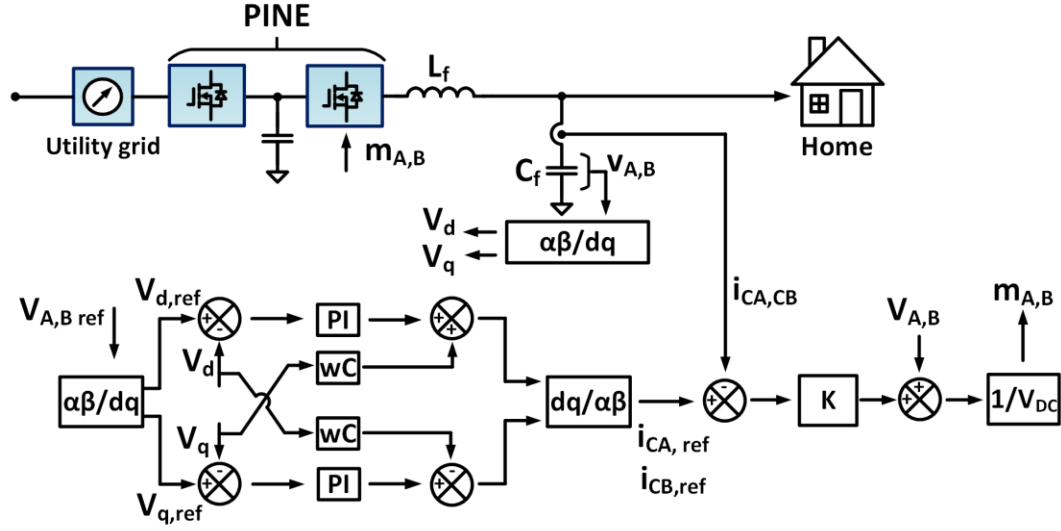


Fig. 40. Control strategy to maintain a nearly sinusoidal output voltage with on-linear loads. Adapted from [54].

Rooftop Solar PV/Battery Interface control

The power sharing converter switches SW_9 and SW_{10} and the balancing current I_{bal} are controlled by the duty cycles D_{sw9} and D_{sw10} . The mentioned duty cycles are obtained from measuring the interfaced voltages V_{PV} and V_{BESS} and using equations (4.5) and (4.6). The resultant average current I_{bal} circulating through the balancing inductor L_{bal} depends on the state of the PSC, as proposed in references [55, 56].

$$D_{sw9} = \frac{V_{BESS}}{V_{BESS} + V_{PV}} = \frac{V_{BESS}}{V_{EF}} \quad (4.5)$$

$$D_{sw9} + D_{sw10} = 1 \quad (4.6)$$

As shown (Fig. 34) a bidirectional high frequency series resonant DC-DC converter is used to interface the output voltage of the PSC V_{EF} with the dc-link. Operating

the DC-DC above the tank resonant frequency (L_R and C_R in series) enables zero voltage switching [57-59]. In order to maintain the dc-link voltage at the required magnitude, two H-bridges are used, the first H-bridge consists of switches SW_{11} - SW_{14} and is connected at the primary side of a high switching frequency transformer. The second H-bridge consists of switches SW_{15} - SW_{18} and is connected at the secondary side of the transformer.

Both H-bridges are controlled by switching signals consisting of high-frequency square waves. The leakage inductance of the high frequency transformer is used as the energy transfer element, The phase shift between the signals controlling the H-bridges is used to maintaining the dc-link voltage at the required magnitude. To control switches SW_{11} and SW_{12} , signal $sig\ 1$ is used, and switches SW_{13} and SW_{14} are controlled by the complementary signal $\overline{sig\ 1}$, as shown in Fig. 41. In a similar manner, $sig\ 2$ is used to control switches SW_{15} and SW_{16} , where SW_{17} and SW_{18} are controlled by the complementary signal $\overline{sig\ 2}$.

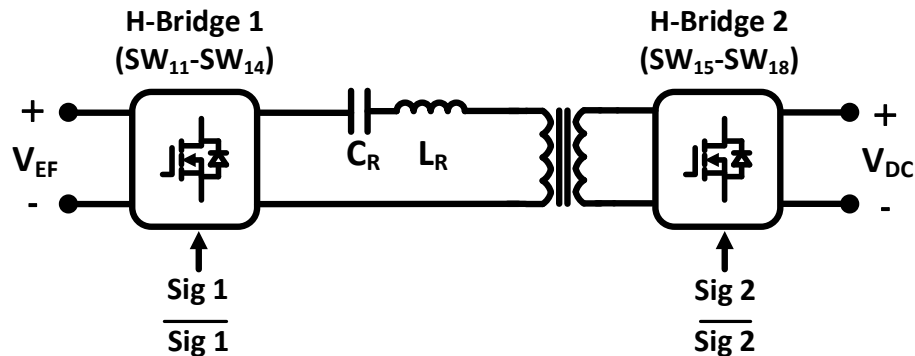


Fig. 41. The voltage V_{DC} is maintained at the desired magnitude by controlling the phase shift between switching functions of H-bridges 1 and 2.

A phase shift ϕ is used between signals *sig 1* and *sig 2*. As shown in Fig. 42. The angle ϕ can be used to control the power transfer, maintaining the voltage magnitude V_{CD} at the required value.

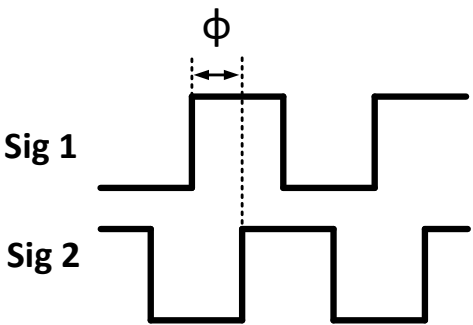


Fig. 42. The voltage V_{DC} is maintained by controlling the phase shift between signals 1 and 2. The phase shift signal is referred to as ϕ .

Simulation results

This section details extensive simulation results of the proposed PINE concept based on the control concepts discussed in previous section over a wide variety of input/output operating conditions.

The simulation design parameters are shown in Table 4:

Table 4. Simulation design parameters of PINE topology.

Parameter	Value
Input voltage	240 V rms
Input inductance	2.3 mH
Switching frequency of Front End PWM rectifier	10 kHz
Balancing inductor	1 mH
Power Sharing Converter switching frequency	15 kHz
Tank resonant frequency of L_R , C_R	1.8 kHz
DC-DC converter switching frequency	2 kHz
dc-link capacitor	3.3 mF
Output voltage	120/240V split-phase
Rated output power	5 kVA (2.5 kVA per phase)
Output inverter switching frequency	21 kHz

A single PINE without the use of the PV/BESS system

Fig. 43, shows the operation of the PINE under varying utility voltage conditions, assuming there is no power available in the PV/BESS system. It is shown that even without any available energy in the PV/BESS system, the PINE topology is able to maintain a constant voltage in the load terminals, regardless of input voltage variations. Fig. 43a

shows the utility input voltage varying $\pm 10\%$ and the corresponding input current, it is noted that when the input voltage increases, the input current decreases to maintain a constant dc-link voltage. The input current is controlled to sinusoidal in phase with the input voltage. Fig. 43b shows the load voltage at the output of the PINE and is shown to be constant, regardless of the variations in the input voltage. Fig. 43c shows the dc-link voltage is regulated to 400V DC. Fig. 43d shows the output load current (5kVA).

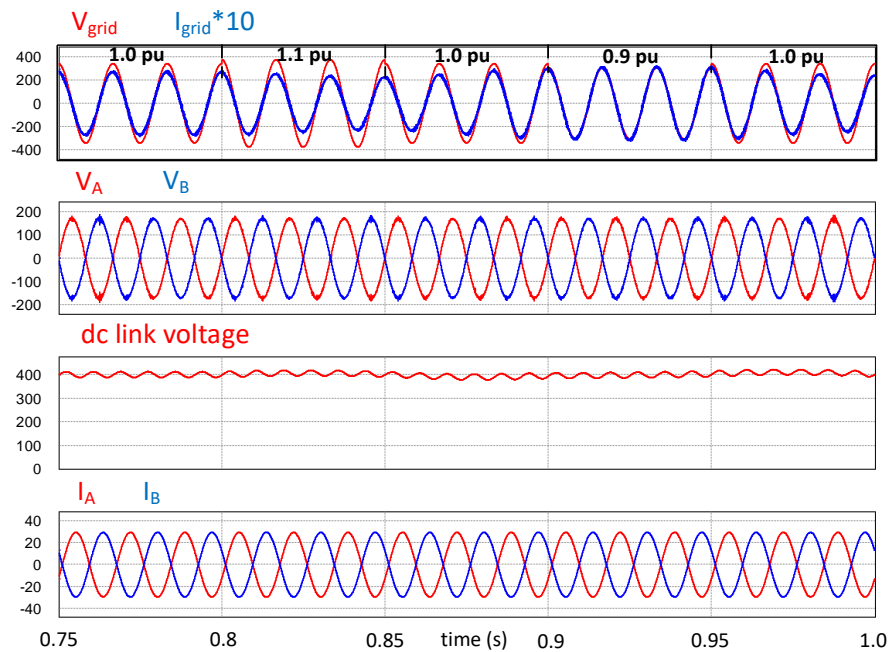


Fig. 43. PINE converter operation during normal operating conditions, a) grid voltage variations V_{grid} and input current $I_{grid} * 10$; b) Output voltages V_A and V_B ; c) dc-link voltage; d) output phase currents I_A and I_B .

Fig. 44 shows a similar operation of PINE (Fig. 33) under varying utility voltage conditions, assuming there is no power available in the PV/BESS system. For this simulation, the load is not assumed to be linear, and the control shown in Fig. 40 as proposed in [54] is used to maintain the output voltage with a Total Harmonic Distortion (THD) below 3%. It is noted that to avoid over-modulation, the dc-link was increased to 420 V.

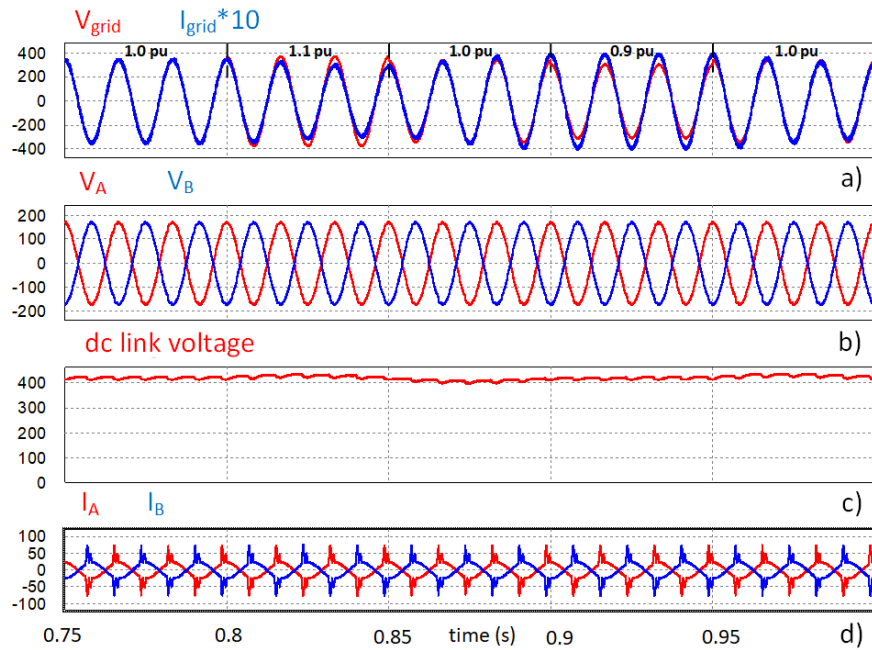


Fig. 44. PINE converter operation during normal operating conditions, a) grid voltage variations V_{grid} and input current $I_{grid} * 10$; b) Output voltages V_A and V_B (with THD < 3%); c) dc-link voltage; d) output phase currents I_A and I_B .

It is shown that even without any available energy in the PV/BESS system, the PINE topology is able to maintain a constant voltage in the load terminals, regardless of input voltage variations. Fig. 44a shows the utility input voltage varying $\pm 10\%$ and the corresponding input current, it is noted that when the input voltage increases, the input current decreases to maintain a constant dc-link voltage. The input current is controlled to be sinusoidal in phase with the input voltage. Fig. 44b shows the load voltage at the output of the PINE and is shown to be constant, regardless of the variations in the input voltage. Fig. 44c shows the dc-link voltage is regulated to 420V DC. Fig. 44d shows the output load current.

Supplying power to the grid

Fig. 45 shows the operation of the PINE converter in regen mode. In this mode the power generated by the PV panels is assumed to be 3.3kW, while the load is assumed to only consume 1.1 kW, while the battery is assumed to be charged at 1.1 kW. Since the power from PV exceeds the output load power and the excess power is fed back to the grid. Fig. 45a shows the utility input voltage and the corresponding input current. The input current is controlled to be sinusoidal and 180° out of phase with the input voltage. Fig. 45b shows the voltage and current of the BESS, charging at the rate of 1.1 kW. Fig. 45c shows the voltage and current of the PV system, generating 3.3 kW. Fig. 45d shows output load voltage and current of 562 W, with PF=0.9 (per-phase).

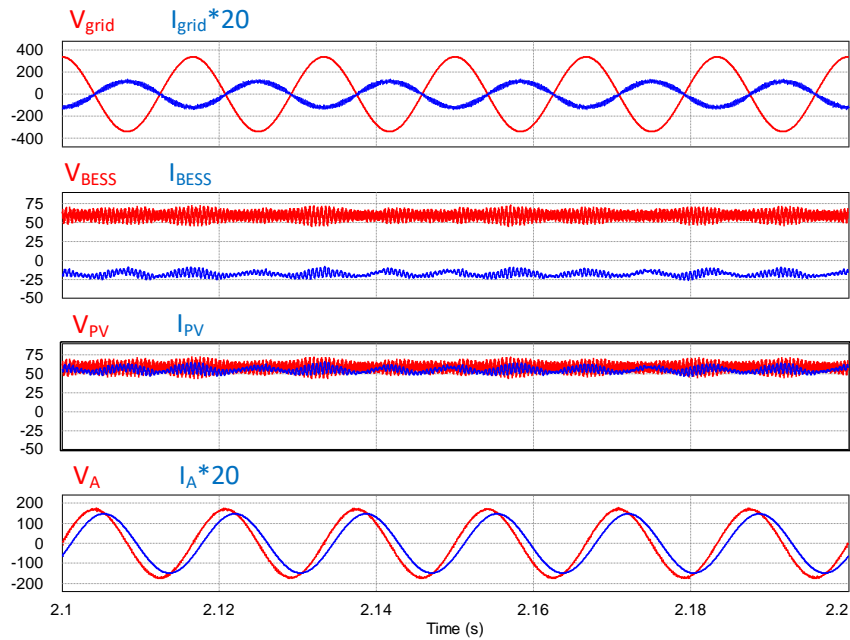


Fig. 45. PINE converter on regen mode, a) grid voltage V_{grid} and input current $I_{grid}*20$; b) BESS voltage V_{BESS} and current I_{BESS} ; c) PV panels voltage V_{PV} and current I_{PV} ; d) output phase voltage V_A and current I_A .

PINE modes of operation as the time of the day changes

In this section, several modes of operation of the proposed PINE topology are shown as the weather conditions change throughout the day, to prove the better use of renewable energy in combination with BESS.

Fig. 46 shows a typical residential customer load profile based on [60]. It can be seen that during certain brief times the load exceeds 3 kW early in the morning, or even 4 kW at the evening, but the sunlight intensity peaks around noon. This means that during the peak load times, the PINE system needs to rely on the BESS and/or the utility grid.

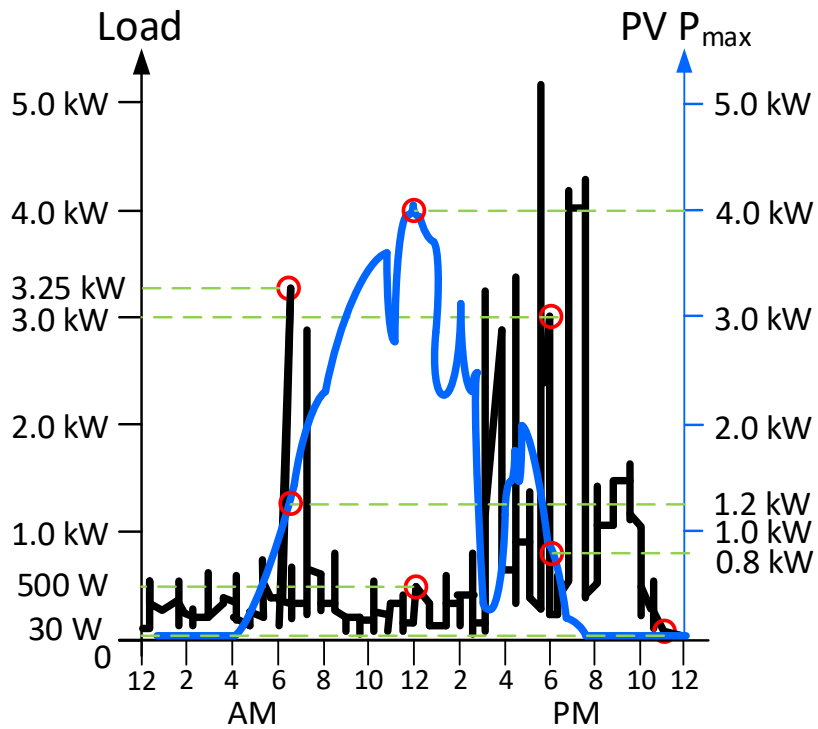


Fig. 46. Load profile of a residential load during a day (black curve). PV output power available profile (blue curve). Adapted from [60].

Table 5 summarizes the operation conditions of PINE during different times of the day. A negative sign in the power means that it is being consumed.

Table 5. Operating conditions of PINE during 4 different scenarios, as time of day changes.

Scenario	Load	PV power	BESS power	Grid power
6:30 AM	-3.25 kW	1.2 kW	1.8 kW	250 W
12:00 PM	-500 W	4.0 kW	-2.5 kW	-1 kW
6:00 PM	-3 kW	800 W	2.2 kW	-1 kVAR
11:00 PM	-30 W	0 W	-1.0 kW	1 kW -2.5 kVAR

Scenario 1

In this scenario, as shown in Fig 47, at 6:30 AM, the load demand is near its peak, at 3.25 kW, and the available power that the PV system can provide is 1.2 kW, since the BESS was previously charged, it has 1.8 kW of power available, this means that 250 W are still required from the grid.

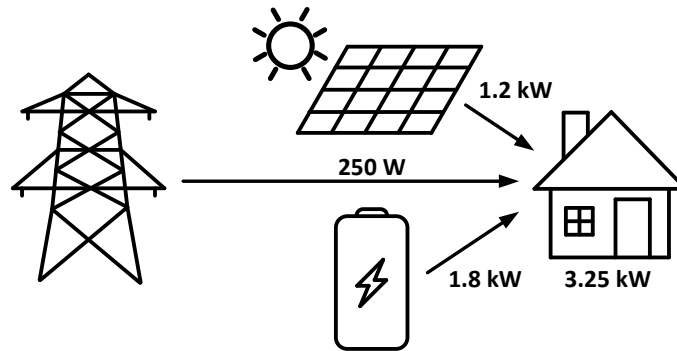


Fig. 47. Scenario at 6:30 AM, the load is near its peak, but the available power from the PV panels is low, the PINE system relies on the BESS and the grid to supply the requirements.

Fig. 48, shows the operation of the PINE topology (Fig. 33) at the simulated scenario at 6:30 AM. It is shown that nearly in the morning the load is near its peak (3.25 kW), and since the PV power available is not enough (1.2 kW) the BESS provides 1.8 kW and the grid 250 W in order to satisfy the load. Fig 48a shows the voltage and current needed to provide 250 W to the load. Fig. 48b shows the battery voltage and current needed to provide 1.8 kW to the load. Fig 48c shows the PV system voltage and current needed to provide 1.2 kW to the load. Fig 48d shows the load voltage and current of phase A at the output of the PINE.

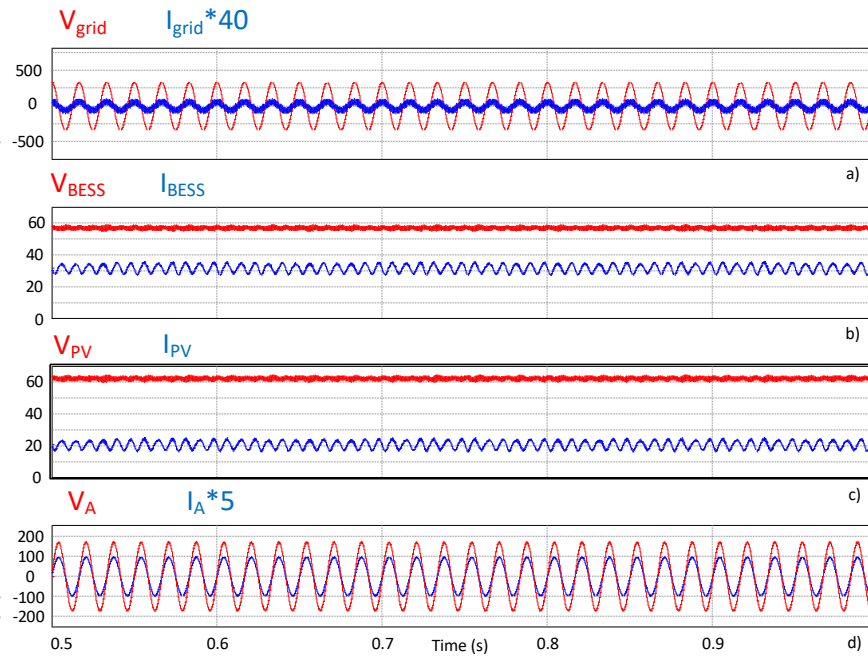


Fig. 48. PINE converter on scenario at 6:30 AM, a) grid voltage V_{grid} and input current $I_{grid} * 40$; b) BESS voltage V_{BESS} and current I_{BESS} ; c) PV panels voltage V_{PV} and current I_{PV} ; d) output phase voltage V_A and current $I_A * 5$.

Scenario 2

In this scenario, as shown in Fig. 49, at 12:00 PM, the load demand is significantly low, at 500 W, and the available power that the PV system can provide is near its peak, at 4.0 kW, after providing the power required from the load, there are 3.5 kW of power available, the system charges the BESS with 2.5 kW and provides 1.0 kW to the grid.

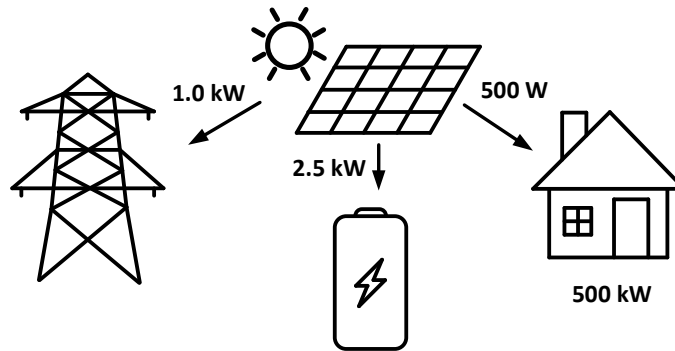


Fig. 49. Scenario at 12:00 PM, the load is near is significantly small, while the available power from the PV panels is near its peak, the PINE system charges the BESS and supplies power to the grid.

Fig. 50, shows the operation of the PINE topology (Fig. 33) at the simulated scenario at 12:00 PM. It is shown that at noon the load is significantly small (500 W), and since the PV power available is near its peak (4.0 kW), an extra supply of 3.5 kW is available, the PINE system charges the BESS with 2.5 kW and feeds the grid with 1.0 kW. Fig 50a shows the voltage and current needed to feed 1.0 kW to the grid. Fig. 50b shows the battery voltage and current needed to charge the BESS with 2.5 kW. Fig 50c shows the PV system voltage and current needed to provide 4.0 kW to the load, the BESS and the grid. Fig 50d shows the load voltage and current of phase A at the output of the PINE.

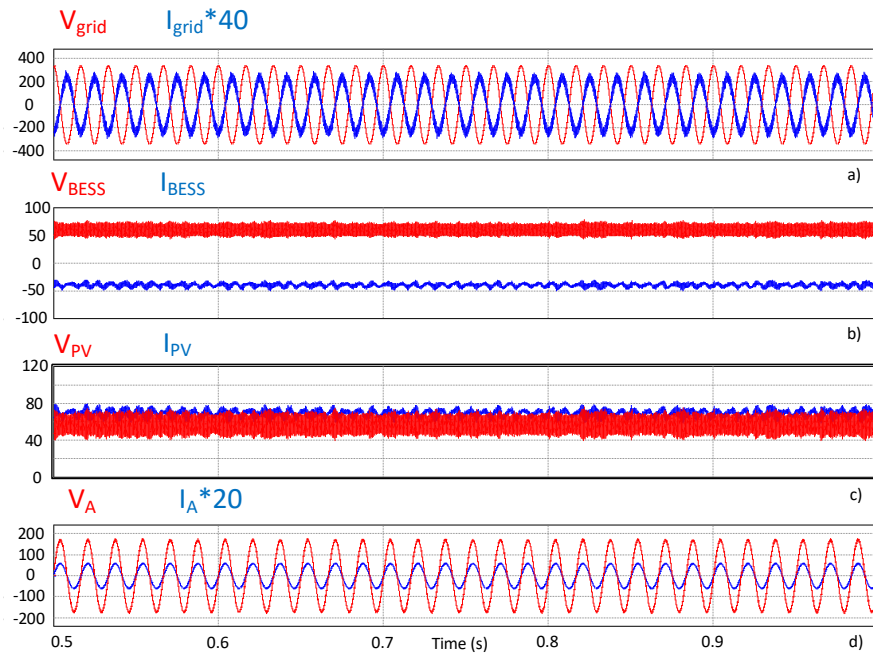


Fig. 50. PINE converter on scenario at 12:00 PM, a) grid voltage V_{grid} and input current $I_{grid} * 40$; b) BESS voltage V_{BESS} and current I_{BESS} ; c) PV panels voltage V_{PV} and current I_{PV} ; d) output phase voltage V_A and current $I_A * 20$.

Scenario 3

In this scenario, as shown in Fig 51, at 6:00 PM, the load demand is again near its peak, at 3.0 kW, and the available power that the PV system can provide is only 800 W, since the BESS has been previously charged at noon, it has 2.2 kW of power available, this means that the load can be supplied entirely from the PV/BESS system. At this time, the PINE system also provides 1 kVAR of reactive power to the grid for voltage support.

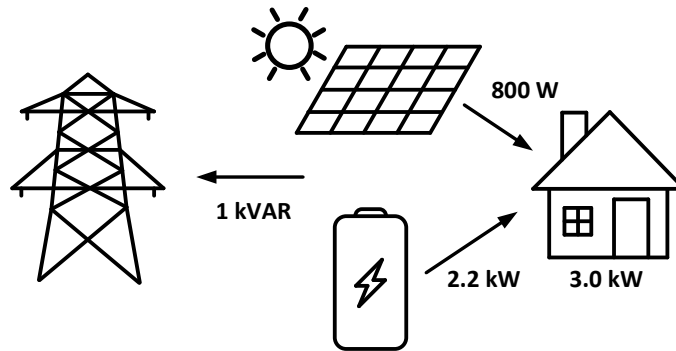


Fig. 51. Scenario at 6:00 PM, the load is near its peak, while the available power from the PV panels is small, the PINE system uses the BESS as well as the PV system to supply the needed power to the load. The grid is fed 1 kVAR of reactive power for voltage support purposes.

Fig. 52, shows the operation of the PINE topology (Fig. 33) at the simulated scenario at 6:00 PM. It is shown that at in the evening the load requirement is near its peak again (3.0 kW), and the PV power available is not enough (800 W), since the BESS has been charged at noon, it can provide the needed 2.2 kW to fully feed the load. At this point, the grid is also fed 1 kVAR of reactive power for voltage support purposes. Fig 52a shows the voltage and current needed to feed 1.0 kVAR to the grid. Fig. 52b shows the battery voltage and current needed for the BESS to supply 2.2 kW to the load. Fig 52c shows the PV system voltage and current needed to provide 800 W to the load. Fig 52d shows the load voltage and current of phase A at the output of the PINE.

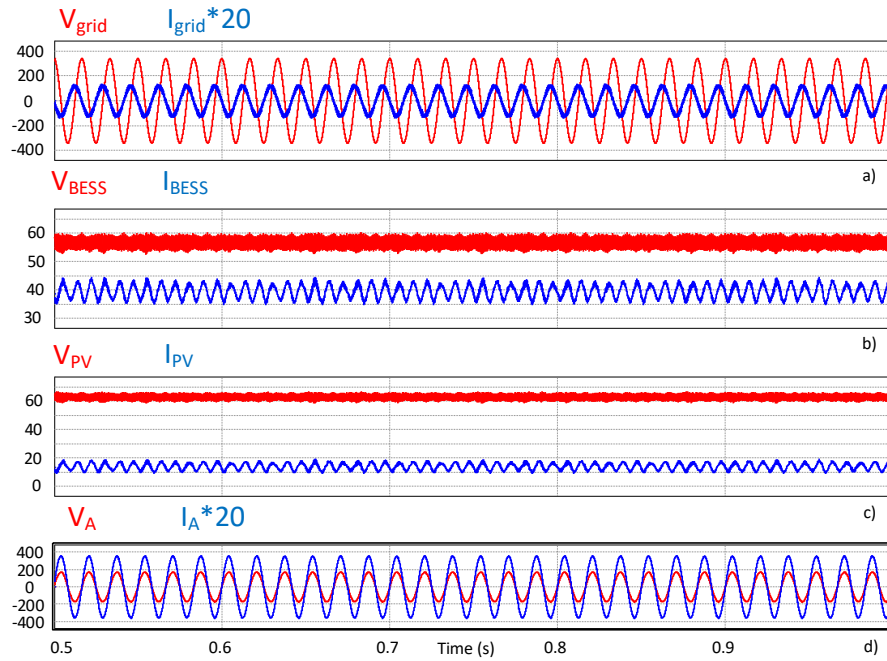


Fig. 52. PINE converter on scenario at 6:00 PM, a) grid voltage V_{grid} and input current $I_{grid} * 20$; b) BESS voltage V_{BESS} and current I_{BESS} ; c) PV panels voltage V_{PV} and current I_{PV} ; d) output phase voltage V_A and current $I_A * 20$.

Scenario 4

In this scenario, as shown in Fig. 53, at 11:00 PM, the load demand consists of only standby power loads, (30 W), and there is no available power that the PV system can provide. Considering a scenario where the electricity price is relatively low, this time of the day is chosen to charge the BESS from the grid at 1.0 kW. At this time, the PINE system also provides 2.5 kVAR of reactive power to the grid for voltage support.

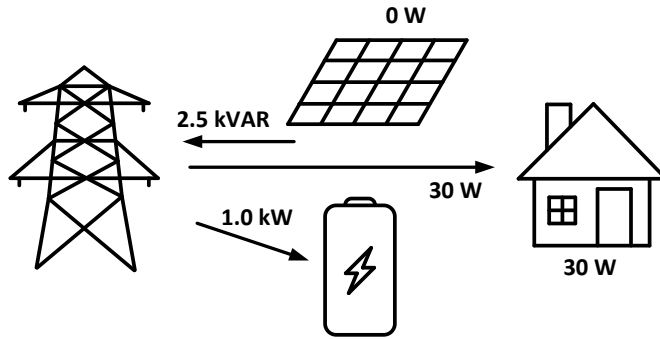


Fig. 53. Scenario at 11:00 PM, the load is significantly small, while there is no available power from the PV panels, since the electricity price is relatively low in this scenario, the PINE system charges the BESS from the grid. The grid is fed 2.5 kVAR of reactive power for voltage support purposes.

Fig. 54, shows the operation of the PINE topology (Fig. 33) at the simulated scenario at 11:00 PM. It is shown that at night the load requirement consists of only small loads (only loads consuming standby power, for 30 W), and the PV power is not available, since the electricity price is considered to be relatively small, the BESS is charged during this time from the grid. At this point, the grid is also fed 2.5 kVAR of reactive power for voltage support purposes. Fig 54a shows the voltage and current needed to charge the BESS (1 kW) considering the electricity price to be small, while feeding the grid 2.5 kVAR for voltage support. Fig. 54b shows the battery voltage and current needed for the BESS to be charged (1 kW) from the grid. Fig 54c shows the PV system voltage and current, it is noted that there is no available PV power at this time. Fig 54d shows the load voltage and current of phase A at the output of the PINE system.

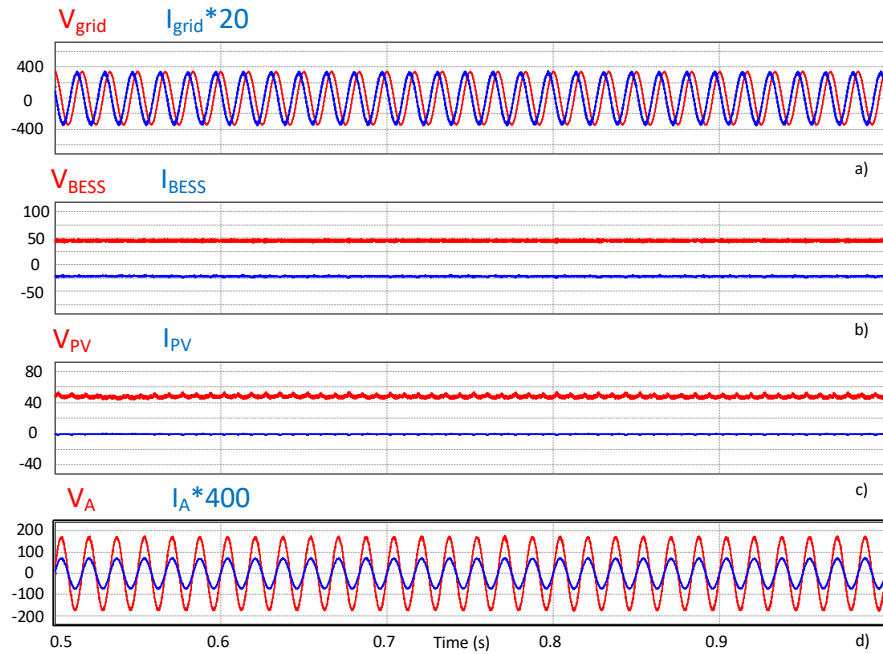


Fig. 54. PINE converter on scenario at 11:00 PM, a) grid voltage V_{grid} and input current $I_{grid} \cdot 20$; b) BESS voltage V_{BESS} and current I_{BESS} ; c) PV panels voltage V_{PV} and current I_{PV} (there is no available power from the PV system); d) output phase voltage V_A and current $I_A \cdot 400$.

Energy budgeting

In this section, examples of 2 different budgeting scenarios are presented to show how the proposed PINE can control the power flow between the microgrid and a house. Fig. 55 shows an example of reconfigured system immediately after a disaster such a hurricane passing. It can be seen that bulk transmission lines are down as well as damage to local solar generation. Circuit breakers (CB) B and C are commanded to isolate the faulted lines. The first two group of homes on the left are shown to have functioning distribution via CB-A, while the third group of homes fed by CB-3 are essentially on their

own operating in an islanded mode. Similarly, the two home groups on the right are functioning with CB-D and CB-4, CB-5 operational.

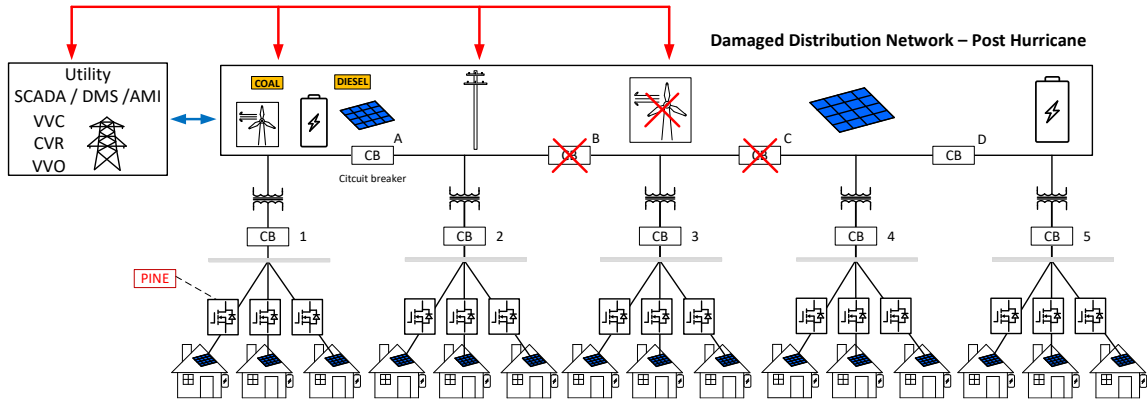


Fig. 55. Example system reconfiguration - post disaster.

In the event of a disaster, energy budgeting is envisioned i.e. each PINE is communicated with a given maximum power. The control strategy was detailed in chapter 4. Fig. 56 shows the simulation results of this strategy. In this mode the PV/BESS power is assumed to be also damaged and the available power from the grid is limited. The amount of available power keeps reducing as the disaster situation changes over time. Fig. 56a shows the output voltage of phase-A, i.e. voltage V_A as the power limitation is altered. It is noted (Fig. 56a) the output load voltage decreases as the available power is reduced as shown in Fig. 56b. It is noted that the output load voltage drops below 0.87pu due to energy budgeting control strategy.

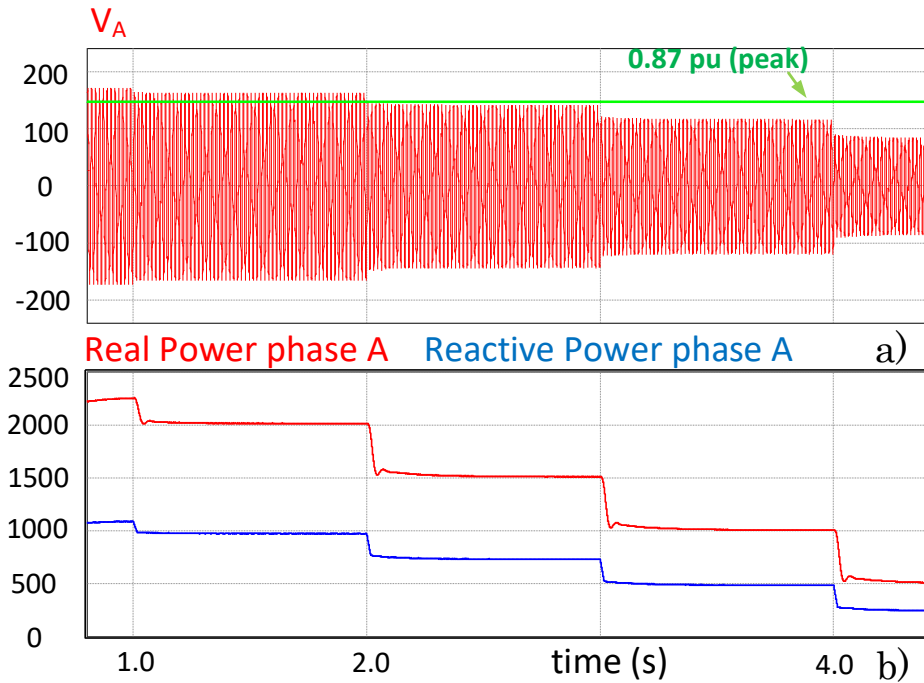


Fig. 56. Energy budgeting scenario without the ability to disconnect each load. a) output voltage V_A and a desirable limit of 0.87 pu. b) Real and Reactive power limit, as disaster evolves.

Fig. 57 shows a modified energy budgeting control strategy with the help of IoT enabled solid state circuit breakers as discussed in section V. In this approach as the available input power decreases over time (Fig. 57b), the control strategy limits the output current which in turn reduces the output voltage. This mode is allowed to continue until the output voltage approached 0.87pu. At this point, the strategy is to disconnect non-essential loads via solid state circuit breaker control. This enables the output voltage to be $0.87 \text{ pu} < V_A < 1 \text{ pu}$. Fig. 57 (a) to (c) shows the resulting waveforms.

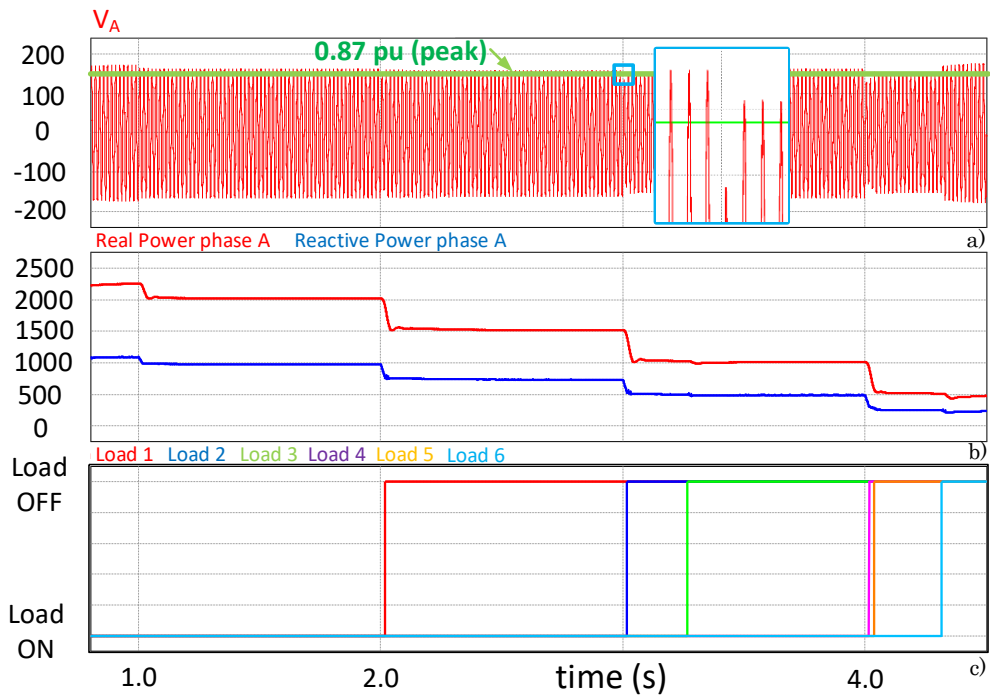


Fig. 57. Energy budgeting scenario, each time the control produces a voltage below 0.87 pu, a non-essential load is disconnected, maintaining the voltage in the allowable range. a) output voltage V_A and a desirable limit of 0.87 pu. b) Real and Reactive power limit, as disaster evolves. c) non-essential loads disconnection steps.

Hardware results

To prove the validity of the concept, a laboratory prototype of PINE is currently under development. The parameters used are shown in Table 6.

Table 6. PINE converter experimental prototype parameters.

Parameter	Magnitude
Rated power	1.14 kW
Input voltage	120 V
Input current	9.43 A
Input inductance	2.3 mH
dc link voltage	220 V
dc link capacitor	1.79 mF
Output power after energy budgeting per phase	200 W
Nominal output voltage per phase	60 V
Output voltage after energy budgeting per phase	36.6 V

Fig. 58 shows the near sinusoidal input current, minimizing both the reactive power and the harmonics injected to the grid. The dc-link voltage ripple is less than 10%. Fig. 59 shows how the Front End PWM converter maintains the dc-link voltage constant regardless of changes in the input voltage variations.

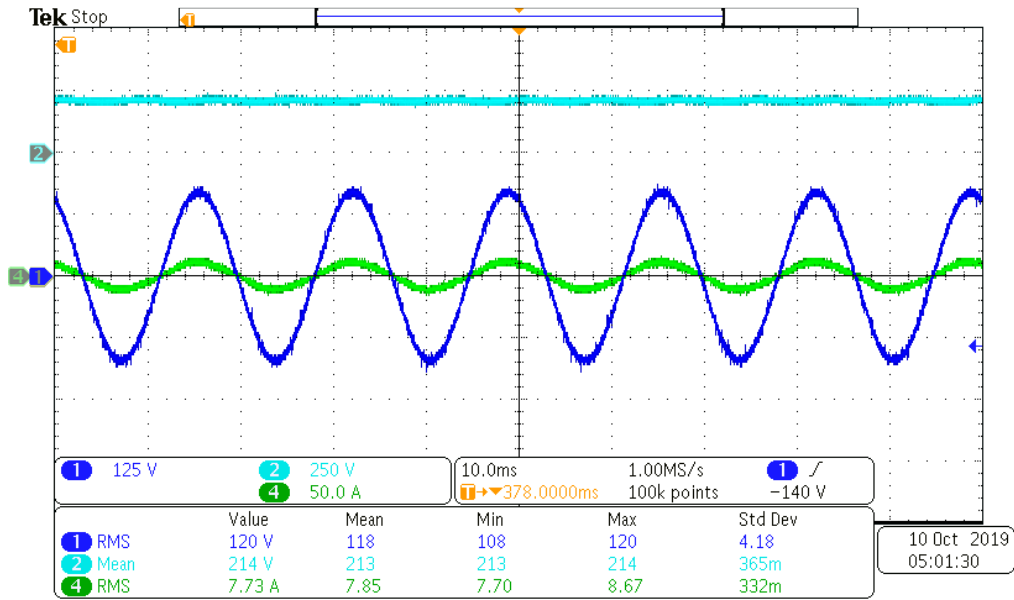


Fig. 58. Experimental waveforms of the PINE converter. Channel 1 shows the input voltage, channel 2 shows the dc-link voltage, channel 4 shows the input current.

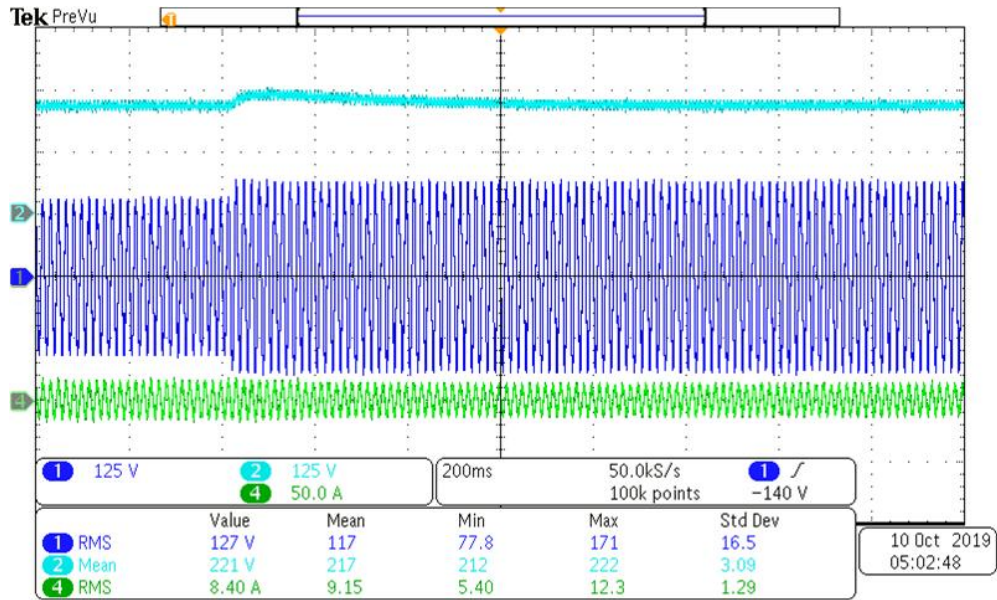


Fig. 59. Experimental waveforms for a step change input voltage. Channel 2 shows the dc-link voltage being regulated. Channel 1 shows the input current, notice the reduction due to constant power nature of PINE.

Fig. 60 shows the output voltages V_A , V_B and phase currents I_A , I_B . The energy budgeting strategy is applied to phase B only, to show how the power gets limited to 200 W, phase A remains unchanged.

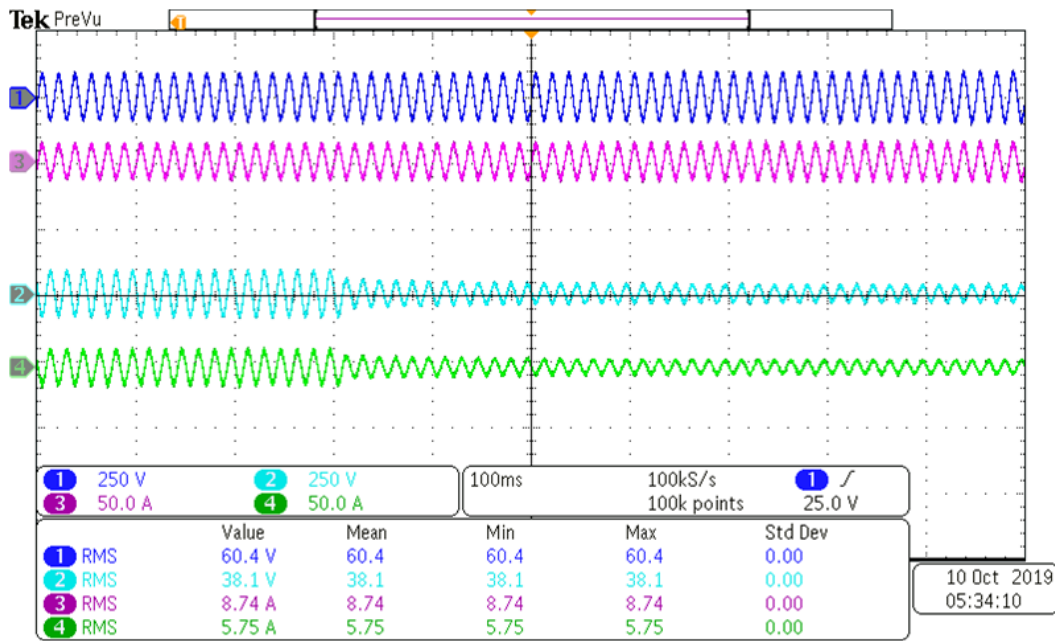


Fig. 60. Experimental waveforms for energy budgeting. Energy budgeting is applied to limit the power to 200W. Channel 1 shows output voltage V_A . Channel 3 shows phase current I_A . Channel 2 shows output voltage V_B and channel 4 shows phase current I_B .

Conclusions

In this chapter, a self-organizing power electronics converter with control intelligence at the edge of the electric distribution network has been proposed. In the proposed system the output power is processed via the PINE converter and it is shown to have several advantages. The PINE converter is shown to have the ability to implement energy budgeting when the available power is limited during a disaster situation. The power flow is shown to be bidirectional as several modes of operation of the proposed PINE topology are shown as the weather conditions change throughout the day, to prove the better use of renewable energy in combination with BESS. During normal operation the PINE approach has been shown to maintain output voltage regulated as well as reduced input current harmonic content. Simulation and experimental results from a laboratory prototype have been shown to validate the proposed concept. The proposed PINE concept has been shown to have the potential to make the future electricity delivery system more internet-like (i.e. intelligence at the network edge).

CHAPTER V

IMPLEMENTATION IMPACTS OF PINE TOPOLOGY AT THE GRID EDGE

In this chapter, the potential for improving the distribution network conditions by the PINE implementation is analyzed. Several PINE advantages are discussed in detail, such as the ability of alleviating the need for voltage regulation and the addition of Transactive Energy operations.

To address the concern about high penetration of Converter Interfaced Generation in the distribution system, in a test feeder based on the IEEE-37 test node feeder is developed and simulated using PINE interfaced loads at every node where a load is connected.

These simulations are implemented in two different realizations. The first one consists of using an average model of the PINE converter in each node representing a PINE converter. The second realization consists of simulation using all the switches of an active rectifier, dc-link and output inverter.

Introduction

In today's distribution systems, voltage variation represents one of the most significant challenges for increased PV penetration [61-63]. Voltage profile variations need to be tightly regulated because significant sags/swells might cause sensitive equipment malfunction [18]. Voltage magnitudes above or below the desired limit might cause problems such as overexcitation, insulation failure, and undesired circuit breaker trips.

Voltage magnitude regulation is typically achieved using Volt-VAR control (VVC) techniques using devices such as capacitor banks, load tap changers and voltage regulators. Traditional VVC devices are slow, centralized and there are a limited number of them in a typical distribution system. Also, there is a limit on the number of times they can operate on a given day.

Recently, new VVC solutions have been proposed to achieve the desired voltage magnitude regulation by using PV inverters for VAR injection at the edge of the grid [64]. These methods do not take into account the voltage magnitude at nodes where there is no PV inverter available [65].

In this chapter, the proposed PINE technology is shown to alleviate the need of voltage regulation for the interfaced residential customers by providing a well-regulated voltage through fast-acting power electronics regardless of fluctuations in the grid. In this manner, available voltage regulation devices only need to regulate the voltage at nodes where customers do not have PINE, as shown in Fig. 61. Also, unlike existing Volt-VAR controls, PINE enables the possibility of peer-to-peer energy transactions.

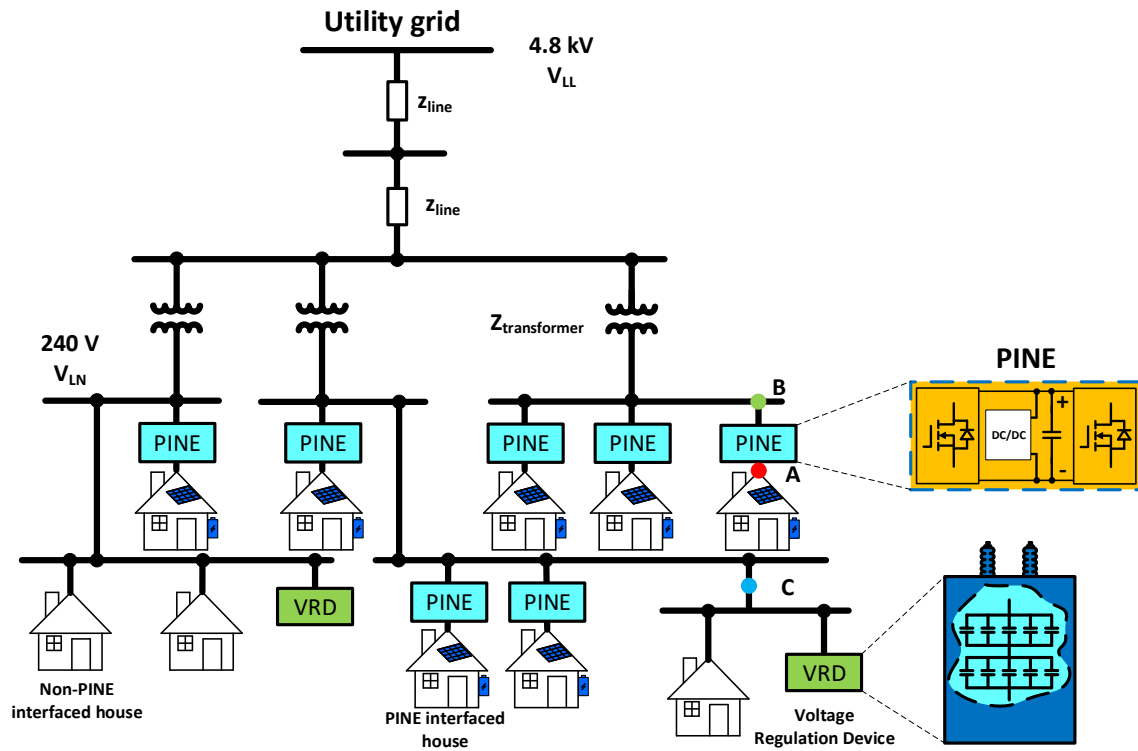


Fig. 61. Future distribution power system with PINE technology installed at different locations. Only nodes where customers do not have PINE installed need to be regulated by Voltage Regulation Devices (VRD). Node A represents the load connection point at a PINE-interfaced house. Node B represents the grid connection point of a PINE-interfaced house. Node C represents the grid connection point of a non-PINE interfaced house.

Before the massive deployment of power electronics devices such as PINE, it is imperative to investigate the physical impact of such services on the legacy distribution grid. Time-domain simulations are performed to simulate a distribution grid with high penetration of PINE, resulting in a stable operation of the system.

PINE average model

In order to simulate a high number of PINE connected residential loads, an average model of the topology was developed in the dq frame.

Front End PWM converter average model

Fig. 62 shows the equivalent circuit of the fundamental frequency (60 Hz) of the Front End PWM converter connected to the grid. It can be seen that the converter and the grid are interfaced by an input impedance (L_{in} , R_{in}).

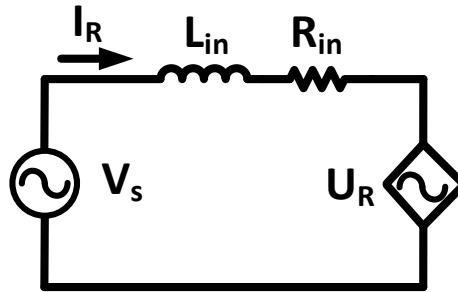


Fig. 62. Equivalent circuit of the Front End PWM converter fundamental component (60 Hz) connected to the grid.

Using Kirchhoff's voltage law (KVL) around this circuit, equation (5.1) is obtained.

$$V_s = L_{in} \frac{d}{dt} I_R + R_{in} I_R + U_R \quad (5.1)$$

Where: V_s is the grid voltage, L_{in} is the input inductance, R_{in} is the input resistance, I_R is the input current, and U_R is the fundamental component of the voltage at the terminals of the Front End PWM converter.

As explained in the first chapter, two orthogonal values are needed to obtain the dq frame equivalent circuit. The original circuit can be referred to as α , and the orthogonal equivalent is named β . By using the Park transformation, the equivalent circuits can be obtained as equations (5.2 – 5.4):

$$V_{sd} = -\omega L_{in} I_{Rq} + L_{in} \frac{d}{dt} I_{Rd} + U_{Rd} + R_{in} I_{Rd} \quad (5.2)$$

$$V_{sq} = \omega L_{in} I_{Rd} + L_{in} \frac{d}{dt} I_{Rq} + U_{Rq} + R_{in} I_{Rq} \quad (5.3)$$

$$I_O = \frac{U_{Rd} I_{Rd} + U_{Rq} I_{Rq}}{2V_{DC}} \quad (5.4)$$

Where: V_{sd} is the d component of the grid voltage, V_{sq} is the q component of the grid voltage, I_{Rd} and I_{Rq} , are the dq components of the input current, U_{Rd} and U_{Rq} , are the dq components of the voltage terminals of the Front End PWM converter, L_{in} is the input inductance, R_{in} is the input resistance, I_O is the dc current and ω is the electrical frequency of the grid voltage ($\omega = 2\pi f$ in rad/sec). Fig. 63 shows the equivalent circuits.

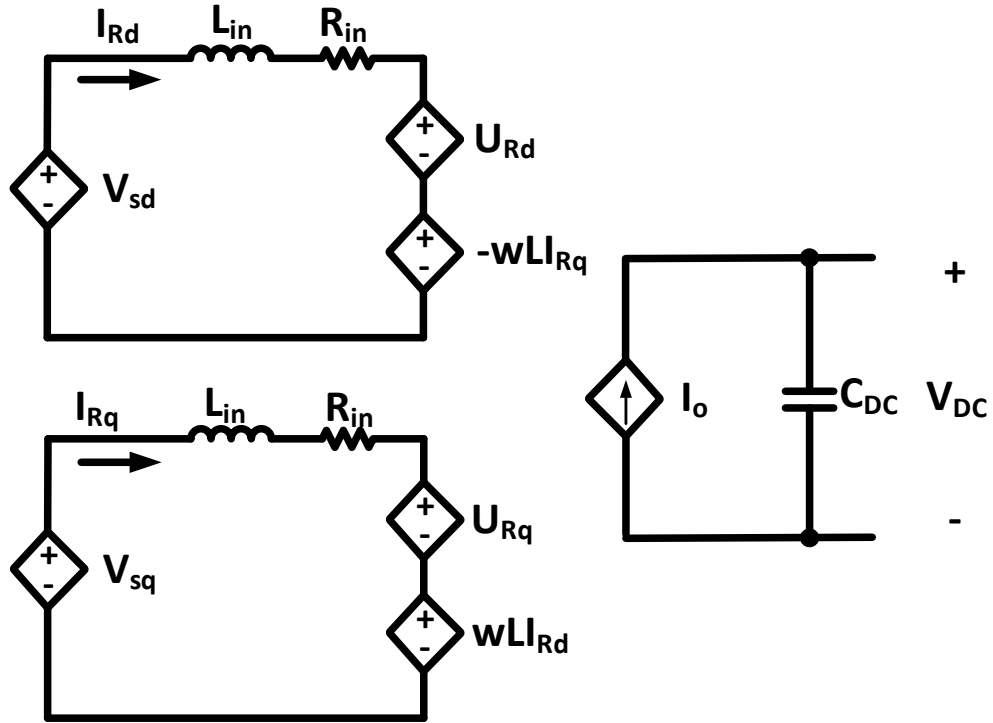


Fig. 63. Equivalent circuit of the Front End PWM connected to the grid in the dq frame.

Output PWM converter average model

In a similar manner, the average model of the output PWM converter is obtained by using both Kirchhoff's voltage and current laws (KVL and KCL), since the output voltage consists of a split phase ac output (120/240V, 60 Hz), an average model is developed for phase A and another for phase B. The model for phase A results in equations (5.5 - 5.8):

$$U_{Ad} = L_f \frac{d}{dt} I_{Ad} + wL_f I_{Aq} + V_{Ad} \quad (5.5)$$

$$U_{Aq} = L_f \frac{d}{dt} I_{Aq} - wL_f I_{Ad} + V_{Aq} \quad (5.6)$$

$$I_{Ad} = C_f \frac{d}{dt} V_{Ad} + \omega C_f V_{Aq} + \frac{V_{Ad}}{Z_d} \quad (5.7)$$

$$I_{Aq} = C_f \frac{d}{dt} V_{Aq} - \omega C_f V_{Ad} + \frac{V_{Aq}}{Z_q} \quad (5.8)$$

Where: U_{Ad} is the d component of the voltage terminals of the Output PWM converter, U_{Aq} is the q component of the voltage terminals of the Output PWM converter, I_{Ad} and I_{Aq} , are the dq components of the current flowing through the inductance L_f , V_{Ad} , and V_{Aq} are the dq component at the output terminals, Z_d and Z_q are the dq components of the load model, L_f is the inductance of the filter, C_f is the filter capacitance. Since the load was modeled as a resistor, Z_d is modeled as a resistance and Z_q is not considered for the simulations in this chapter. Fig. 64 shows the equivalent circuits.

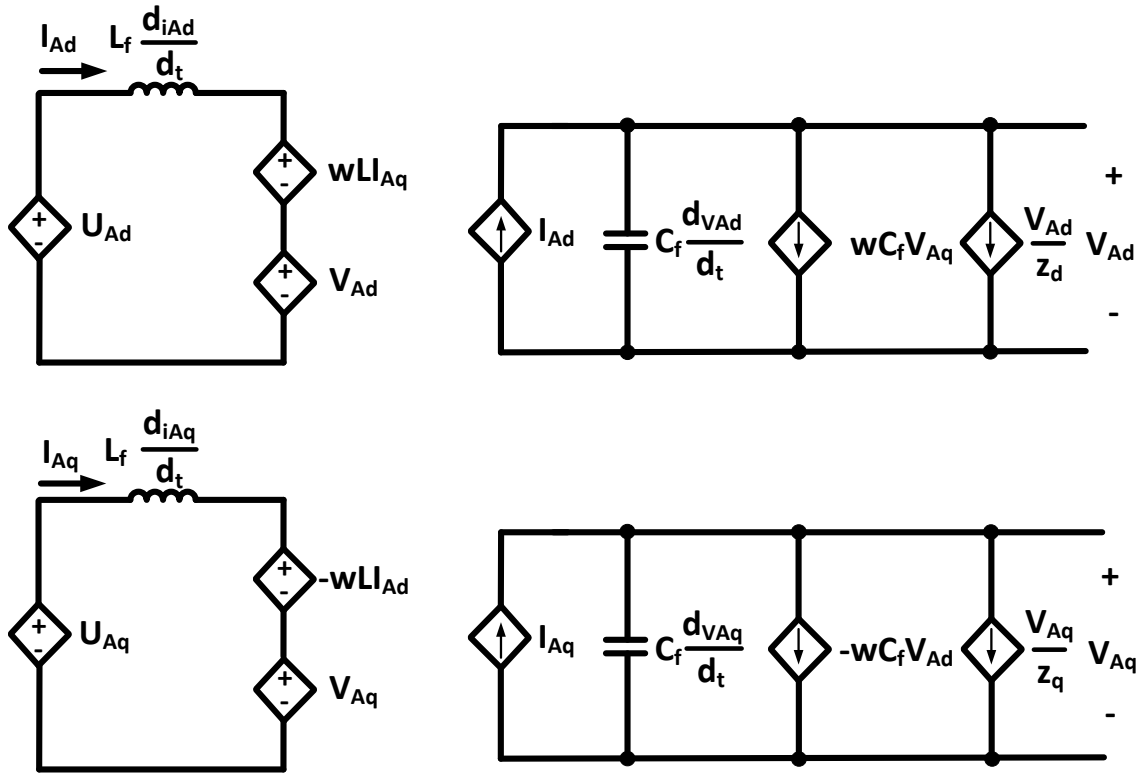


Fig. 64. Equivalent circuit of the Output PWM converter phase A. The phase B is modeled in a similar manner.

Demonstration of PINE's value on a small distribution system

To demonstrate the benefits brought by the proposed concept for both PINE-interfaced and non-PINE-interfaced residential customers as well as for the distribution system operator, a small distribution system is simulated using the PINE average model. The mentioned distribution system, as shown in Fig. 65, has two residential loads respectively at nodes B and C, and one capacitor bank to regulate voltages at B and C to be within the required range between 0.87 pu and 1.06 pu.

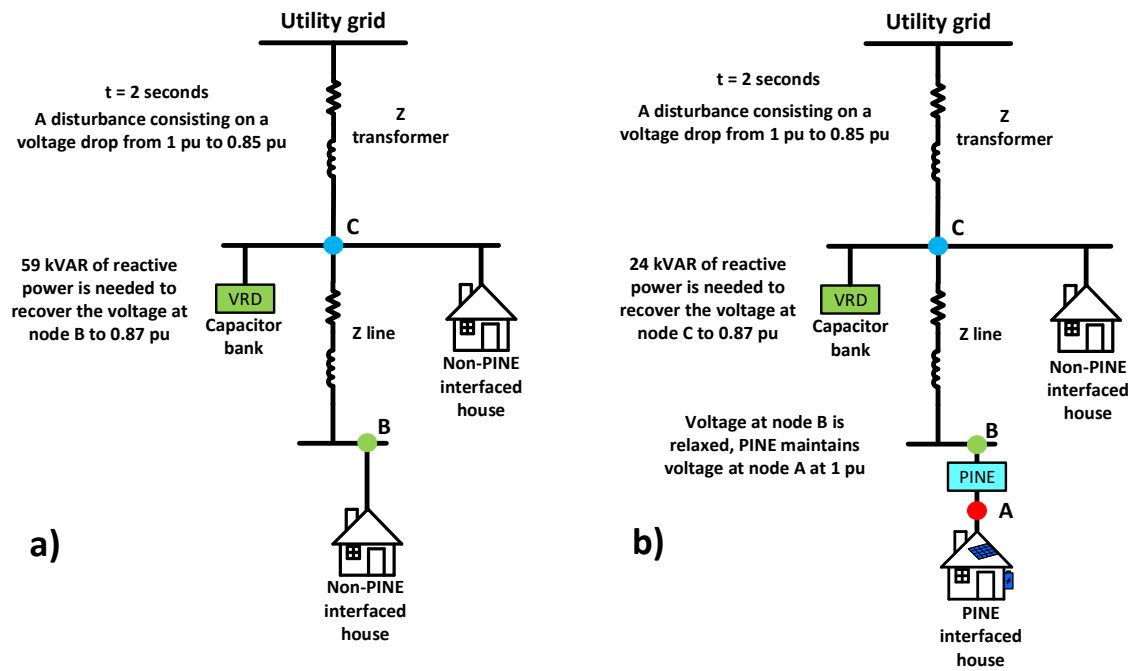


Fig. 65. A simple distribution system with/without PINE technology. (a) Traditional distribution system without PINE. (b) Distribution system with PINE.

Consider a disturbance causing the grid voltage to drop from 1.0 pu to 0.85 pu at $t = 2$ seconds, the capacitor bank at $t = 3$ seconds will switch in more capacitors, inject more reactive power and regulate voltages at B and C to meet minimum requirement, i.e. 0.87 pu. If without PINE technology, both voltages at B and C need to be tightly regulated and the required reactive power from the capacitor bank turns out to be 59 kVAR. The system dynamics over this process are shown in Fig. 66. It shows that both residential customers will experience the voltage dip from $t = 2$ seconds to $t = 3$ seconds and their voltage recoveries both rely on the capacitor bank at C.

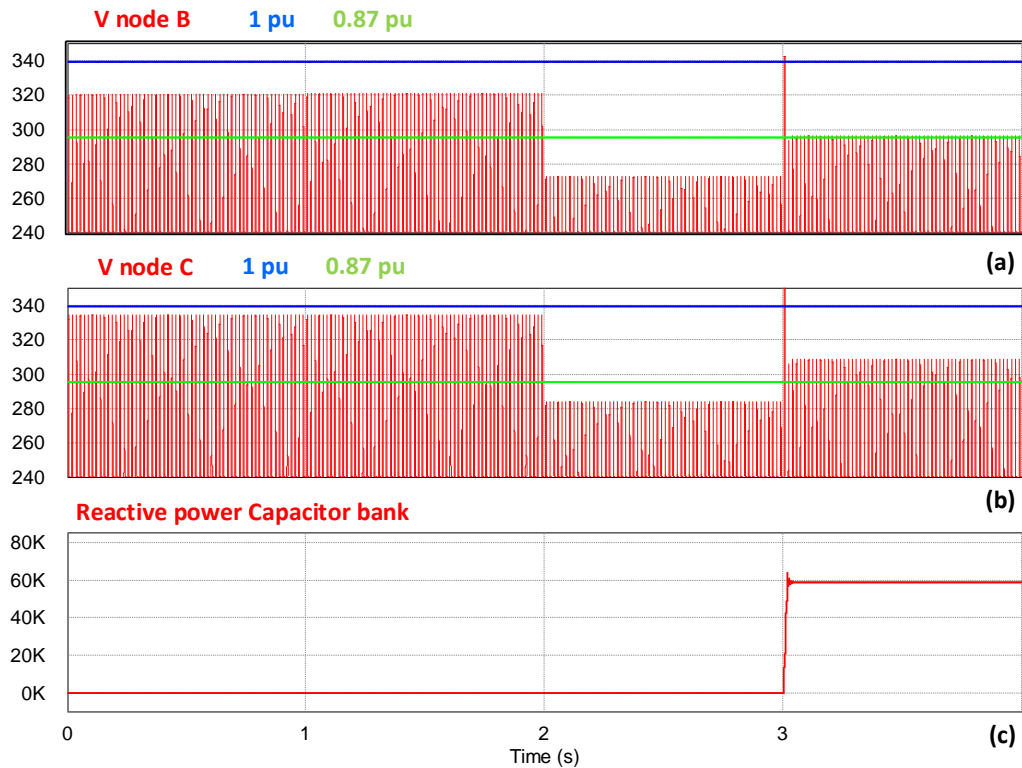


Fig. 66. System dynamics subject to the disturbance: phase voltage profile and reactive power support without PINE. (a) Voltage at node B. (b) Voltage at node C. (c) needed reactive power to regulate voltages at nodes B and C to meet minimum requirement i.e. 0.87 pu.

With PINE technology installed for the residential house at B, as shown in Fig. 65b, the regulation of voltage at B can be relaxed without compromising the quality of the electricity service. According to the system dynamics shown in Fig. 67, the residential customer behind PINE can hardly feel the disturbance from the utility grid and can always enjoy the ideal 1.0 pu voltage. In this case, only voltage at C needs to be regulated while the required reactive power from the capacitor bank is only 24 kVAR. In addition, the

non-PINE-interfaced house at C can also enjoy a better electricity service since there are more reactive power reserve to regulate its voltage profile.

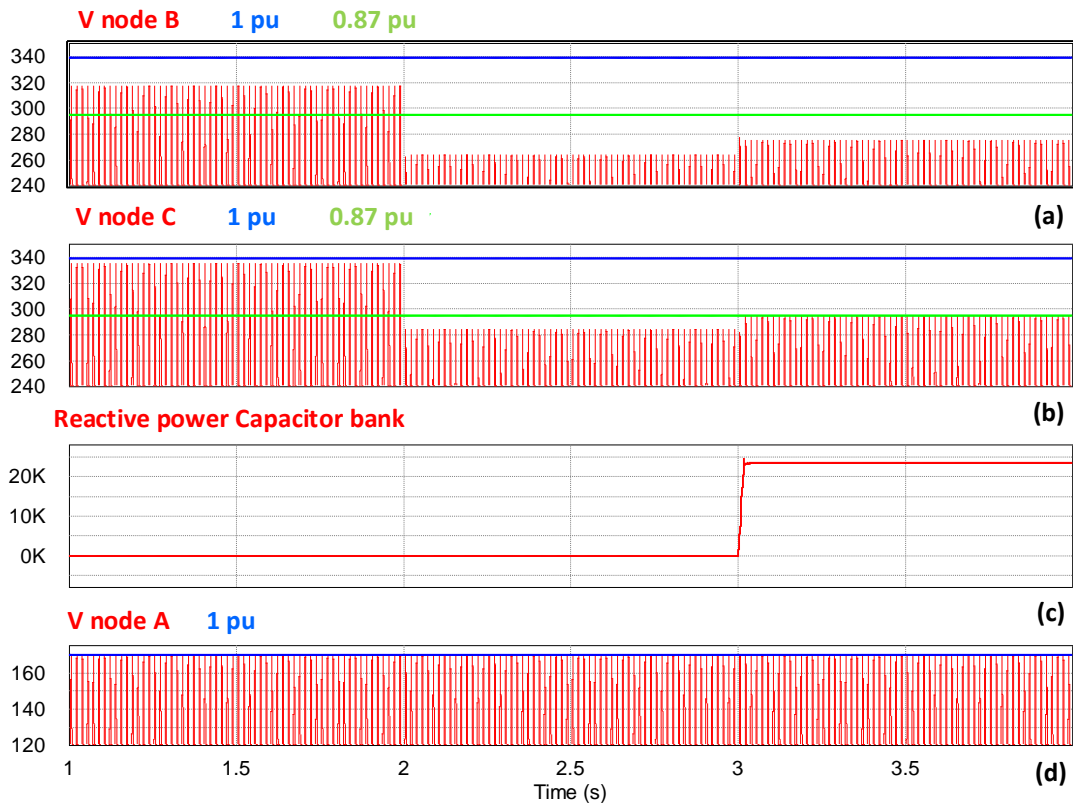


Fig. 67. System dynamics subject to the disturbance: phase voltage profile and reactive power support with PINE at node B. (a) Voltage at node B. (b) Voltage at node C. (c) needed reactive power to regulate only voltage node C (since PINE is regulating its own load voltage, node A) to meet minimum requirement i.e. 0.87 pu. (d) Voltage at node A, or load voltage of PINE interfaced load.

Increased penetration levels of PINE in a residential distribution system

Fig. 68 shows a modified test node feeder based on IEEE 37 node system [66] and reference [67]. It can be seen that every residential load in this system is interfaced to the grid through PINE. This illustrates 100% PINE penetration. An example node 41 (Fig. 68)

shows a distribution system node containing residential loads. It can be seen that the distribution voltage is 4.8kV, which is transformed to 120V/240V via a step down transformer followed by three loads of 5kVA (one per phase) supplied via PINE. A total of 8 such nodes with 24 PINE installations are shown in Fig. 68, (nodes 7, 8, 9, 25, 38, 39, 40, and 41).

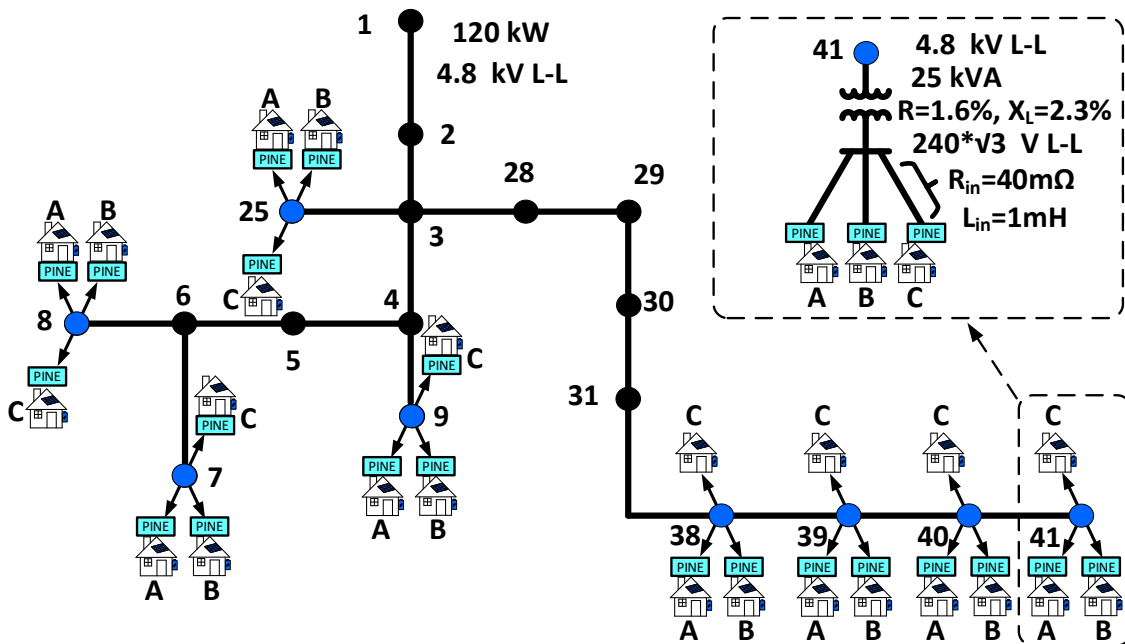


Fig. 68. Test feeder used to simulate high penetration levels of PINE in a distribution feeder, based on the IEEE-37 test node feeder. Note: line impedances between nodes are specified in Appendix A. Adapted from [67].

Fig. 69 shows the configuration of each node in detail, it can be seen that every node is considered to have a step down transformer that steps down the voltage from 4.8kV

to 120V/240V. Each node has three PINE loads, one per phase, as explained earlier, each PINE load consists of a split phase ac output (120/240V, 60Hz) designed for the typical residential load.

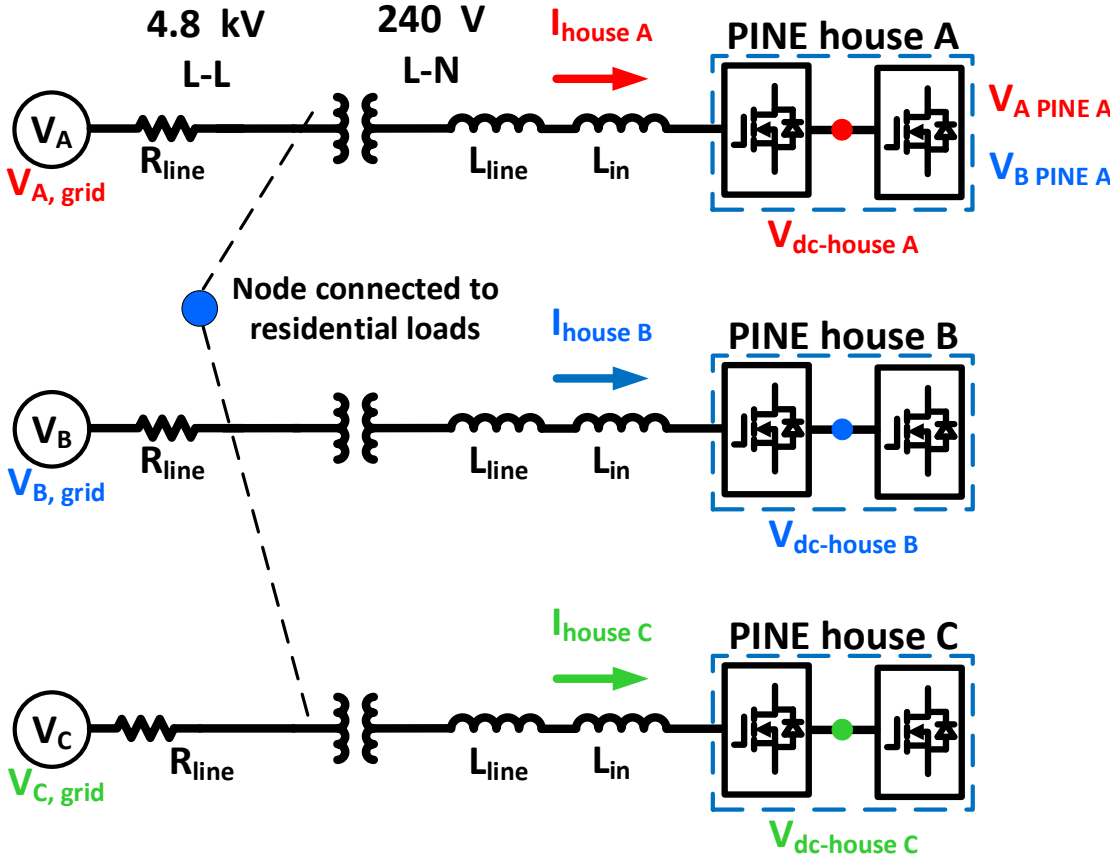


Fig. 69. Detailed configuration of each node containing loads (every blue node in Fig. 68).

Simulation with average model

The average model developed in this chapter is used to simulate such a system and the results are discussed in this section.

Fig. 70 shows the distribution grid voltage (4.8kV) increase by 10% at $t = 0.5$ sec. Fig. 70b shows the node 38 input currents drawn by each PINE. A decrease in the input current is noted (Fig. 70b) for a corresponding increase in input voltage (Fig. 70a) due to the constant power nature of the PINE converter. Fig. 70c shows the input power fluctuation. Fig. 70c shows that the power consumed by the load at node 38 maintains unchanged before and after the disturbance in the grid voltage. This seems to be the reason that a load controlled by constant power strategy is named CPL in literature. However, it should be emphasized that a load controlled to behave like a CPL is significantly different from an ideal CPL, whose behaviors are dominated by a pure algebraic equation and tend to cause instability. The load controlled to consume a constant power, or we call it dynamic CPL load, possesses differential state variables associated with its control, like the load at node 38. It should also be noted that in reality almost all CPLs are dynamic CPLs. Therefore, the negative impedance induced instability in DC circuit does not necessarily exist in systems with dynamic CPLs, as shown by the system responses in dc-link voltage and load power in Fig. 70 that the system is quite stable. In fact, the stability of the system with dynamic CPLs is highly dependent on the control design of the load.

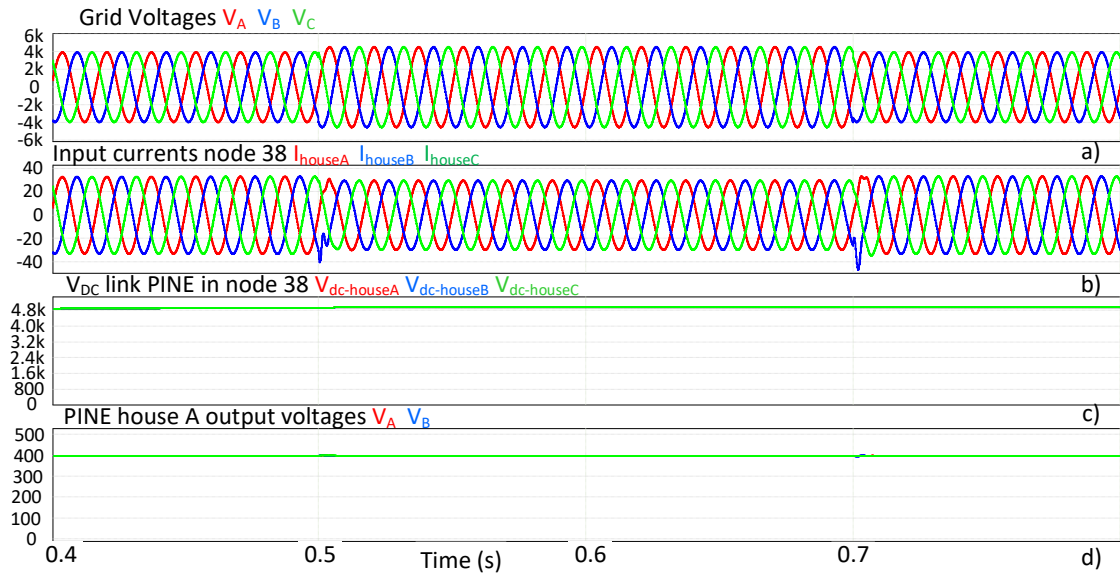


Fig. 70. Simulation results for a distribution grid with 100% PINE penetration level. As seen in Fig. 69, each node has three connected PINE enabled homes, one per phase; a) Grid voltages phases A, B and C; b) input current of PINE enabled homes in node 38; c) Real power of PINE enabled homes in node 38; d) dc-link voltage of PINE enabled homes in node 38.

Simulation with switching converters

In this section, in order to validate the developed PINE average model results, the same distribution grid is simulated in more detail. This is done by simulating the Front End PWM converter and the Output PWM converter of each PINE using a recently developed tool (DSIM). This tool enables the simulation of considerable amounts of switches in a small amount of time. The voltage variations are realized by simulating the resistance losses along the lines by modifying the resistance R_{line} between nodes 1 and 2 (see Figs. 68 and 69).

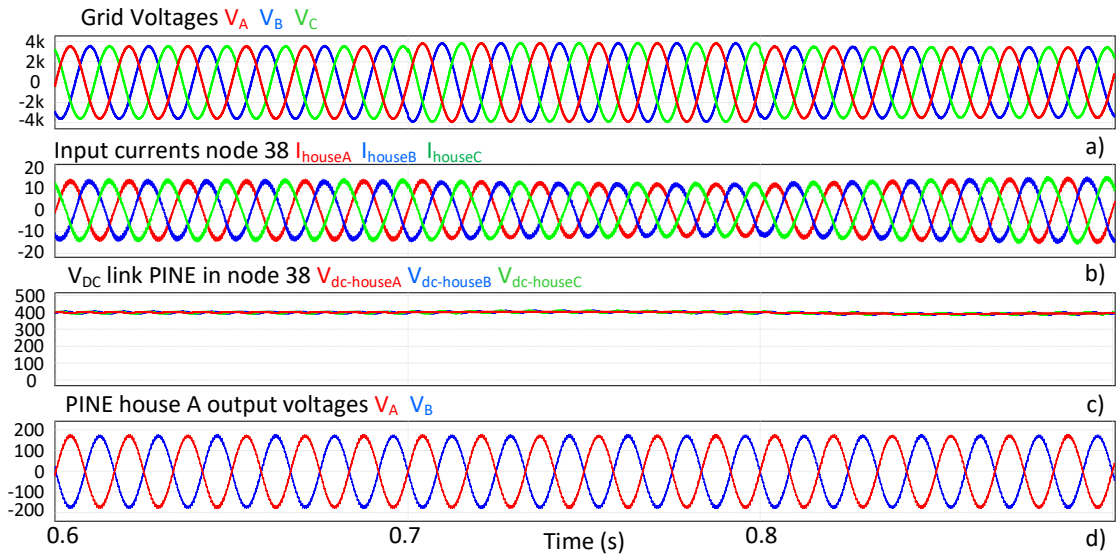


Fig. 71. Simulation results for a distribution grid with 100% PINE penetration level, for the switching converters simulation. As seen in Fig 69, each node has three connected PINE enabled homes, one per phase; a) Grid voltages phases A, B and C; b) input current of PINE enabled homes in node 38; c) dc-link voltage of PINE enabled homes in node 38; d) output voltages V_A and V_B of PINE load connected at node 38, phase A.

The results of the simulation using switching converters are discussed in this section. It can be seen that due to the use of switches instead of average models, the results are more detailed, allowing to observe the current harmonics. Fig. 71a shows the distribution grid voltage (4.8kV) increase by 9% at $t = 0.7$ sec, and returning to its rated value at $t=0.8$ sec. Fig. 71b shows the node 38 input currents drawn by each PINE. A decrease in the input current is noted (Fig. 71b) for a corresponding increase in input voltage (Fig. 71a) due to the constant power nature of the PINE converter. Fig. 71c shows that the dc-link voltage ripple in each PINE load is smaller than 4%. Fig 71d shows the

output voltage of the PINE load connected at node 38, phase A, it can be seen that the customer has a constant voltage, regardless of voltage variations in the grid.

Conclusions

In this chapter, the potential for improving the distribution network conditions by the PINE implementation was discussed. Simulation results on a distribution system with high penetration of PINE were done, it was shown that the distribution system was stable. Simulations were done using an average model of the Front End PWM converter and the Output PWM converter of PINE and by a regular simulation using switching converters. A test feeder based on the IEEE-37 test node feeder was developed to implement both simulations, representing a distribution system with 100% PINE penetration.

CHAPTER VI

SUMMARY

Conclusion

In summary, new power electronics topologies, as well as a power flow control strategy were proposed and analyzed to improve the control of the grid. In chapter two, a topology named Power Electronics Transformer with Dynamic Voltage and Angle Droop Control (PET-DVADC) was introduced, using fractionally rated transformers coupled with AC-AC converters to enable accurate angle droop control without the use of a dc-link stage. The third chapter introduced a modified angle droop control scheme intended to be used with the previously introduced power router. The proposed control scheme enables energy transactions between peers, which was studied and analyzed using different operation scenarios to prove the validity of the control scheme.

The fourth chapter introduced a new topology, named Power Electronics Intelligence at the Network Edge (PINE), this topology interfaces PV/BESS systems with the grid in residential applications. PINE introduces several advantages to the distribution grid, enabling high levels of PV penetration in the grid, targeting even 100%. The power flow is shown to be bidirectional and the PINE topology has been shown to maintain load voltage regulated as well as reduced input current harmonic content. Simulation and experimental results from a laboratory prototype have been shown to validate the proposed concept.

The fifth chapter analyzes the impacts that PINE can have in a distribution grid, using an average model to simulate 24 PINE models, the average model is further

validated by simulating PINE with switching converters. By using PINE, the voltage regulation requirements decrease, since each PINE guarantees the appropriate voltage level at each customer's load. An example test node feeder is developed based on the IEEE 37 test node feeder, to prove that the system is stable. The advantages of PINE are also discussed in a small distribution system, proving that PINE can alleviate the need for voltage regulation in the distribution system.

Future Work

There are several areas of possible future work in this dissertation. For the introduced topology in chapter two (PET-DVADC), an average model can be included in the angle droop control analysis, and a comparison with the traditional implementations can be done.

For the modified angle droop control technique presented in chapter three, more detailed microgrids can be included in future simulations, including renewable sources of energy models, as well as BESS, a laboratory scale prototype can be used to prove the concept using Hardware in the Loop (HIL) systems.

For the PINE concept discussed in chapter four, the laboratory scale prototype can be further developed, the power ratings can be increased, and a control strategy to minimize the required dc-link capacitor can be included.

The average model of PINE, as well as the test node feeder used in chapter five can be used to further analyze the advantages of PINE, such as losses reduction in the distribution system, Transactive Energy operations between peers, minimization of harmonics in the distribution grid, etc.

REFERENCES

- [1] International Energy Agency (2017), “World Energy Outlook 2017” [Online]. Available <https://www.iea.org/reports/world-energy-outlook-2017>. [Accessed on: March 20, 2020]
- [2] Y. Zhang and L. Xie, “A Transient Stability Assessment Framework in Power Electronic-Interfaced Distribution Systems,” in *IEEE Transactions on Power Systems*, vol. 31, no. 6, pp. 5106-5114, Nov. 2016.
- [3] N. Hatziargyriou, H. Asano, R. Iravani and C. Marnay, “Microgrids,” in *IEEE Power and Energy Magazine*, vol. 5, no. 4, pp. 78-94, July-Aug. 2007.
- [4] J. A. P. Lopes, C. L. Moreira and A. G. Madureira, “Defining control strategies for MicroGrids islanded operation,” in *IEEE Transactions on Power Systems*, vol. 21, no. 2, pp. 916-924, May 2006.
- [5] F. Katiraei, R. Iravani, N. Hatziargyriou and A. Dimeas, “Microgrids management,” in *IEEE Power and Energy Magazine*, vol. 6, no. 3, pp. 54-65, May-June 2008.
- [6] A. G. Tsikalakis and N. D. Hatziargyriou, “Centralized Control for Optimizing Microgrids Operation,” in *IEEE Transactions on Energy Conversion*, vol. 23, no. 1, pp. 241-248, March 2008.
- [7] D. E. Olivares et al., “Trends in Microgrid Control,” in *IEEE Transactions on Smart Grid*, vol. 5, no. 4, pp. 1905-1919, July 2014.
- [8] B. Kroposki, R. Lasseter, T. Ise, S. Morozumi, S. Papathanassiou and N. Hatziargyriou, “Making microgrids work,” in *IEEE Power and Energy Magazine*, vol. 6, no. 3, pp. 40-53, May-June 2008.
- [9] J. M. Guerrero, L. Hang and J. Uceda, “Control of Distributed Uninterruptible Power Supply Systems,” in *IEEE Transactions on Industrial Electronics*, vol. 55, no. 8, pp. 2845-2859, Aug. 2008.
- [10] J. A. Ramos-Ruiz, P. Enjeti and L. Xie, “Peer-to-peer Energy Transaction in Microgrids with Power Electronics Enabled Angle Droop Control,” 2018 IEEE Electronic Power Grid (eGrid), Charleston, SC, 2018, pp. 1-6.
- [11] Y. Zhang and L. Xie, “Online dynamic security assessment of microgrid interconnections in smart distribution systems,” *Power Systems, IEEE Transactions on Power Systems*, vol. 30, no. 6, pp. 3246–3254, 2015.

- [12] US Department of Energy, “The history of solar”, [Online]. Available: https://www1.eere.energy.gov/solar/pdfs/solar_timeline.pdf. [Accessed on: March 20, 2020]
- [13] NASA science, “How do photovoltaics work?”, [Online]. Available: <https://science.nasa.gov/science-news/science-at-nasa/2002/solarcells>. [Accessed on: March 20, 2020].
- [14] M. A. Islam, A. Merabet, R. Beguenane and H. Ibrahim, “Modeling solar photovoltaic cell and simulated performance analysis of a 250W PV module,” 2013 IEEE Electrical Power & Energy Conference, Halifax, NS, 2013, pp. 1-6.
- [15] S. B. Kjaer, J. K. Pedersen, and F. Blaabjerg, “A review of single-phase grid-connected inverters for photovoltaic modules,” IEEE Trans. Ind. Appl., vol. 41, no. 5, pp. 1292–1306, Sep./Oct. 2005.
- [16] V. Vega-Garita, L. Ramirez-Elizondo, G. R. C. Mouli and P. Bauer, “Review of residential PV-storage architectures,” 2016 IEEE International Energy Conference (ENERGYCON), Leuven, 2016, pp. 1-6.
- [17] M. Castillo-Cagigal, A. Gutiérrez, F. Monasterio-Huelin, E. Caamaño-Martín, D. Masa, J. Jiménez-Leube, “A semi-distributed electric demand-side management system with PV generation for self-consumption enhancement,” Energy Conversion and Management, vol. 52, Issue 7, 2011, pp. 2659-2666.
- [18] Power Quality World, “CBEMA curve – the power acceptability curve for computer business equipment”, [Online]. Available: <http://www.powerqualityworld.com/2011/04/cbema-curve-power-quality-standard.html>. [Accessed on: March 20, 2020].
- [19] P. Kundur, (1994). “Power System Stability and Control”. New York: McGrawHill.
- [20] A. S. Dobakhshari, S. Azizi and A. M. Ranjbar, “Control of microgrids: Aspects and prospects,” 2011 International Conference on Networking, Sensing and Control, Delft, 2011, pp. 38-43.
- [21] B. Bahrani, A. Rufer, S. Kenzelmann and L. A. C. Lopes, “Vector Control of Single-Phase Voltage-Source Converters Based on Fictive-Axis Emulation,” in IEEE Transactions on Industry Applications, vol. 47, no. 2, pp. 831-840, March-April 2011.

- [22] R. Zhang, M. Cardinal, P. Szczesny and M. Dame, "A grid simulator with control of single-phase power converters in D-Q rotating frame," 2002 IEEE 33rd Annual IEEE Power Electronics Specialists Conference. Proceedings (Cat. No.02CH37289), Cairns, Qld., Australia, 2002, pp. 1431-1436 vol.3.
- [23] M. Gonzalez, V. Cardenas and F. Pazos, "DQ transformation development for single-phase systems to compensate harmonic distortion and reactive power," 9th IEEE International Power Electronics Congress, 2004. CIEP 2004, Celaya, Gto., Mexico, 2004, pp. 177-182.
- [24] L. N. Arruda, S. M. Silva and B. J. C. Filho, "PLL structures for utility connected systems," Conference Record of the 2001 IEEE Industry Applications Conference. 36th IAS Annual Meeting (Cat. No.01CH37248), Chicago, IL, USA, 2001, pp. 2655-2660 vol.4.
- [25] Ciobotaru, Mihai & Teodorescu, R. & Blaabjerg, F, "Improved PLL structures for single-phase grid inverters," Proc. Power Electronics and Intelligent Control for Energy Conservation Conference (PELINCEC), Warsaw, Poland, 2004, pp. 1-6.
- [26] M. Ciobotaru, R. Teodorescu and F. Blaabjerg, "A new single-phase PLL structure based on second order generalized integrator," 2006 37th IEEE Power Electronics Specialists Conference, Jeju, 2006, pp. 1-6.
- [27] D. Das, D. M. Divan and R. G. Harley, "Power flow control in networks using controllable network transformers," in IEEE Transactions on Power Electronics, vol. 25, no. 7, pp. 1753-1760, July 2010.
- [28] A. Prasai, R. P. Kandula, R. Moghe, T. Heidel, C. Schauder and D. Divan, "Compact dynamic phase angle regulator for power flow control," 2015 IEEE Energy Conversion Congress and Exposition (ECCE), Montreal, QC, 2015, pp. 4985-4992.
- [29] R. L. Andersen, T. B. Lazzarin and I. Barbi, "A 1-kW Step-Up/Step-Down Switched-Capacitor AC-AC Converter," in IEEE Transactions on Power Electronics, vol. 28, no. 7, pp. 3329-3340, July 2013.
- [30] A. A. Khan, H. Cha and H. F. Ahmed, "High efficiency buck and boost type AC-AC converters," 2015 17th European Conference on Power Electronics and Applications (EPE'15 ECCE-Europe), Geneva, 2015, pp. 1-10.
- [31] J. Ramos-Ruiz, H. Krishnamoorthy and P. Enjeti, "Adding capacity to an existing electric power distribution network using a solid state transformer system," 2015 IEEE Energy Conversion Congress and Exposition (ECCE), Montreal, QC, 2015, pp. 6059-6066.

- [32] The GridWise Architecture Council (2015), “GridWise Transactive Energy Framework Version 1.0”, [Online]. Available: https://www.gridwiseac.org/pdfs/te_framework_report_pnnl-22946.pdf [Accessed on: March 20, 2020].
- [33] D. Forfia, M. Knight and R. Melton, “The View from the Top of the Mountain: Building a Community of Practice with the GridWise Transactive Energy Framework,” in IEEE Power and Energy Magazine, vol. 14, no. 3, pp. 25-33, May-June 2016.
- [34] K. Kok and S. Widergren, “A Society of Devices: Integrating Intelligent Distributed Resources with Transactive Energy,” in IEEE Power and Energy Magazine, vol. 14, no. 3, pp. 34-45, May-June 2016.
- [35] T. Morstyn, A. Teytelboym and M. D. Mcculloch, “Bilateral Contract Networks for Peer-to-Peer Energy Trading,” in IEEE Transactions on Smart Grid, vol. 10, no. 2, pp. 2026-2035, March 2019.
- [36] Y. Wu, X. Tan, L. Qian, D. H. K. Tsang, W. Z. Song and L. Yu, “Optimal Pricing and Energy Scheduling for Hybrid Energy Trading Market in Future Smart Grid,” in IEEE Transactions on Industrial Informatics, vol. 11, no. 6, pp. 1585-1596, Dec. 2015.
- [37] R. Bayindir, S. Demirbas, E. Irmak, U. Cetinkaya, A. Ova and M. Yesil, “Effects of renewable energy sources on the power system,” 2016 IEEE International Power Electronics and Motion Control Conference (PEMC), Varna, 2016, pp. 388-393.
- [38] R. R. Kolluri, I. Mareels, T. Alpcan, M. Brazil, J. de Hoog and D. Thomas, “Power sharing correction in angle droop controlled inverter interfaced microgrids,” 2015 IEEE Power & Energy Society General Meeting, Denver, CO, 2015, pp. 1-5.
- [39] J. A. Ramos-Ruiz, P. Enjeti and L. Xie, “Power Electronics Intelligence at the Grid Edge - Enables Energy Budgeting,” 2018 IEEE Electronic Power Grid (eGrid), Charleston, SC, 2018, pp. 1-6.
- [40] International Energy Agency (2016), “Renewable Energy Medium-Term Market Report 2016” [Online]. Available: <https://webstore.iea.org/medium-term-renewable-energy-market-report-2016>. [Accessed on: March 20, 2020].
- [41] M. Farivar, R. Neal, C. Clarke and S. Low, “Optimal inverter VAR control in distribution systems with high PV penetration,” 2012 IEEE Power and Energy Society General Meeting, San Diego, CA, 2012, pp. 1-7.

- [42] T. Aziz and N. Ketjoy, "PV Penetration Limits in Low Voltage Networks and Voltage Variations," in *IEEE Access*, vol. 5, pp. 16784-16792, 2017.
- [43] V. S. S. Kumar, L. Xie, and P. R. Kumar, "An Analytical Approach for Loss Minimization and Voltage Profile Improvement in Distribution Systems with Renewable Energy Resources," *IREP Symposium 2017*.
- [44] H. G. Yeh, D. F. Gayme, and S. H. Low, "Adaptive VAR Control for Distribution Circuits With Photovoltaic Generators," *IEEE Trans on Power Systems*, vol. 27:3, pp. 1656–1663, Aug. 2012.
- [45] A. Kwasinski, V. Krishnamurthy, J. Song and R. Sharma, "Availability Evaluation of Micro-Grids for Resistant Power Supply During Natural Disasters," in *IEEE Transactions on Smart Grid*, vol. 3, no. 4, pp. 2007-2018, Dec. 2012.
- [46] C. Abbey et al., "Powering Through the Storm: Microgrids Operation for More Efficient Disaster Recovery," in *IEEE Power and Energy Magazine*, vol. 12, no. 3, pp. 67-76, May-June 2014.
- [47] L. Comfort, A. Boin & C. Demchak (2010), "Designing Resilience: Preparing for Extreme Events". Pittsburgh, Univ. of Pittsburgh Press.
- [48] H. M. Chou, L. Xie, P. Enjeti and P. R. Kumar, "Power electronics intelligence at the network edge (PINE)", 2017 IEEE Energy Conversion Congress and Exposition (ECCE), Cincinnati, OH, 2017, pp. 5214-5221.
- [49] Kolter, J. Zico, and Matthew J. Johnson. "REDD: A public data set for energy disaggregation research," Workshop on data mining applications in sustainability (SIGKDD), San Diego, CA, vol. 25, 2011, pp. 59-62.
- [50] Pinney, D., "Costs and Benefits of Conservation Voltage Reduction." [Online] Available: https://www.smartgrid.gov/files/recovery_act/NRECA_DOE_Costs_Benefits_of_CVR_0.pdf [Accessed on: March 20, 2020].
- [51] Mohan, N., Undeland, T. M., & Robbins, W. P. (2003). "Power electronics: Converters, applications, and design", Chapter 18-6. New Delhi, India: John Wiley & Sons.
- [52] EATON, "Energy management circuit breaker", [Online] Available: <https://www.eaton.com/us/en-us/markets/innovation-stories/energy-management-circuit-breaker.html>. [Accessed on: March 20, 2020].

- [53] H. Kang, T. SHIM, S. H. Kim, S. Jeong and Y. An, “A Testbed for Experimenting IoT Platform on High-Voltage Customer Electrical Installation,” 2018 International Conference on Information and Communication Technology Convergence (ICTC), Jeju, 2018, pp. 1301-1304.
- [54] S. Golestan, M. Monfared, J. M. Guerrero and M. Joorabian, “A D-Q synchronous frame controller for single-phase inverters,” 2011 2nd Power Electronics, Drive Systems and Technologies Conference, Tehran, 2011, pp. 317-323.
- [55] J. T. Hawke, H. S. Krishnamoorthy and P. N. Enjeti, “A Family of New Multiport Power- Sharing Converter Topologies for Large Grid-Connected Fuel Cells,” IEEE Journal of Emerging and Selected Topics in Power Electronics, vol. 2:4, pp. 962-971, Dec. 2014.
- [56] S. A. Sabeeh Al-Obaidi, K. C. Hodge and P. Enjeti, “A Dual-Phase Output 4-Leg Inverter with Active Decoupling and Integrated Power Optimizer for Off-Grid Applications,” 2018 9th IEEE International Symposium on Power Electronics for Distributed Generation Systems (PEDG), Charlotte, NC, USA, 2018, pp. 1-6.
- [57] R. L. Steigerwald and K. T. Ngo, “Full-bridge lossless switching converter,” U. S. Patent 4 864 479, Sept. 5, 1989, [Online] Available: <https://patents.google.com/patent/US4864479A/en>. [Accessed on: March 20, 2020].
- [58] A. Safaee, P. Jain and A. Bakhshai, “Time-domain analysis of a wide-range dual-active-bridge bidirectional series resonant converter,” IECON 2015 - 41st Annual Conference of the IEEE Industrial Electronics Society, Yokohama, 2015, pp. 004139-004145.
- [59] Erickson, R. W., & Maksimović, D. (2001). “Fundamentals of Power Electronics” New York: Kluwer Academic.
- [60] J. Dickert and P. Schegner, “Residential load models for network planning purposes,” 2010 Modern Electric Power Systems, Wroclaw, 2010, pp. 1-6.
- [61] M. Karimi, H. Mokhlis, K. Naidu, S. Uddin, A.H.A. Bakar, “Photovoltaic penetration issues and impacts in distribution network – A review,” Renewable and Sustainable Energy Reviews, vol. 53, pp.594-605, 2016.
- [62] J. Johnson et al., “Distribution Voltage Regulation Using Extremum Seeking Control With Power Hardware-in-the-Loop,” in IEEE Journal of Photovoltaics, vol. 8, no. 6, pp. 1824-1832, Nov. 2018.

- [63] S. Gonzalez, J. Johnson and J. Neely, “Electrical power system support-function capabilities of residential and small commercial inverters,” 2015 IEEE 42nd Photovoltaic Specialist Conference (PVSC), New Orleans, LA, 2015, pp. 1-6.
- [64] P. Jahangiri and D. C. Aliprantis, “Distributed Volt/VAr Control by PV Inverters,” in IEEE Transactions on Power Systems, vol. 28, no. 3, pp. 3429-3439, Aug. 2013.
- [65] R. Moghe, D. Divan, D. Lewis and J. Schatz, “Turning Distribution Feeders Into STATCOMs,” in IEEE Transactions on Industry Applications, vol. 53, no. 2, pp. 1372-1380, March-April 2017.
- [66] IEEE PES AMPS DSAS Test Feeder Working Group, (1992). “37-bus Feeder” [Online]. Available: <https://site.ieee.org/pes-testfeeders/resources/>. [Accessed on: March 20, 2020].
- [67] A. R. Malekpour and A. Pahwa, “Radial Test Feeder including primary and secondary distribution network,” 2015 North American Power Symposium (NAPS), Charlotte, NC, 2015, pp. 1-9.

APPENDIX A

LINE PARAMETERS OF TEST FEEDER SYSTEM. ADAPTED FROM [67]

From Node #	To Node #	Resistance (Ω)	Inductance (H)
0	1	1.00E-01	0
1	2	9.271E-02	1.766E-04
2	3	8.160E-02	1.292E-04
3	4	1.122E-01	1.776E-04
4	5	9.576E-02	8.920E-05
5	6	6.906E-02	8.898E-05
6	7	7.980E-02	7.433E-05
6	8	1.117E-01	1.041E-04
4	9	1.480E-01	1.907E-04
3	25	1.596E-01	1.487E-04
3	28	8.879E-02	1.144E-04
28	29	1.282E-01	1.653E-04
29	30	3.192E-02	2.973E-05
30	31	2.075E-01	1.933E-04
31	38	2.619E-01	2.572E-04
38	39	5.238E-01	5.145E-04
39	40	5.238E-01	5.145E-04
40	41	5.238E-01	5.145E-04